Engineering the flow behavior of colloidal materials through surface modification and shape anisotropy

by

Chien Ching Lilian Hsiao

A dissertation submitted in partial fulfillment
of the requirements for the degree of
Doctor of Philosophy
(Chemical Engineering)
in the University of Michigan
2014

Doctoral committee:

Professor Michael J. Solomon, Chair
Professor Sharon C. Glotzer
Professor Ronald G. Larson
Assistant Professor Xiaoming Mao

In loving memory of my late grandparents, Gong Gong and Mak

ACKNOWLEDGEMENTS

Graduate school, for me, was a transformative experience. Moments of independent discovery were few. But when they came they absolutely thrilled me and gave me the willpower to continue. Most of all, I would like to express my deep gratitude to the people that have made my accomplishments possible.

My research advisor, Mike Solomon, is a world-class scientist and a world-class educator. He is, hands down, one of the best advisors that a graduate student could ever ask for. (Despite my rebellious nature, I would never trade him for anyone else!) Mike gave me the freedom and resources to explore and as a result, I gained the breadth and depth of knowledge necessary for an academic career. Mike's emphasis on consistency, quality, and integrity has made a significant impact on the work that I have been able to produce over the course of my PhD. I am honored by the high standards that he placed on me, because it is a symbol of confidence - this is not something I fully appreciated and understood until later on. As the years fly by, I became increasingly amazed at his great intellect and his endless support and patience for his students. I hope that I can take all of these qualities with me if I lead my own research group.

I am eternally grateful to my committee member and mentor, Sharon Glotzer. Sharon is a fighter who does not submit to adversity. I am certain that her success is won through passion, hard work, and perseverance. When my very first manuscript was rejected, Sharon told me of the

many roads to Rome. When I asked for research and career advice, Sharon freely provided recommendations from her own stories. When I was agonizing over my future, Sharon personally gave me the encouragement needed to pursue my dreams. I feel extremely privileged that Sharon is one of my biggest advocates, and I will always look up to her great strength.

I would like to thank my two other committee members, Ron Larson and Xiaoming Mao, for providing valuable technical insights throughout the course of my PhD. Ron is one of the most brilliant, yet humble people that I have ever encountered in my life. I admire Ron greatly for his legendary ability to absorb a textbook's worth of material overnight, even in areas far from his expertise. He will always be known as the god of fluid dynamics to me! I have also enjoyed many fruitful scientific discussions with Xiaoming, who taught me to work with care to details. I hope to continue collaborative work with her down the road.

Over the years, Mike gave me ample opportunities to develop a network of peers and to interact closely with a number of other professors. I would like to give special thanks to Eric Furst for inviting me to work with his students and his optical tweezers at the University of Delaware. There, and on multiple occasions elsewhere, I had the chance to exchange ideas with Norman Wagner, who exudes energy and great passion for his research. John Younger and Greg Thurber, both at the University of Michigan, have been very generous in giving me career advice. Peter Green granted me frequent usage of his top-notch equipment, allowing me to conduct experiments of high quality with great efficiency.

I wish to thank my collaborators, all of whom worked tirelessly with me on research projects - Kathy Whitaker, my counterpart at Delaware who performed optical trapping experiments with me; Indranil Saha Dalal, for writing up an image processing algorithm from scratch without asking for anything in return; Daniel Beltran-Villegas, for providing help with

simulations and sharing advice about everything; Benjamin Schultz, for churning out data quickly in a time crunch; Emmanouil Glynos, for doing outstanding AFM work and providing much needed humor; Richmond Newman, for his friendship, delicious food, and his work on my first manuscript; and the Green, Larson, and Glotzer group members who treated me as a lab member because of my frequent work with them. I would also like to thank all my undergraduate research assistants - they did a lot of exploratory work and I learned to become a better mentor through them.

The departmental staff are remarkably helpful and friendly to graduate students. I would like to thank Karen Coulter, Harald Eberhart, Susan Hamlin, Rhonda Sweet, Shelley Fellers, Kelly Raickovich, Mike Africa, Ruby Sowards, Barbara Perry, and Justin Scanlon for providing excellent administrative and technical support.

Speaking of friendship, my graduate school experience would not be complete without my circle of friends. My best friend since 8th grade, Tien-Huei, was here with me through thick and thin. Alexey, Leo, and Laura are always around to listen when I needed to vent. I enjoyed many a night of dungeons and dragons with Matt, Julia, Thomas, and Chad. Fun times were had with my friends in the Solomon, Savage, and Linic groups. I truly enjoyed their companionship, particularly at the final stages of my dissertation writing when I needed it most.

Finally, I would like to thank my mom and dad for their love and support despite being so far away from home. This has been a fascinating and life-changing journey; none of it would be possible without the people who helped me see it through.

TABLE OF CONTENTS

LIST OF FIGURES

LIST OF TABLES

LIST OF APPENDICES

ABSTRACT

In this dissertation, we explore the idea that colloidal materials can be designed with enhanced rheological properties by incorporating shape and surface anisotropy. This hypothesis is motivated by our finding that structural rigidity can be used to predict the nonlinear elasticity in gels that have undergone yielding in high-rate strain flows. The rigidity contributes to gel elasticity even when the sample is fully fluidized; the origin of the elasticity is the slow Brownian relaxation of rigid, hydrodynamically interacting clusters. We report a power-law scaling of the elastic modulus with the stress-bearing volume fraction that is valid over a range of volume fractions and gelation conditions. We demonstrate that the predictive power of microscopic theories can be improved when both the microstructural rigidity and the dynamical heterogeneity induced by yielding are taken into account. The dynamical heterogeneity takes a bimodal form in the self-part of the van Hove correlations, indicating subpopulations of slow and fast colloids within sheared gels.

Because thermal rupture forces play a critical role in yielding, we develop a model gel system in which rheological measurements can be carried out in conjunction with microscopy experiments and optical trapping. Sterically stabilized poly(methyl methacrylate) (PMMA) colloids are suspended in cyclohexane (CH) and cyclohexyl bromide (CHB) with dilute polystyrene as a depletion agent. A study of the optical trap strength, rheology, and microscopic structure of the gels as a function of CH/CHB solvent composition identifies the conditions for

which these measurements can be applied to characterize gel properties.These measurements allow us to compare simultaneous measurements of viscoelasticity, microstructure, and interparticle forces.

In the later part of this dissertation, we aim to test the validity of structural rigidity by synthesizing colloidal spheroids and roughened particles. We find that colloidal oblate spheroids, synthesized by thermomechanical compression, self-assemble into tilted structures in a specific range of volume fractions and attraction strengths. The phase behavior and aggregation kinetics of the three-dimensional self-assembled structures are quantified by measuring the degree of clustering and local orientational order.These structures could pave the way for maintaining the elasticity of colloidal gels even at exceedingly low particle loading. Finally, we observe a significant decrease in the critical shear rate required for shear thickening in concentrated suspensions of rough colloids. Nevertheless, we find a negligible difference in the time-dependent translational diffusivity between smooth and rough colloids. These results collectively provide experimental support for the applicability of structural rigidity as a guiding principle in engineering the flow properties of a broad range of soft matter.

CHAPTER 1

Introduction

Colloidal systems: connecting the microscale to the macroscale

Colloidal dispersions consist of particles with sizes ranging from tens of nanometers to a few microns suspended in a dispersed phase. Different types of attractive and repulsive interactions can be induced between these particles, leading to phenomena such as crystallization [1], phase separation [2-4], and glass transition [5]. Colloids are found in many industrial and technological applications, such as ink processing and direct-write printing [6], sensors and photonics [7], ceramics development [8, 9], consumer products [10], household items [10], and foods such as yogurt and cream [11].

One of the main advantages of studying colloids is that they are excellent model systems: colloids with sizes greater than the wavelength of visible light can be directly observed with optical and fluorescence microscopy, allowing for precise characterization of their spatial and temporal locations. In addition, they are sufficiently small to exhibit Brownian motion due to the thermal energy of the solvent. The extent of these thermally induced fluctuations in particle position is highly dependent on the interparticle forces that exist between individual colloids. For example, gelled networks formed through attractive interactions can break up when a sufficiently large force is applied [12]. It is known that this critical force is stochastic in nature; that is, the minimum force required to break bonds is not a singular value, but rather a distribution that

depends on the depth and width of the attractive potential [13]. While thermal fluctuations are weak, in the absence of external fields such as gravity, they are still able to impose a limit on the lowest volume fraction at which structures can form [14]. Subtle differences in these thermal fluctuations can also lead to the emergence of dynamical heterogeneity [15, 16] in a manner that is reminiscent of supercooled liquids [17]. The collective motions of these fluctuations play an important role in determining the bulk properties of colloidal suspensions.

Consequently, there has been a concerted effort to understand the microscopic contribution of particle-particle interactions to the overall structure and dynamics of a system, which ultimately leads to the ability to control material properties. The connection between bulk properties to the structure of colloidal systems is qualitatively understood. For example, well-defined photonic bandgaps are expected to arise from the regular lattice positions in a crystalline structure [18, 19]. The viscoelasticity of a material can be enhanced by increasing the packing fraction or attraction in a system [20]. The quantitative aspects of predicting the formation of such structures are not so clear however. How does one generate, for example, a load-bearing gel structure that has a large yield stress without resorting to trial-and-error? What happens when surface and shape anisotropies are introduced into the system? Is there a scaling law for which bulk properties can be predicted from microstructure with accuracy? This dissertation aims to address these questions by developing a guiding framework based on the experimental studies of the structural and dynamical physics of colloidal suspensions, using a number of colloidal synthetic methods to generate shape and surface anisotropies, and examining the macroscopic flow behavior of these systems.

Repulsive and attractive interactions

The competition between attraction and repulsion is responsible for a majority of the phase behavior and bulk properties seen in colloidal suspensions [21]. When colloids with similar surface charges approach one another, they experience a repulsive (Coulombic) potential as a function of their approach distance. The range of this repulsion, characterized by the Debye length, can be reduced by screening the electrostatic double layer with a solvent containing counterions. The addition of a large quantity of counterions (in the form of salt or changes in pH) can result in almost complete screening of the Debye length to generate near-hard sphere suspensions [22], for which the phase behavior and hydrodynamics is well understood [23]. Colloidal crystals rely on the interaction of charged colloids to maintain lattice spacing [24, 25], and the onset of the glass transition can be accelerated in dense suspensions by the compression of the Debye layer [26].

Attractive interactions are commonly present in the form of van der Waals [27] or hydrophobic interactions [28]. Adjustable forms of the attractive potential can be introduced using sticky spheres [29] or a depletion attraction [30]. Depletion is an entropically driven process: when small, non-adsorbing molecules are excluded from the gap between two colloidal particles by virtue of the fact that their size is greater than the gap, an unbalanced osmotic pressure develops and drives colloids into contact to minimize the overall free energy [31]. In this dissertation, we focus on using depletion interactions as the driving force behind gelation and self-assembly, because they provide a simple and elegant method to control the strength and range of the attractive forces within the system.

Yielding of colloidal gels in large flows

When a net attraction is induced in a colloidal suspension with sufficient packing fraction, a gelled network is formed. Gels exhibit slow, arrested dynamics and unusual viscoelastic behavior [32]. The solid-like rheology of colloidal gels, combined with the ease of changing their viscoelastic properties by tuning the interparticle potential [33-35], makes them highly desirable candidates in technological development. Particulate gels undergo yielding beyond a critical yield stress, causing the previously rigid structure to rupture [36]. Large voids and aggregates often form during this nonlinear rheological process [37, 38]. This catastrophic transition can be induced, for example, by the sudden stresses encountered in transportation and processing. Yielding poses serious problems in industrial goods; examples include structural failures in ceramics and sedimentation that leads to product instability in pharmaceutical formulations. While changes in gel viscoelasticity agree well with theoretical models in the linear deformation regime [39-42], the microscopic origin of the yielding phenomenon is far less predictable due to complicating factors from flow inhomogeneities [43], shear banding [44, 45], and dynamical heterogeneity [46, 47].

Investigation of microstructural changes using conventional microscopy techniques is the most direct method of analyzing the relationship between gel structure and yielding behavior. Because the technique suffers from resolution limitations during motion capture even with fast scanning microscopes, a majority of studies provide the analysis of orientations and trajectories of colloidal particles during flow only at low shear rates [48-50]. Within this linear regime, cage breaking can occur for high volume fraction gels [20], and intracluster bond breakage has been experimentally observed in dilute gels [51]. Complete network rupture is rarely studied due to the high shear rates and deformations required. Our goal is to directly visualize the complex

behavior of a colloidal gel as it undergoes yielding at large deformations and high shear rates. The changes in microstructure and dynamics are used to form connections to the linear and nonlinear rheological data.

Microstructure and dynamical characterization with microscopy

Confocal laser scanning microscopy is widely used to investigate colloidal systems in which the particle length scales are larger than the wavelength of incident light. Because the out-of-focus light from multiple scattering are reduced using point-by-point rastering and pinhole apertures, the two-dimensional (2D) and three-dimensional (3D) structure and dynamics of fluorescent colloids [52] that are refractive index matched with the suspending solvent can be observed even deep within the sample [53]. This alleviates the need to image at the coverslip, where colloids tend to interact strongly with the walls. With a high numerical aperture objective and at visible light wavelengths, the maximum lateral and axial resolution are limited by the Rayleigh criterion to ~200 nm and ~500 nm respectively [54].

Once images are captured, image processing is necessary to generate meaningful structural and dynamical quantities. Crocker and Grier developed a workhorse algorithm that identifies particle centroids based on applying a Gaussian mask to filter out digital noise, locating the brightest local intensity, and refining the position of the centroid to subpixel accuracy [55]. The accuracy of these image processing algorithm depends heavily on the refractive matching between colloid and solvent, and to a lesser degree, on the particle loading in the suspension. In dense suspensions where imaging artifacts cannot be avoided, image processing techniques that rely on edge detection, such as the Hough transform, perform far better than algorithms based on the local intensity maxima [56]. In our study, we focus on

characterizing short- and long-range structure using the radial distribution function, contact number distribution, cluster size, and structure factor. 2D particle tracking yields dynamical measures such as the single-particle mean squared displacement and the single-particle self-part of the van Hove correlations [57]. These parameters allow us to quantify colloidal structure and dynamics obtained from direct observation.

Effect of shape and friction in colloidal systems

Jamming is a process in which complex fluids become completely rigid at high packing fractions. This phenomenon is ubiquitous in densely packed granular media [58], but has also been proposed for colloidal systems for which strong kinetic arrest exists [59]. Both types of soft matter are known to jam with increasing volume fraction, where they form a rigid network that is capable of bearing finite shear stresses. As we approach the critical point of jamming, the configuration of contacts between particles becomes isostatic; that is, they become structurally rigid with respect to their constraints and degrees of freedom [60]. Normally, this is only discussed within the context of repulsion-driven dense packings. However, we have perceived locally dense regions in colloidal gels that would allow us to not only visualize the rheological changes associated with jamming, but also to analyze the validity of naïve constraint counting methods that are commonly used in the study of granular materials.

Constraint counting is a simple method by which Maxwell first quantitatively determined the structural rigidity of objects: a set of nodes interacting through central, pairwise interaction can only be isostatic and rigid if the number of constraints is equal to the number of degrees of freedom. This means that triangles and tetrahedra are the most basic rigid configurations in 2D and 3D respectively. Surprisingly, we see analogous structures in attractive colloidal systems

[61]. These rigid structures are responsible for elastic properties in percolated and jammed systems [62-65].

Shape and surface anisotropy are believed to important parameters in enhancing mechanical strength. Many experimental and theoretical studies in granular materials support this hypothesis. Particles with frictional forces jam easily, because they form stress-bearing chains that relax slowly on experimental time scales [66]. As a result, they require fewer nearest neighbors to bear load [67], and contribute to phenomenon such as discontinuous shear thickening [68] and a reduced critical shear rate for the jamming transition [69]. Certain particle shapes, such as highly-faceted polyhedra and interlocking jacks, are known to produce high stiffness and compressive strength in granular materials [70]. Fiber networks resist bending and stretching [71], and even simple ellipsoids can pack in closer configurations than spheres [72].

One of the major challenges of using granular systems is their lack of refractive index matching; that is, the ease of generating shape anisotropy (through 3D printing and other means) is offset by the difficulty in studying their 3D structure and dynamics. Although efforts have been made to image dense granular structures in refractive index matched fluids [73], the sophistication of such methods remain far from that developed for colloidal suspensions. Recent advances in colloidal synthesis techniques have led to the production of high quality tetrahedral clusters [30], metallic Janus spheres [74], and ellipsoidal shapes [75, 76] suitable for confocal microscopy. By combining the ability to synthesize anisotropic colloids, the instrumental capabilities of confocal imaging and rheometry, and the tunability of particle-level interactions, we can probe the effect of shape and surface anisotropy on the mechanical properties of colloidal suspensions.

Research objectives and motivation

The overarching aim of this dissertation is to offering a framework that can be used to predict the flow behavior of a broad range of soft matter based on its microstructure. This work is built upon applying the governing principle of structural rigidity at the macroscale (bridges, buildings, domes) to explain nonlinear elasticity at the microscale. By understanding the structural and dynamical physics that govern the nonlinear rheology of colloidal gels, we explore the means to harness this knowledge in order to engineer colloidal materials with enhanced mechanical properties.

All experimental work are conducted using poly(methyl methacrylate) (PMMA) colloids suspended in organic solvents to allow microscopy and rheometry experiments to be conducted in parallel. We summarize the studies in this dissertation here:

1. We impose simple shear flows of various strains on the gels and use a confocal laser scanning microscope to characterize the resulting 3D structural changes. Contrary to methods based on ensemble-averaged parameters, we find that bond breakage in gels occurs mainly due to the erosion of rigid clusters that persist far beyond the yield strain. We develop a simple correlation between the elastic modulus and the stress-bearing volume fraction that is valid over a range of volume fractions and gelation conditions. Since gels contain local regions of dense packings, we ask the questions: in what way would microstructural rigidity affect rheology, and are the correlations sufficiently general to match the physics of other soft materials? To address these questions, we directly visualize the flow of colloidal gels composed of isotropic spheres and study their corresponding elastic and shear moduli in high strain-rate deformations.

2. As a continuation of 1, we investigate the combined effect of structural rigidity and dynamical heterogeneity on the nonlinear elasticity of colloidal gels that have undergone yielding. We observe a decrease in the subdiffusive motion of the particles as the applied strain increases. This deformation introduces a bimodal distribution in the van Hove self-correlation function, suggesting the existence of a fast and slow subpopulation of colloids within sheared gels. We show that the predictive power of microscopic theories that connect elasticity to localization length can be improved by considering only this slow subpopulation. This work is a close collaboration with Dr. Heekyoung Kang and Prof. Kyung-Hyun Ahn at the Seoul National University.
3. We report a model gel system that allows coordinated two-particle force measurement by optical trapping, microstructure from confocal microscopy, and linear viscoelasticity from rheometry. Mixtures of cyclohexane and cyclohexyl bromide are used. We discuss the limits imposed by sedimentation and refractive index mismatch on the three experimental techniques used. This work is a close collaboration with Kathryn Whitaker and Prof. Eric Furst at the University of Delaware.
4. We use high-speed 3D confocal imaging to directly observe the self-assembly of a model system of colloidal PMMA oblate spheroids with aspect ratio of 0.46. Oblate spheroids are known for their tendency to produce tilted structures. Based on structural arguments from isostaticity, we believe that orientational aggregates could promote mechanical properties even at reduced particle loading. As a first step towards realizing this goal, long-ranged depletion attraction is used to induce self-assembly in these spheroids. We induce orientational aggregation in these assemblies by systematically varying the packing fraction and the depth of the attractive potential. In addition, we seek to deduce the mechanism of

orientational aggregation by studying the cluster and orientational aggregation kinetics of these assemblies.

5. Because friction reduces the isostatic criterion needed for jamming, introducing surface roughness into densely packed colloidal suspensions could have a significant effect on their rheological properties. To test this idea, we synthesize PMMA colloids with large surface roughness to examine the effect of steric hindrance on translational motion in dense suspensions. Rheological experiments show that they jam at lower weight fractions than smooth spheres. We compare the differences in the translational motion of smooth and rough colloids in concentrated suspensions.

Outline of the dissertation

This dissertation provides a guiding principle for designing the viscoelasticity of colloidal suspensions, and experimentally supports this framework by studying the effect of shape and surface modification on rheological properties. In Chapter 2, we form a universal scaling relation between nonlinear elasticity and structural rigidity for colloidal gels that have undergone yielding. In Chapter 3, we show that strong flows introduce a specific kind of dynamical heterogeneity in colloidal gels. A simple modification of mode coupling theory that considers only the contribution of localized dynamics provides excellent agreement with the nonlinear elasticity of these gels across a large range of deformations. Chapter 4 describes the development of a model gel system in which microscopy and rheological characterization can be performed alongside thermal rupture force measurements using optical tweezers. In Chapter 5, we explore methods to generate PMMA spheroids that can be self-assembled in density-matched solvents, along with their phase behavior and assembly kinetics. In Chapter 6, we find that surface

roughness gives rise to an increase in shear thickening and jamming behavior at lower volume fractions. We compare the translational diffusivities of smooth and rough colloids in these suspensions. The summarizing remarks are presented along with future work in Chapter 7.

References

[1] F. M. van der Kooij, K. Kassapidou, and H. Lekkerkerker, *Nature* **406**, 868 (2000).
[2] W. C. K. Poon, *Current Opinion in Colloid & Interface Science* **3**, 593 (1998).
[3] P. Germain and S. Amokrane, *Physical Review Letters* **102**, 4 (2009).
[4] V. J. Anderson and H. N. W. Lekkerkerker, *Nature* **416**, 811 (2002).
[5] C. Klix, C. Royall, and H. Tanaka, *Physical Review Letters* **104**, 165702 (2010).
[6] B. Ahn *et al.*, *Science* **323**, 1590 (2009).
[7] E. M. Furst, E. Dufresne, and C. O'Hern, *ACS Nano* **5**, 6695 (2011).
[8] F. F. Lange, *Journal of the American Ceramic Society* **72**, 3 (1989).
[9] J. J. Guo and J. A. Lewis, *Journal of the American Ceramic Society* **83**, 2341 (2000).
[10] M. J. Solomon and P. T. Spicer, *Soft Matter* **6**, 1391 (2010).
[11] E. Dickinson (1992). An Introduction to Food Colloids (Oxford University Press, Oxford).
[12] D. Bonn and M. M. Denn, *Science* **324**, 1401 (2009).
[13] J. Swan, M. Shindel, and E. Furst, *Physical Review Letters* **109**, 198302 (2012).
[14] S. Manley *et al.*, *Physical Review Letters* **93**, 108302 (2004).
[15] A. Puertas, M. Fuchs, and M. Cates, *Journal of non-crystalline solids* **352**, 4830 (2006).
[16] Y. Gao and M. Kilfoil, *Physical Review Letters* **99**, 78301 (2007).
[17] W. Kob, C. Donati, S. J. Plimpton, P. H. Poole, and S. C. Glotzer, *Physical Review Letters* **79**, 2827 (1997).
[18] J. McMullan and N. J. Wagner, *Soft Matter* **6**, 5443 (2010).
[19] C. G. Schäfer, D. A. Smolin, G. P. Hellmann, and M. Gallei, *Langmuir* **29**, 11275 (2013).
[20] N. Koumakis and G. Petekidis, *Soft Matter* **7**, 2456 (2011).
[21] C. P. Royall, D. Aarts, and H. Tanaka, *Journal of Physics: Condensed Matter* **17**, S3401 (2005).
[22] B. J. Maranzano and N. J. Wagner, *Journal of Rheology* **45**, 1205 (2001).
[23] C. G. Dekruif, E. M. F. Vanlersel, A. Vrij, and W. B. Russel, *Journal of Chemical Physics* **83**, 4717 (1985).
[24] T. Okubo, *Accounts of Chemical Research* **21**, 281 (1988).
[25] M. E. Leunissen, C. G. Christova, A.-P. Hynninen, C. P. Royall, A. I. Campbell, A. Imhof, M. Dijkstra, R. van Roij, and A. van Blaaderen, *Nature* **437**, 235 (2005).
[26] S. K. Lai, W. J. Ma, W. van Megen, and I. K. Snook, *Physical Review E* **56**, 766 (1997).
[27] I. Vakarelski, D. Chan, T. Nonoguchi, H. Shinto, and K. Higashitani, *Physical Review Letters* **102**, 4 (2009).
[28] Q. Chen, J. K. Whitmer, S. Jiang, S. C. Bae, E. Luijten, and S. Granick, *Science* **331**, 199 (2011).
[29] J. M. Kim, J. Fang, A. P. R. Eberle, and N. J. Wagner, *Physical Review Letters* **110**, 208302 (2013).
[30] G. Meng, N. Arkus, M. Brenner, and V. Manoharan, *Science* **327**, 560 (2010).
[31] S. Asakura and F. Oosawa, *Journal of Chemical Physics* **22**, 1255 (1954).
[32] E. Zaccarelli, *Journal of Physics: Condensed Matter* **19**, 323101 (2007).
[33] A. Eberle, N. Wagner, and R. Castañeda-Priego, *Physical Review Letters* **106**, 105704 (2011).
[34] H. Guo, S. Ramakrishnan, J. L. Harden, and R. L. Leheny, *Journal of Chemical Physics* **135**, 154903 (2011).
[35] C. J. Rueb and C. F. Zukoski, *Journal of Rheology* **42**, 1451 (1998).

[36] V. Gopalakrishnan and C. F. Zukoski, *Langmuir* **23**, 8187 (2007).
[37] P. Varadan and M. J. Solomon, *Journal of Rheology* **47**, 943 (2003).
[38] M. Kogan and M. J. Solomon, *Langmuir* **26**, 1207 (2010).
[39] R. A. Lionberger and W. B. Russel, *Journal of Rheology* **38**, 1885 (1994).
[40] S. A. Shah, Y. L. Chen, K. S. Schweizer, and C. F. Zukoski, *Journal of Chemical Physics* **119**, 8747 (2003).
[41] W. Y. Shih, W. H. Shih, and I. A. Aksay, *Journal Of The American Ceramic Society* **82**, 616 (1999).
[42] W. H. Shih, W. Y. Shih, S. I. Kim, J. Liu, and I. A. Aksay, *Physical Review A* **42**, 4772 (1990).
[43] T. Gibaud, D. Frelat, and S. Manneville, *Soft Matter* **6**, 3482 (2010).
[44] A. Fall, J. Paredes, and D. Bonn, *Physical Review Letters* **105**, 225502 (2010).
[45] S. M. Fielding, *Soft Matter* **3**, 1262 (2007).
[46] V. Kobelev and K. Schweizer, *Journal of Chemical Physics* **123**, 164902 (2005).
[47] E. Saltzman and K. Schweizer, *Physical Review E* **74**, 061501 (2006).
[48] B. Rajaram and A. Mohraz, *Soft Matter* **6**, 2246 (2010).
[49] K. Masschaele, J. Fransaer, and J. Vermant, *Journal of Rheology* **53**, 1437 (2009).
[50] K. Masschaele, J. Fransaer, and J. Vermant, *Soft Matter* **7**, 7717 (2011).
[51] H. Chan and A. Mohraz, *Physical Review E* **85**, 41403 (2012).
[52] A. Campbell and P. Bartlett, *Journal of Colloid and Interface Science* **256**, 325 (2002).
[53] A. Dinsmore, E. Weeks, V. Prasad, A. Levitt, and D. Weitz, *Applied Optics* **40**, 4152 (2001).
[54] M. J. Solomon and M. Kogan, *Encyclopedia of Condensed Matter Physics* **9** (2005).
[55] J. C. Crocker and D. G. Grier, *Journal of Colloid and Interface Science* **179,** 298 (1996).
[56] M. C. Jenkins and S. U. Egelhaaf, *Advances in Colloid and Interface Science* **136**, 65 (2008).
[57] C. J. Dibble, M. Kogan, and M. J. Solomon, *Physical Review E* **77**, 50401 (2008).
[58] A. Liu and S. Nagel, *Nature* **396**, 21 (1998).
[59] V. Trappe, V. Prasad, L. Cipelletti, P. N. Segre, and D. A. Weitz, *Nature* **411**, 772 (2001).
[60] M. v. Hecke, *Journal of Physics: Condensed Matter* **22**, 033101 (2010).
[61] A. Campbell, V. Anderson, J. van Duijneveldt, and P. Bartlett, *Physical Review Letters* **94**, 1 (2005).
[62] C. Moukarzel and P. M. Duxbury, *Physical Review Letters* **75**, 4055 (1995).
[63] C. Storm, J. J. Pastore, F. C. MacKintosh, T. C. Lubensky, and P. A. Janmey, *Nature* **435**, 191 (2005).
[64] M. Wyart, H. Liang, A. Kabla, and L. Mahadevan, *Physical Review Letters* **101**, 215501 (2008).
[65] D. J. Jacobs and M. F. Thorpe, *Physical Review Letters* **75**, 4051 (1995).
[66] E. Somfai, M. van Hecke, W. G. Ellenbroek, K. Shundyak, and W. van Saarloos, *Physical Review E* **75**, 020301 (2007).
[67] S. Papanikolaou, C. S. O'Hern, and M. D. Shattuck, *Physical Review Letters* **110**, 198002 (2013).
[68] R. Seto, R. Mari, J. F. Morris, and M. M. Denn, *Physical Review Letters* **111**, 218301 (2013).
[69] D. Lootens, H. Van Damme, Y. Hémar, and P. Hébraud, *Physical Review Letters* **95**, 268302 (2005).

[70] A. G. Athanassiadis *et al.*, *Soft Matter* **10**, 48 (2014).
[71] C. P. Broedersz, X. Mao, T. C. Lubensky, and F. C. Mackintosh, *Nature Physics* **7**, 983 (2011).
[72] A. Donev, I. Cisse, D. Sachs, E. Variano, F. H. Stillinger, R. Connelly, S. Torquato, and P. M. Chaikin, *Science* **303**, 990 (2004).
[73] J. A. Dijksman, F. Rietz, K. A. Lorincz, M. van Hecke, and W. Losert, *Review of Scientific Instruments* **83**, 11301 (2012).
[74] Q. Chen, S. C. Bae, and S. Granick, *Nature* **469**, 381 (2011).
[75] D. Dendukuri and P. Doyle, *Advanced Materials* **21**, 1 (2009).
[76] D. Mukhija and M. J. Solomon, *Journal of Colloid and Interface Science* **314**, 98 (2007).

CHAPTER 2

Role of isostaticity and load-bearing microstructure in the elasticity of yielded colloidal gels

Abstract

We report a simple correlation between microstructure and strain-dependent elasticity in colloidal gels by visualizing the evolution of cluster structure in high strain-rate flows. We control the initial gel microstructure by inducing different levels of isotropic depletion attraction between particles suspended in refractive index matched solvents. Contrary to previous ideas from mode coupling and micromechanical treatments, our studies show that bond breakage occurs mainly due to the erosion of rigid clusters that persist far beyond the yield strain. This rigidity contributes to gel elasticity even when the sample is fully fluidized; the origin of the elasticity is the slow Brownian relaxation of rigid, hydrodynamically interacting clusters. We find a power-law scaling of the elastic modulus with the stress-bearing volume fraction that is valid over a range of volume fractions and gelation conditions. These results provide a conceptual framework to quantitatively connect the flow-induced microstructure of soft materials to their nonlinear rheology. The text in this chapter is reprinted with permission from [L.C. Hsiao, R.S. Newman, S.C. Glotzer & M.J. Solomon, *Proc. Natl. Acad. Sci. USA* **109**, 16029-16034 (2012)].

Introduction

Colloidal gels form sample-spanning networks [1] and are used to generate solid-like properties in a broad range of materials such as direct-write inks [2], nanoemulsions [3], tissue scaffolds [4], and membranes [5]. When gels undergo large deformations, their network ruptures into clusters via a complex process. The ability to connect structural changes to suspension rheology is critical in understanding the mechanism of yielding. The network of clusters that makes up colloidal gels arises due to percolation, dynamic arrest, and phase separation, where the volume fraction and pair potential play an important part in their structure and rheology [6–8]. Interparticle bonds rupture under a sufficiently large stress; the result is a flow-induced fluidization transition accompanied by the formation of voids and aggregates that continuously break and reform along the principal axes of flow [9, 10]. A complex two-step yielding process has been observed in gels at intermediate volume fractions ($0.05 \leq \phi \leq 0.30$) [11, 12]. Within this regime, a small number of bonds are broken in gels undergoing steady shear yielding [9, 10]. Methods that track the evolution of ensemble-averaged structure, such as mode coupling theory [6] and light scattering, lack sensitivity to these subpopulations. On the other hand, micromechanical treatments directly model the contributions of local microstructure to the macroscopic elasticity of the material [13–15]. However, experiments to connect the yield stress to different interparticle potentials, volume fractions, and particle sizes show little agreement. Presently, these theories can only provide estimates of colloidal rheology under specific conditions.

We demonstrate that a simple, general correlation between microstructure and strain-dependent rheology exists for colloidal depletion gels undergoing large deformations at high shear rates. Our experiments harness confocal laser scanning microscopy (CLSM) to capture the

three-dimensional (3D) morphology of colloidal gels. Non-adsorbing polystyrene and photopolymer are used to induce depletion attraction of various strengths (Table 2.1, Fig. 2.1). Quiescent gels exhibit structures (Fig. 2.2a, b) and rheology (Fig. 2.2c) that are typical of colloidal gels [7, 11]; specifically, there is a prominent peak in the radial distribution function $g(r)$ at the first coordination shell, and the structure factor $S(q)$ is elevated at low scattering vectors q. The rheological response shows a crossover between the elastic and viscous moduli at the yield strain. (Complete rheological data can be found in Fig. 2.3.) We generate gels with a variety of initial microstructures by changing the depletion potential, the colloidal volume fraction, the gelation time, and degree of preshearing [16] (Fig. 2.4).

Previous attempts to visualize yielding have been complicated by shear banding [17], concurrence of rupture and reaggregation in steady flow, and difficulties in resolving particle positions at large deformation rates [9, 10, 18, 19]. We resolve these issues (particularly shear banding, see Fig. 2.5) by using uni-directional, high-rate step strains within a shear cell mounted to the CLSM (Fig. 2.2d). Incorporation of ultraviolet-initiated photopolymer to the solvents allows structures to be rapidly locked in place for imaging. We confirm that the immobilized sample represents the post-deformation structure by comparing the arrest time of the photopolymerization to the characteristic stress relaxation time of the gel. The difference between them is negligible (Fig. 2.6), indicating that photopolymerized gels precisely reflect the structure after cessation of flow.

To formulate a general correlation between rheology and microstructure, we look to the physics of granular materials for inspiration. In 1864, Maxwell determined that a particular configuration of nodes interacting with central, pairwise forces can only be isostatic and rigid if the number of constraints is equal to the degrees of freedom [20]. This definition motivates a

criterion for rigidity in colloidal gels, since gels support stress just as macroscopic structures are designed to withstand loads. For example, triangular and tetrahedral arrangements of trusses are used in architecture due to their structural stability. Analogous colloidal structures manifest themselves as Bernal spirals in gels [21, 22] and tetrahelices in dodecagonal quasicrystals [23]. Distinguishing between particles in rigid clusters and those connected by soft bonds allows us to parameterize micromechanical models proposed for colloidal systems [24–26]. Similar ideas have been used in fibre networks [27] and granular materials [28] to quantify the contribution of rigidity to the mechanics of 3D networks. Frictionless spheres in granular matter, for example, jam at the isostatic contact number of six [29]. These treatments suggest that the contact number may be used as a metric of isostatic connectivity [30]. In order to examine their implications in colloidal gels, we identify stress-bearing colloids as particles with z greater or equal to the isostatic contact number, z_{iso}, of spheres interacting through central forces (i.e. $z \geq z_{iso}$, where $z_{iso} = 6$).

Materials & Methods

Preparation of colloidal gels

A suspension of sterically-stabilized poly(methyl methacrylate) (PMMA) dyed with Nile Red dispersed in a refractive index matched solvent was used. We synthesized monodisperse dimethyl-diphenyl siloxane (DPDM) stabilized PMMA spheres of two diameters [36], $2a$ = 861 nm ± 5% and 1.06 μm ± 4%, as well as poly(12-hydroxystearic acid) (PHSA) stabilized PMMA spheres [37] of diameter $2a$ = 1.67 μm ± 4%. Gels were created by adding a combination of non-adsorbing, linear polystyrene of various concentration (M_W = 900,000 g/mol, $M_w/M_n \leq 1.10$, R_g = 41 nm, c_p^* = 0.0053 g/mL) and a UV-triggered photopolymer [38] to particles suspended in two

solvents: (i) 55% cyclohexyl bromide: 10% decalin:35% dioctyl phthalate and (ii) pure dioctyl phthalate. Tetrabutylammonium chloride of concentration ranging from 1 to 10 μM (Debye length of κ^{-1} = 69 nm) was added. Direct observation of the motion of the colloidal particles in an electric field device established an upper bound of the zeta potential ≤ 10 mV [39].

Confocal microscopy, shearing device, and structural measurements

Confocal microscopy images were acquired using a Leica TCS SP2 scanning head attached to a Leica DMIRE 2 inverted microscope and 100x, 1.4 numerical aperture oil immersion objectives. A shear cell with parallel glass plates was used for the visualization of gels before and after the application of a step strain [38]. The top plate was attached to a linear stepper motor. We ensured that the parallelism of the plates were within ± 10 μm. The gap distance between the plates was set to 120 μm for $5 \leq \gamma \leq 60$, and doubled to 240 μm for $0.5 \leq \gamma \leq 5$ to compensate for the very small displacements needed.

We allowed the gels to rest for a specified waiting time, t_w, after initial sample loading. Step strains were applied to the quiescent gel sample at a shear rate of 40 s^{-1} (for DPDM-stabilized PMMA gels) and 50 s^{-1} (for PHSA-stabilized PMMA gels) to induce structural changes. For the PHSA-stabilized PMMA gels (Case 7 in Table 2.1), we also applied an oscillatory preshear procedure (γ = 120 at 50 s^{-1} each oscillation for a total of 30 *s*) prior to equilibration. We chose high shear rates to avoid shear banding, as shown in the case of 0.033 s^{-1} where regions of non-uniform density were observed in the gels (Fig. 2.5). We also checked for the existence of shear banding in the rheometer using the same shear rates. These combined results suggest the existence of unstable flows consisting of sections of fluid moving at low shear rates. Consequently, for most of the cases listed in Table 2.1, gels were deformed at the high

shear rate of 40 s^{-1}. For gels suspended in pure DOP, rheological instrument constraints limit us to deformations with a shear rate of 5 s^{-1}.

Three independent experiments were performed for each step strain. Gels were photopolymerized immediately after yielding. Image volumes (27.5 × 27.5 × 25 μm^3) were taken at three locations away (distance above the coverslip at 10 μm, 35 μm, 60 μm) from sample boundaries. Image analysis was performed on 96% of the total collected volumes, with the rest rejected due to anomalous, extreme structural heterogeneity that is possibly caused by the deficient initial bonding of the gel to the surface of the shear cell. Centroids of particles in the image volumes were identified in 3D space [40]. The static error in particle location was previously found to be ± 35 nm in the objective plane and ± 45 nm in the axial direction [41]. Using this image processing procedure, we obtain the contact number distribution of each image volume. Particles are considered nearest neighbors if the interparticle separation is less than that of the first minimum in the radial distribution function, $g(r)$.

The static structure factor, $S(q)$, was calculated from particle centroids using $S(q) = \left\langle \left| \frac{1}{N} \sum_{i}^{N} \exp(-i\mathbf{q} \cdot \mathbf{r}_i) \right| \right\rangle$, where $\mathbf{q}$ are the wave vectors chosen in Cartesian coordinates, N is the total number of particles in the system, and $\mathbf{r}_i$ is the distance vector of particle i to the origin. We removed particle centroids near the boundaries to eliminate finite size effects of the image volume [7].

Rheological measurements

Rheological measurements were done using a stress-controlled rheometer (AR-G2, TA Instruments) with a 40 mm parallel steel plate at a gap of 300 μm. The temperature was fixed at

25°C. A solvent trap was fitted over the geometry to reduce solvent evaporation. The samples were presheared at 200 rad/s for 2 minutes and allowed to rest for t_w. For PHSA-stabilized PMMA gels (Case 7 in Table 2.1), the sample was presheared for an additional 30 s at 50 rad/s. To address the inhomogenous shear flow in the parallel disk geometry, we correct our oscillatory rheology and step strain data using the method of Soskey and Winter [42].

The elastic modulus, G', of the gels were measured for strain amplitudes ranging from 0.0001 to 100 at a shear rate of 40 rad/s. The shear rate was reduced to 5 rad/s for samples from Case 2 to obtain measurements of G' at large γ due to the stress limits on the instrument. We checked that wall slip did not affect our results by attaching sandpaper (roughness length scale of ~ 26 μm) to the top and bottom of the rheometer geometry and by changing the geometry gap to 600 μm [43]. We also performed an oscillatory measurement using a 60 mm cone-and-plate geometry. The standard deviation of these measurements for all conditions and all strains (± 40%) is comparable to that of sample-to-sample variability (± 50%).

In order to quantify the degree of gelation arising from the added polystyrene and the photopolymer, we measured the linear oscillatory elastic modulus, G'_{linear}, as a function of the concentration of the depletants, c_{depl}. We take the onset of gelation to occur at $c_{depl} = c_{depl,gel}$, where two distinct power-laws intersect. We include corresponding CLSM images for these data points (Fig. 2.1).

We performed stress relaxation measurements after a nonlinear step strain to determine the Brownian stress of the ruptured gels and to determine the adequacy of the photopolymer arrest time [44]. The Brownian stress, $G_B(t, \gamma)$, is determined as the residual stress immediately after the step strain has been completed, and the hydrodynamic contribution to the stress has ceased (Fig. 2.7). We measured $G_B(t, \gamma)$ for a number of cases listed in Table 1 (except for $\gamma =$

0.5, 1, 20, 30, 40 in Case 1, and γ = 20, 60 in Case 7). To test the performance of the photopolymer, a step strain (γ= 50) was applied (Case 1 from Table 2.1) and the stress relaxation measured after the deformation (Fig. 2.6). After the cessation of the step strain, the stress magnitude remains close to 1.5 Pa for ~10 s. This stress plateau is much longer than the photopolymerization time (< 0.8 s). The comparison shows that the photopolymer arrests structure much more rapidly than the diffusion and reorientation of the gels.

Clustering of particles based on contact number and statistical analysis

We assigned particles to clusters for which the cutoff distance is the location of the first minimum of $g(r)$ of the quiescent gel. Linear regression was used to find the best power-law fit for $G'(\gamma)(2a)^3\langle N_{p,rigid}\rangle$ versus ϕ_{rigid} for each value of z. A chi-squared value was calculated to quantify the agreement between the experimental values and the power-law fit using the relation $\tilde{\chi}_0^2 = \frac{1}{d}\sum_{k=1}^{n}\frac{(O_k - E_k)^2}{E_k}$, where d is the number of degrees of freedom, O_k and E_k are the observed and expected y-axis values, and n is the total number of observations. Larger values of $\tilde{\chi}_0^2$ is a result of significant *disagreement* between the observed and expected distributions [45]. If the value of $\tilde{\chi}_0^2$ is close to 1, there is a significant probability that the measurements follow the expected distribution. We used the same method to obtain a power-law fit of $G_B(t, \gamma)(2a)^3\langle N_{p,rigid}\rangle$ versus ϕ_{rigid} (Fig. 2.7). Variability in the magnitude of the rigid volume fraction arises from sample-to-sample differences, the particular value of the $g(r)$ selected as the cutoff for nearest neighbors, and the number of nearest neighbors used as the rigidity criterion.

Brownian Dynamics simulations and rigidity metrics[*]

Molecular dynamics simulations were conducted using the molecular dynamics package HOOMD-Blue (http://codeblue.umich.edu/hoomd-blue). Particle coordinates are taken from experimental data. All particles are modeled with a soft-core repulsion via the Weeks-Chandler-Anderson potential [46], with a core diameter of 1.06 μm. Particles within the distance defined by the first minimum of the $g(r)$ are bonded with a harmonic approximation of the interaction potential. The spring constant is set at k = 4800, similar to the estimated width of the experimental depletion potential. The equilibrium bond distance is chosen to be the interparticle distance. The simulation was allowed to thermalize for 1 million time steps. The connectivity of the bonded network determined the extent to which particles can locally rearrange and move during the simulations.

Characterization of the rigidity of clusters is done using two metrics: the angular mobility metric and the Fourier shape-matching parameter. Angular mobility for each cluster of particles was measured by calculating the average square displacement of all angles in each cluster as they evolved, and can be quantified using a time-averaged mobility metric, $\langle M \rangle = \frac{2}{N_c(N_c-1)(N_c-2)} \left\langle \sum_i \left| \theta_i(t_0) - \theta_i(t) \right|^2 \right\rangle$, where $\theta_i(t_0)$ and $\theta_i(t)$ are angles between two adjacent bonds in the initial configuration at t_0 and the simulation configuration at time t, and N_c is the number of particles within the cluster. The Fourier parameter is computed from shape descriptors that determine the correlation between the shape of a cluster with the shape at another frame [33]. These descriptors can be used to calculate an order parameter based on the goodness of fit. The relative rigidity of a cluster is measured by the time average of this order parameter,

[*] Brownian Dynamics simulations are performed by Richmond S. Newman.

$<O_F>$, with larger values denoting a more rigid structure. Both parameters were calculated from twenty simulation frames and clusters containing three to one hundred particles.

Results & Discussion

We observe a striking transformation in the microstructure as the applied step strain, γ, is increased. At lower applied strains ($0.5 \leq \gamma \leq 5$), no changes are visually resolved (Fig. 2.2e-h). As the applied strain increases, there is a progression from a dense network at $\gamma = 10$ (Fig. 2.2i) to a disordered, fluid-like suspension by $\gamma = 20$ (Fig. 2.2j). Locally dense clusters form between $\gamma = 30$ to 60 (Fig. 2.2k-n). Over the range of our CLSM observations, $G'(\gamma)$ decreases by almost two orders of magnitude. Despite this large decrease, the G' at $\gamma = 60$ is much greater than that of a suspension of non-interacting particles, for which G' is not measurable when $\gamma > 15$. Inspection of image volumes reveals a significant number of large clusters, even in the large-strain amplitude regime. The potential role of this type of clusters has previously been discussed in the context of thixotropic systems, for which the existence of large intact aggregates at high shear rates was inferred from measurements of the hydrodynamic stresses that were substantially larger than that of hard sphere suspensions [31, 32]. What properties of these residual clusters are correlated with the nonlinear elastic stress?

To address this question, we acquire particle coordinates in 3D and plot the contact number distribution as a function of strain (Fig. 2.8a, inset). Particles are considered to be in adhesive contact if they are within a distance less than that of the first minimum in $g(r)$ (Fig. 2.2a). The breakdown of the network structure in Fig. 2.2e-n is accompanied by a decrease in the mean contact number, $<z>$, by a factor of two as γ increases from 0.5 to 60 (Fig. 2.8a). The modest decrease in $<z>$ is insufficient to explain the observed changes in G', as we address later.

This failure suggests that theories based on the averaged ensemble of all particles in the system cannot fully describe rheological changes in yielding. Instead, it appears that certain subpopulations of particles are responsible for supporting elasticity in the ruptured gel.

We search for candidate subpopulations based on contact number by examining the difference between the contact number distribution for each γ and for the quiescent gel (Fig. 2.8b). The results show a decrease in the fraction of particles with six neighbors ($z = 6$) and a corresponding increase in the number of particles with $z = 2$. These observations are markedly different from proposed models. For example, within micromechanical theories, soft bonds are postulated to be important in yielding [9, 12]. Other experiments suggest shear-induced densification occurs as flow progresses [9, 10]. Neither possibility explains our observations of high strain-rate yielding, since Fig. 2.8b suggests that the principal change in microstructure is caused by the gradual erosion of particles with large z. Thus, it appears that high contact number particles are key determinants of the nonlinear $G'(\gamma)$ of ruptured gels. We hypothesize that these particles are localized in rigid clusters that are load-bearing. As strain-induced yielding proceeds, a reduction in the number of these clusters causes a drop in the $G'(\gamma)$ of the gel.

When we apply the rigidity criterion (configurations with $z \geq z_{iso} = 6$ are considered rigid) to yielded gels, renderings illustrate differences between the rigid microstructure of gels sheared at small ($\gamma = 0.5$) and large strain ($\gamma = 60$). Rigid clusters at $\gamma = 0.5$ span the image volume (Fig. 2.9c), while at $\gamma = 60$, the clusters form only a small subset (Fig. 3d) of the original volume (Fig. 2.9a, b). In addition, we find that the volume fraction of rigidly bonded particles, ϕ_{rigid}, is a strongly decreasing function of γ(Fig. 2.9e). Between $\gamma = 0.5$ and $\gamma = 60$, ϕ_{rigid} drops from 0.08 ± 0.01 to 0.008 ± 0.006. Correspondingly, the mean number of particles in rigid clusters, $\langle N_{p,rigid} \rangle$,

decreases by more than a factor of seven. (Note that the gel volume fraction, ϕ_{gel} = 0.20, is constant for these cases.)

Simulation of the clusters identified from the CLSM images supports that particles with $z \geq z_{iso}$ behave rigidly. We perform Brownian dynamics simulations (HOOMD-Blue) on these clusters by initializing particles from the experimental configurations and using a harmonic spring approximation to connect those in the same cluster [33]. The configurations are allowed to thermalize and the relative rigidity of the clusters is characterized by the average angular mobility parameter, $\langle M \rangle$ (Fig. 2.9f), and Fourier shape-matching parameter (34) (Fig. 2.10). The value of $\langle M \rangle$ drops by nearly three orders of magnitude from $z \geq 1$ to $z \geq 9$, indicating that the rotation of particles is increasingly constrained with large z. Clusters from $z \geq 4$ to $z \geq 6$ experience the largest decrease in $\langle M \rangle$. The simulations support the idea that rigidity in the experimental system can be correlated to the subpopulation of high contact number particles, allowing the effects of rigidity on gel rheology to be studied.

A mechanism for the elasticity of ruptured gels in terms of the mean size and volume fraction of the high contact number clusters can now be hypothesized. Within yielded gels, there exists a distribution of slowly diffusing clusters comprised of particles with large z. The low contact number particles relax from their non-equilibrium, shear-induced configurations rapidly, and are incapable of supporting elastic stress. These floppy modes with $z \leq z_{iso}$ need not be considered in the rheological model for elasticity; the elastic rheology is then a function of the size and number of interacting rigid clusters. To test this idea, we plot the strain-dependent elastic modulus normalized by the cluster volume and thermal energy, $G'(2a)^3\langle N_{p,rigid}\rangle/k_BT$, as a function of $\phi_{\text{rigid}}(\gamma)$ (defined for particles with $z \geq 6$) (Fig. 2.11). The ordinate is based on the classical scaling for hard sphere rheology [35], with the volume of a hard sphere, $V_p \sim (2a)^3$,

replaced by the mean volume of a rigid cluster, $V_{\text{cluster}} \sim (2a)^3 \langle N_{p,rigid} \rangle$. Fig. 4 is generated by plotting non-dimensional variables suggested by the isostaticity approach. These variables obtained from the CLSM microstructural results have no adjustable parameters. The high quality of the correlation suggests that the nonlinear $G'(\gamma)$ is described by the manner in which shear reduces the size and volume fraction of load-bearing clusters. Remnant clusters contribute a Brownian stress that scales as a power law of $\phi_{\text{rigid}}(\gamma)$ with an exponent of 2.7 ± 0.4. This scaling is generated due to the slow relaxation of rigid clusters, mediated by hydrodynamic interactions between clusters. We obtain a similar power-law correlation with the Brownian stress, $G_B(t, \gamma)$, which we measure during stress relaxation after a non-linear step strain deformation [31, 44] (Fig. 2.7). These experiments provide additional support for the hypothesis that structural rigidity is the principal determinant of the stress response of gels ruptured through different types of nonlinear deformation. Because the large amplitude oscillatory deformation of $G'(\gamma)$ and the stress relaxation after step strain, $G_B(t, \gamma)$, differ in the relative contributions of hydrodynamic and Brownian components of the stress, there is scope for rigidity to contribute to these rheological measures in different ways. These differences have potential implications for rheological properties, such as in thixotropic systems [31].

The power-law correlation based on $G'(\gamma)$ and $\phi_{\text{rigid}}(\gamma)$ holds for all samples in Table 2.1. Moreover, the correlation based on the properties of the rigid clusters is statistically much better ($\tilde{\chi}_0^2 = 1.25$, $n = 24$) than the analogous correlation of G' with the ensemble-averaged contact number ($\tilde{\chi}_0^2 = 9.83$, $n = 9$). Here, $\tilde{\chi}_0^2$ is the normalized chi-squared value of the correlation, and n is the number of experimental conditions tested. When we expand the analysis to consider correlations for $z \geq 0$ to $z \geq 9$, we find highly significant correlations for $z \geq 4$ to $z \geq 6$, with values of $\tilde{\chi}_0^2$ that are close to 1 (Fig. 2.11, inset). This rigidity range is also supported by the

simulation results (Fig. 2.9f). Interestingly, these bounds match the z_{iso} for 3D granular matter, which decreases from six to four as friction between particles increases [29]. The lower limit of the rigidity criterion ($z \geq 4$) could be linked to friction and/or non-central, tangential interactions in colloids, which has been previously measured in particle chains [14]. Thus, we propose using $z = 4$ and $z = 6$ as lower and upper bounds for evaluating the rigidity of colloidal gels.

Identification of the role of isostaticity and rigidity in gel elasticity provides a new method to understand and manipulate the viscoelastic properties of soft matter in high strain-rate flows. The general correlation that we show in Fig. 2.11 can be applied to predict colloidal structure in large strain and strain-rate flows that are characteristic in the processing of soft matter. We have shown that nonlinear elasticity is a result of the slow relaxation of rigid and hydrodynamically coupled clusters; it would be interesting to investigate the orientational anisotropy of these clusters along the principal axes of the flow [10] as well as the nature of this hydrodynamic coupling. Our work also demonstrates that rheological properties can be quantitatively predicted using the underlying microstructure of stress-bearing clusters, and introduces new possibilities for the design of soft materials in which the shape of such clusters can be modified. For example, gels with Bernal spiral microstructure [21, 22] might potentially display an even more defined rheological response than that found in this work, because of the structural uniformity imposed by their rigid tetrahelical motif.

Table 2.1. Summary of test cases used in CLSM and rheological measurements

Case	Solvent	ϕ_{gel}	$c_{depl}/c_{depl,gel}$	R_g/a	t_w	γ
1	CHB/decalin/DOP	0.20	10.0	0.077	2 h	0.5, 1, 5, 10, 20, 30, 40, 50, 60
2	Pure DOP	0.13	2.4	0.077	2 h	1, 10, 20, 30, 40
3	CHB/decalin/DOP	0.10	7.3	0.095	15 mins	10, 40
4	CHB/decalin/DOP	0.20	7.3	0.095	15 mins	10, 40
5	CHB/decalin/DOP	0.10	13.7	0.095	15 mins	10, 40
6	CHB/decalin/DOP	0.20	13.7	0.095	15 mins	10, 40
7‡	CHB/decalin/DOP	0.20	10.0	0.049	2 h	20, 60

‡ Presheared gels; details of the procedure are in the Materials and Methods section.

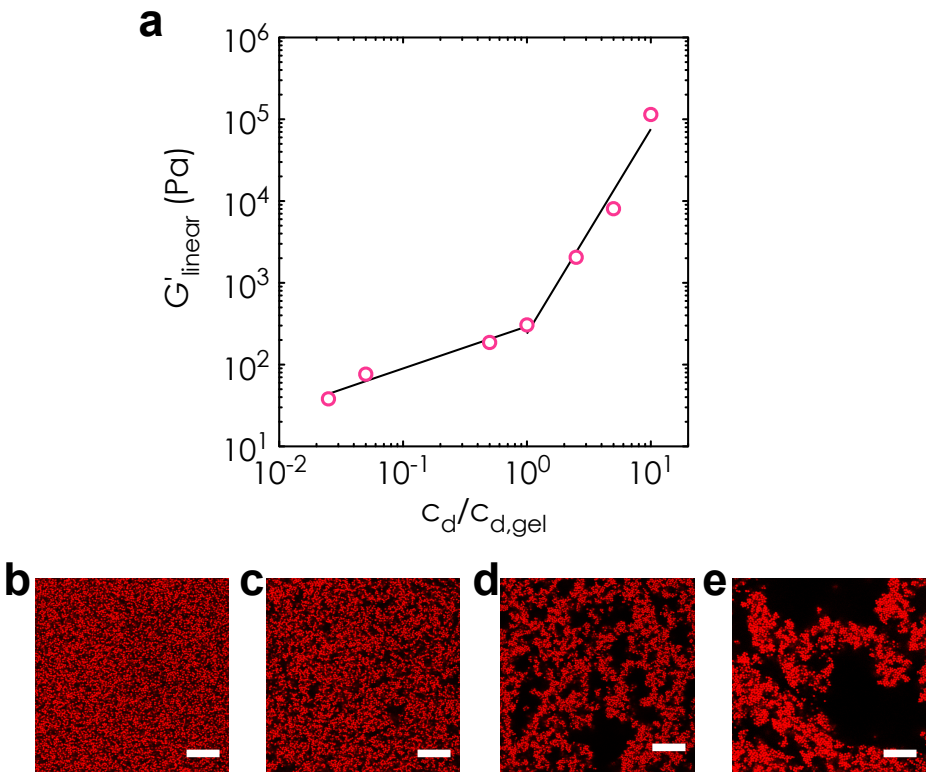

Figure 2.1. Determination of the gelation boundary. a, The linear elastic modulus, G'_{linear}, of the gels as a function of the degree of gelation, $c_d/c_{d,gel}$. Power-law fits are drawn through the data points to illustrate the onset of gelation at $c_d/c_{d,gel} = 1$. Representative CLSM 2D images of samples at b, $c_d/c_{d,gel} = 0.05$; c, $c_d/c_{d,gel} = 0.5$; d, $c_d/c_{d,gel} = 1.0$; and e, $c_d/c_{d,gel} = 10.0$ are also included. Only the data for the solvent mixture (55% cyclohexyl bromide, 10% decalin, and 35% dioctyl phthalate) is shown for clarity. In b-e, scale bars represent 15 μm. This Figure is reprinted with permission from [L.C. Hsiao, R.S. Newman, S.C. Glotzer & M.J. Solomon, *Proc. Natl. Acad. Sci. USA* **109**, 16029-16034 (2012)].

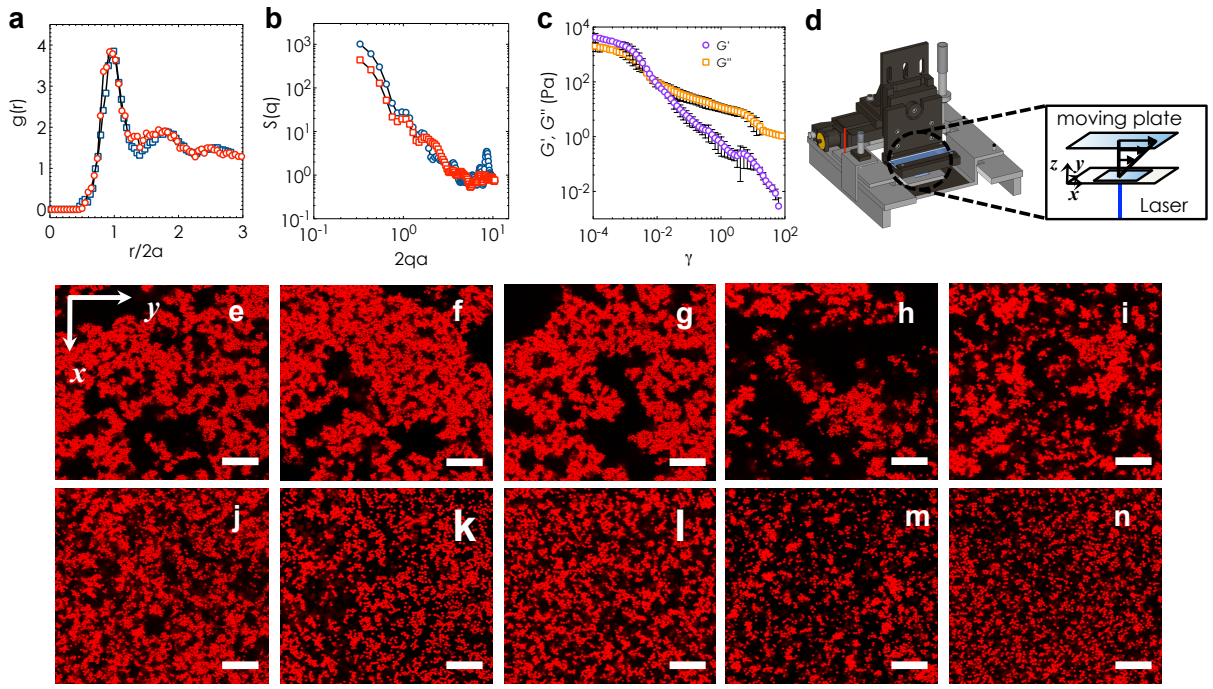

Figure 2.2. Visualization of the structural evolution of colloidal gels undergoing high-rate step strains. a, Radial distribution function, b, structure factor, c, elastic and viscous moduli of quiescently-formed gels. a and b are shown for Cases 1 (blue open squares) and 2 (red open circles) in Table 1, while c is shown for Case 1. d, Schematic of CLSM shearing device and close-up of parallel plates and flow field used in the high-rate step strain experiments. e-n, Representative CLSM 2D images of poly(methyl methacrylate) gels before and after execution of step strain with magnitude γ: e, quiescent structure; f, $\gamma = 0.5$; g, $\gamma = 1$; h, $\gamma = 5$; i, $\gamma = 10$; j, $\gamma = 20$; k, $\gamma = 30$; l, $\gamma = 40$; m, $\gamma = 50$; n, $\gamma = 60$. In e-n, scale bars represent 15 µm. In d and e-n, the x, y, and z-axes are the flow, vorticity, and gradient directions respectively. This Figure is reprinted with permission from [L.C. Hsiao, R.S. Newman, S.C. Glotzer & M.J. Solomon, *Proc. Natl. Acad. Sci. USA* **109**, 16029-16034 (2012)].

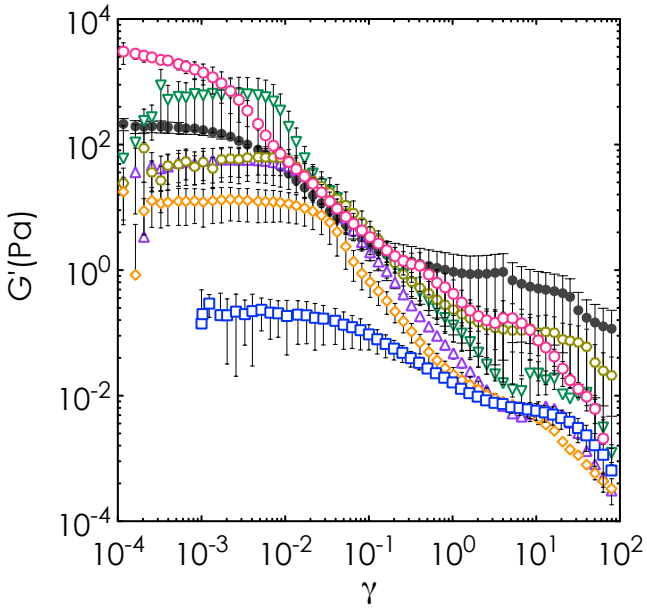

Figure 2.3. Complete oscillatory strain sweep rheology data set. The elastic modulus, G', as a function of the applied oscillatory strain, γ, for all experimental cases. Values of G' have been corrected for the non-homogenous flow imposed by the parallel disk geometry as described in the text. Legend: Case 1 = red open circles; Case 2 = blue open squares; Case 3 = orange open diamonds; Case 4 = olive open hexagons; Case 5 = purple open triangles; Case 6 = green inverted open triangles; Case 7 = grey filled circles. Error bars shown are standard errors of the mean. This Figure is reprinted with permission from [L.C. Hsiao, R.S. Newman, S.C. Glotzer & M.J. Solomon, *Proc. Natl. Acad. Sci. USA* **109**, 16029-16034 (2012)].

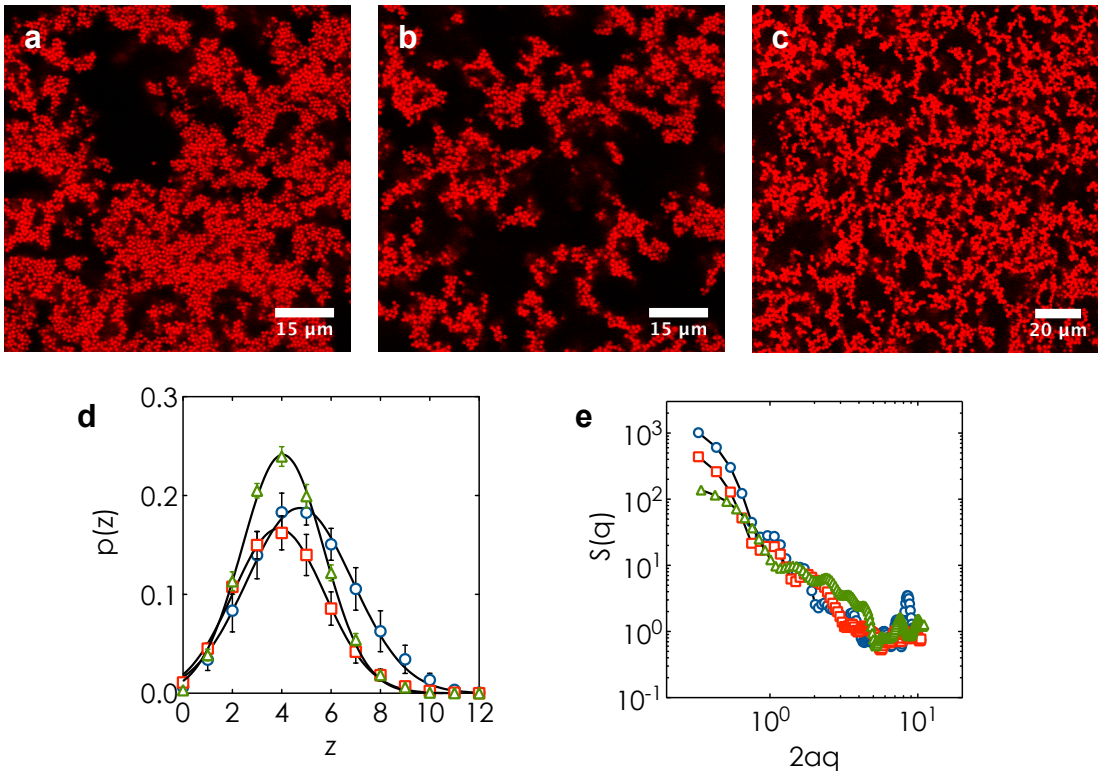

Figure 2.4. Visualization and quantification of initial microstructure at different test conditions. Representative 2D CLSM images of quiescent gels that are used in a, Case 1; b, Case 2; and c, Case 7. Structural differences seen between these gels are quantified with d, the contact number distribution and e, the structure factor. Legend: Case 1 = blue open circles; Case 2 = red open squares; Case 7 = green open triangles. This Figure is reprinted with permission from [L.C. Hsiao, R.S. Newman, S.C. Glotzer & M.J. Solomon, *Proc. Natl. Acad. Sci. USA* **109**, 16029-16034 (2012)].

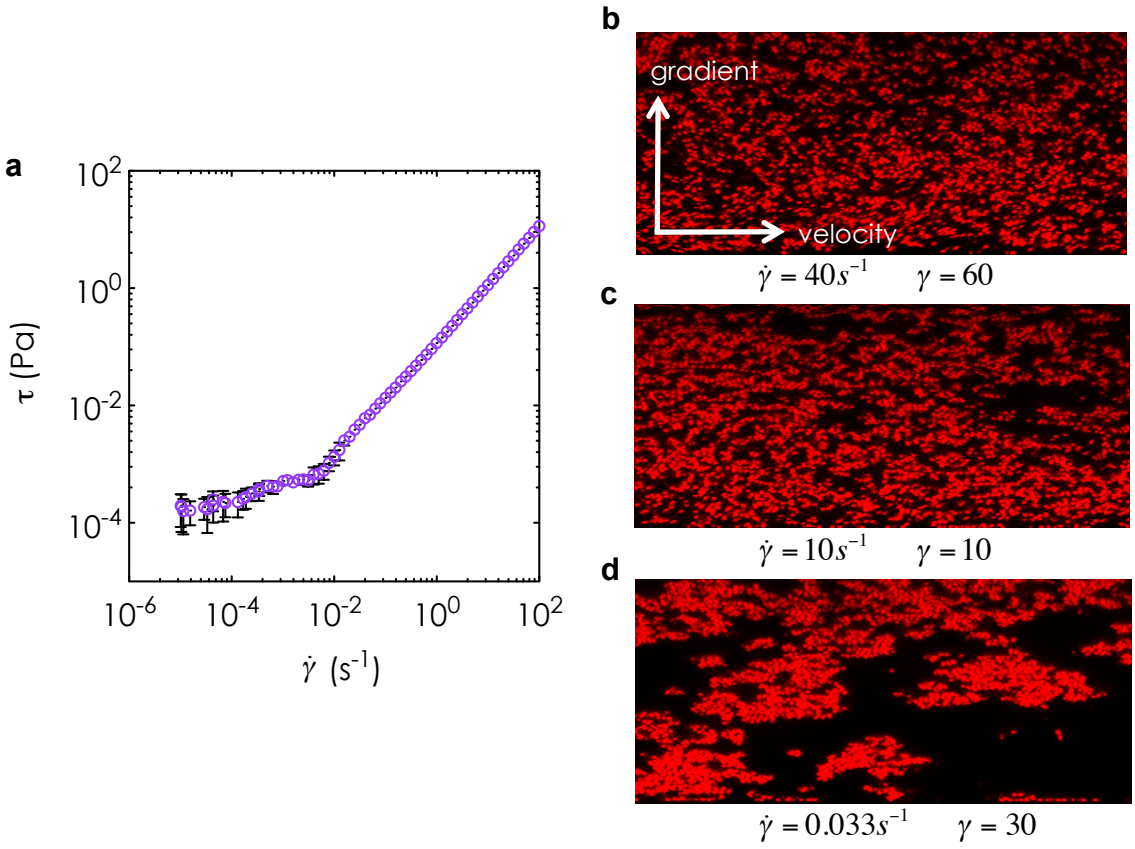

Figure 2.5. Avoiding shear banding using high shear rates. a, Steady-state rheology measuring the shear stress, τ, as a function of shear rate, $\dot{\gamma}$. b-d, CLSM images in the velocity-gradient plane for various applied strains and shear rates. b, $\dot{\gamma}$ = 40 s^{-1}, γ= 60; c, $\dot{\gamma}$ = 10 s^{-1}, γ= 10; d, $\dot{\gamma}$ = 0.033 s^{-1}, γ= 30. Error bars shown in the rheology measurements are standard errors of the mean. This Figure is reprinted with permission from [L.C. Hsiao, R.S. Newman, S.C. Glotzer & M.J. Solomon, *Proc. Natl. Acad. Sci. USA* **109**, 16029-16034 (2012)].

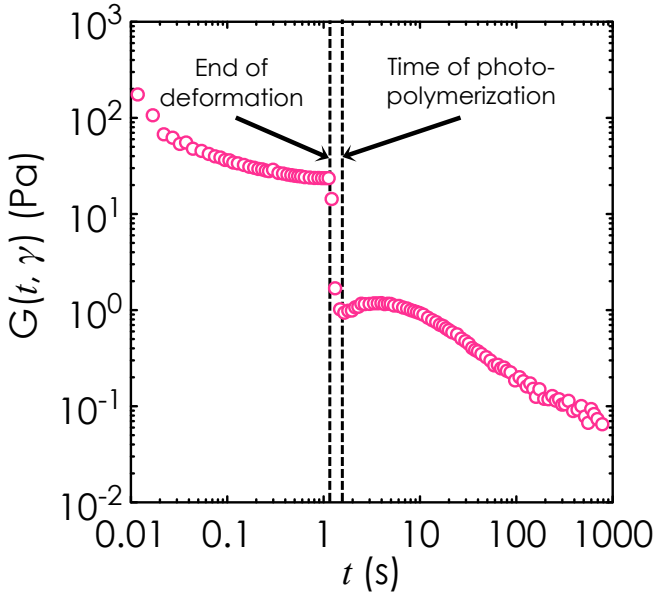

Figure 2.6. Photopolymerization of gels undergoing yielding. Stress relaxation rheological measurements of $G(t, \gamma)$ as a function of time, t, for an applied strain of 50 and shear rate of 40 s^{-1}. Dashed lines indicate the end of the step strain deformation and the arrest time of the photopolymer as labeled. Values of $G(t, \gamma)$ have been corrected for the non-homogenous flow imposed by the parallel disk geometry. This Figure is reprinted with permission from [L.C. Hsiao, R.S. Newman, S.C. Glotzer & M.J. Solomon, *Proc. Natl. Acad. Sci. USA* **109**, 16029-16034 (2012)].

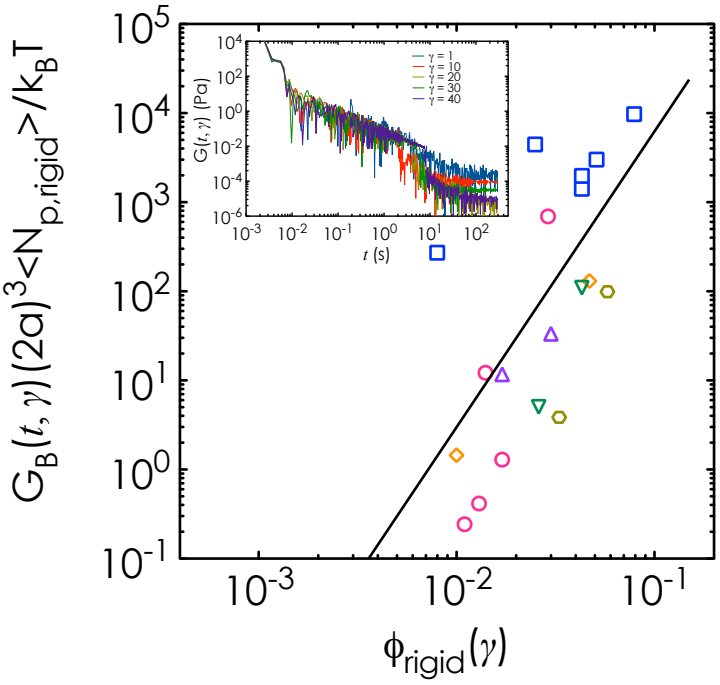

Figure 2.7. Brownian stress from nonlinear stress relaxation as a function of rigid microstructure. Normalized Brownian stress of the gels after application of step strain, $G_B(t, \gamma)(2a)^3\langle N_{p,rigid}\rangle/k_BT$, as a function of the load-bearing volume fraction, ϕ_{rigid}. The experimental data points are fitted to a power law (solid line) using linear regression. Legend: Case 1 = red open circles; Case 2 = blue open squares; Case 3 = orange open diamonds; Case 4 = olive open hexagons; Case 5 = purple open triangles; Case 6 = green open triangles. This Figure is reprinted with permission from [L.C. Hsiao, R.S. Newman, S.C. Glotzer & M.J. Solomon, *Proc. Natl. Acad. Sci. USA* **109**, 16029-16034 (2012)].

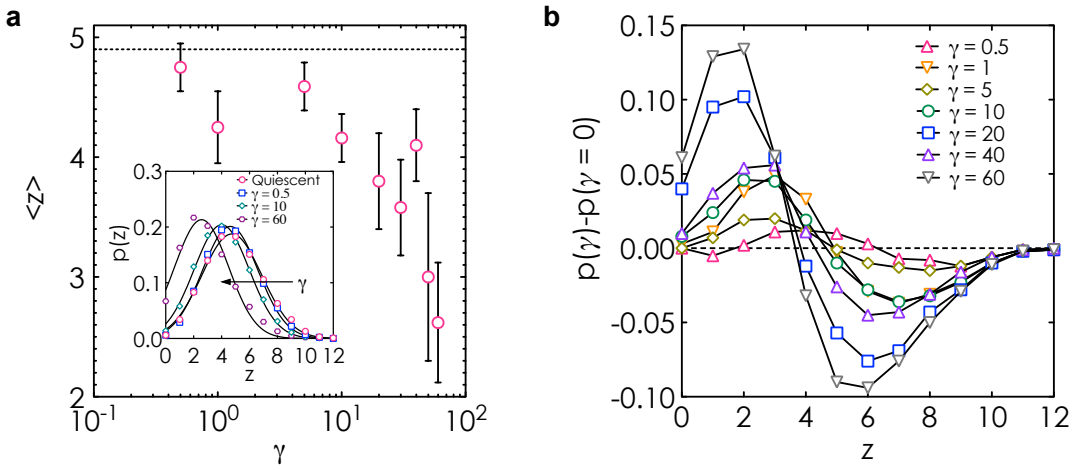

Figure 2.8. Quantification of gel microstructure before and after yielding. a, Changes in the mean contact number, $\langle z \rangle$, as a function of the applied strain, γ. Error bars are obtained from six or more independent measurements. Inset: The contact number distribution of gels as the applied γ increases. Four experimental data sets (γ = 0, 0.5, 10, 60) are shown for clarity. Dashed line represents $\langle z \rangle$ of the quiescent gel. b, Change in the strain-dependent contact number distribution, p(γ), relative to the quiescent distribution, p(γ = 0). Dashed line represents p(γ = 0). Seven experimental data sets are displayed for clarity (γ = 0.5, 1, 5, 10, 20, 30, 40, 50, 60). All of the data shown here are obtained from Case 1. Error bars shown are standard errors of the mean. This Figure is reprinted with permission from [L.C. Hsiao, R.S. Newman, S.C. Glotzer & M.J. Solomon, *Proc. Natl. Acad. Sci. USA* **109**, 16029-16034 (2012)].

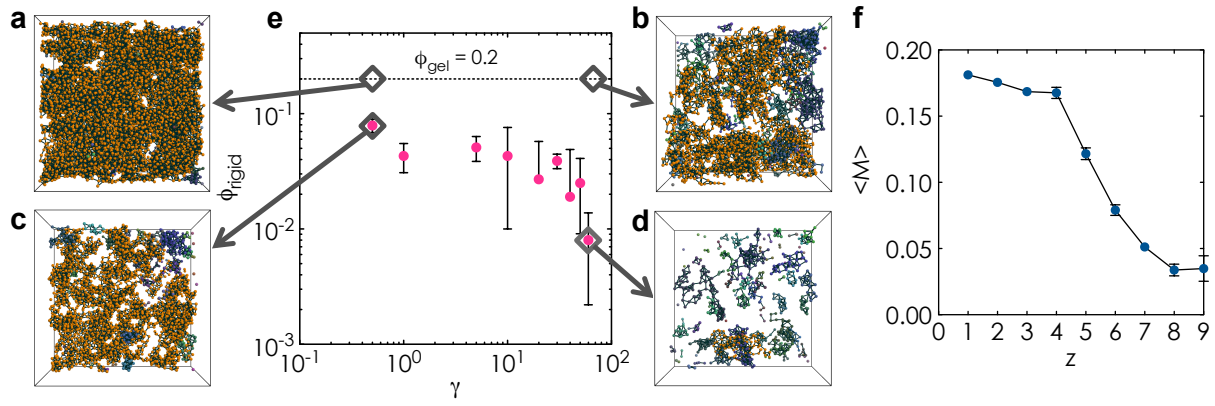

Figure 2.9. Establishing rigid clusters in sheared gels. a-d, Three-dimensional computer renderings showing the difference between the complete network and the load-bearing network for two strains (γ = 0.5, 60). a, Complete network ($z \geq 0$, $\phi_{rigid} = \phi_{gel} = 0.2$) for γ = 0.5; b, Complete network ($z \geq 0$, $\phi_{rigid} = \phi_{gel} = 0.2$) for γ = 60; c, Rigid network ($z \geq 0$, $\phi_{rigid} = 0.08 \pm 0.01$) for γ = 0.5; d, Rigid network ($z \geq 0$, $\phi_{rigid} = 0.008 \pm 0.006$) for γ = 60. Here, ϕ_{gel} is the experimental gel volume fraction and ϕ_{rigid} is the rigid volume fraction as defined for $z \geq 6$. Particles are color-coded according to the clusters they belong to, with orange representing the largest cluster in the volume. These renderings are snapshots of gels as indicated in e, the plot of ϕ_{rigid} as a function of the applied strain γ. f, Angular mobility parameter, $\langle M \rangle$, calculated for $z \geq 1$ to $z \geq 9$. The data shown in a-f are obtained from Case 1. All error bars shown are the standard errors of the mean from independent experimental trials. This Figure is reprinted with permission from [L.C. Hsiao, R.S. Newman, S.C. Glotzer & M.J. Solomon, *Proc. Natl. Acad. Sci. USA* **109**, 16029-16034 (2012)].

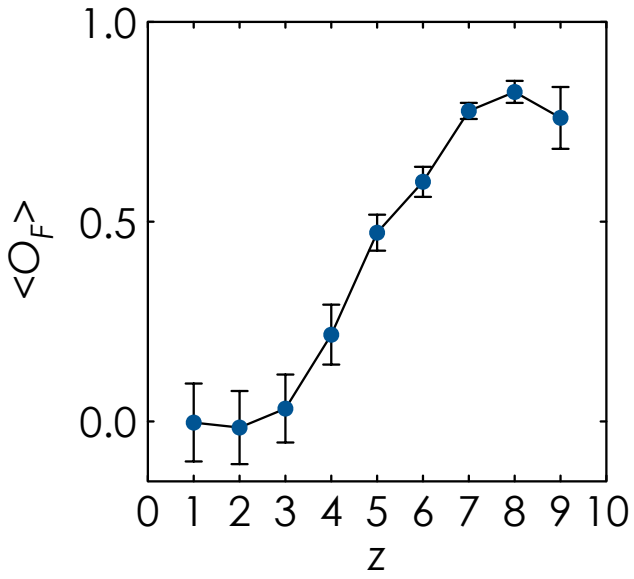

Figure 2.10. Fourier shape-matching parameter. The time-averaged Fourier shape-matching parameter, $\langle O_F \rangle$, as a function of z. The data shown are obtained from Brownian Dynamics simulations of clusters from Case 1. All error bars shown are the standard errors of the mean obtained from simulations derived from experimental configurations. This Figure is reprinted with permission from [L.C. Hsiao, R.S. Newman, S.C. Glotzer & M.J. Solomon, *Proc. Natl. Acad. Sci. USA* **109**, 16029-16034 (2012)].

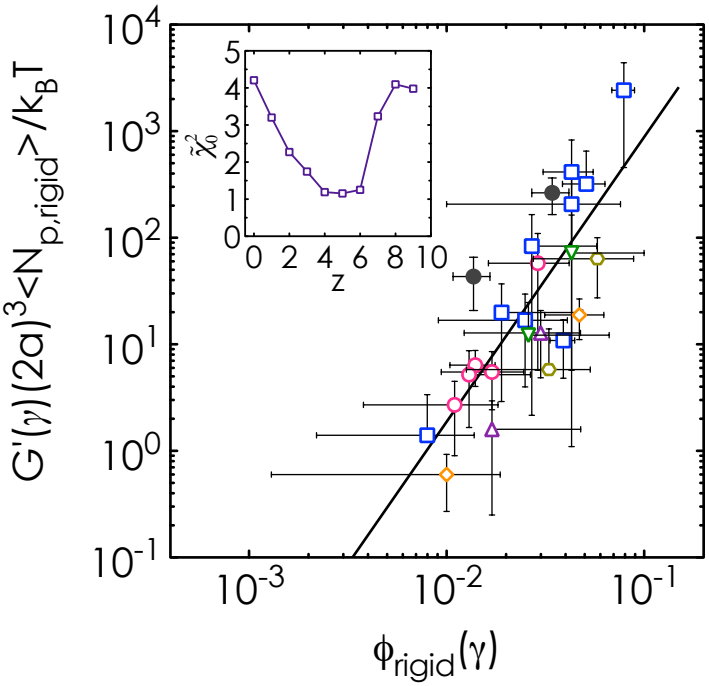

Figure 2.11. Contribution of load-bearing clusters to gel elasticity. Normalized nonlinear elastic modulus of the ruptured gels, $G'(\gamma)(2a)^3<N_{p,rigid}>/k_BT$, as a function of the load-bearing volume fraction, ϕ_{rigid}. Values of G' have been corrected for the non-homogenous flow imposed by the parallel disk geometry. The experimental data points are fitted to a power law (solid line) using linear regression. Vertical error bars are standard errors of the mean from rheology experiments, and horizontal error bars are standard errors of the mean from CLSM structural measurements. Legend: Case 1 = red open circles; Case 2 = blue open squares; Case 3 = orange open diamonds; Case 4 = olive open hexagons; Case 5 = purple open triangles; Case 6 = green inverted open triangles; Case 7 = grey filled circles. Inset: Statistical correlation for testing rigidity hypothesis. The normalized chi-squared value, $\tilde{\chi}_0^2$, is plotted for correlations calculated to include contact numbers from $z \geq 0$ to $z \geq 9$. This Figure is reprinted with permission from [L.C. Hsiao, R.S. Newman, S.C. Glotzer & M.J. Solomon, *Proc. Natl. Acad. Sci. USA* **109**, 16029-16034 (2012)].

References

[1] Zaccarelli E (2007) Colloidal gels: equilibrium and non-equilibrium routes. *J. Phys.: Condens. Matter* **19**: 323101.

[2] Han BY *et al*. (2009) Omnidirectional printing of flexible, stretchable, and spanning silver microelectrodes. *Science* **323:** 1590-1593.

[3] Helgeson ME, Moran SE, An HZ, Doyle PS (2012) Mesoporous organohydrogels from thermogelling photocrosslinkable nanoemulsions. *Nature Mater.* **11:** 344-352.

[4] Drury JL, Mooney DJ (2003) Hydrogels for tissue engineering: scaffold design variables and applications. *Biomater.* **24**: 4337-4351.

[5] Lu Y *et al*. (1997) Continuous formation of supported cubic and hexagonal mesoporous films by sol-gel dip-coating. *Nature* **389:** 364-368.

[6] Chen YL, Schweizer KS (2004) Microscopic theory of gelation and elasticity in polymer-particle suspensions. *J. Chem. Phys.* **120:** 7212-7222.

[7] Lu PJ *et al.* (2008) Gelation of particles with short-range attraction. *Nature* **453:** 499-504.

[8] Eberle APR, Wagner NJ, Castañeda-Priego R (2011) Dynamical arrest transition in nanoparticle dispersions with short-range interactions. *Phys. Rev. Lett.* **106**: 105704.

[9] Rajaram B, Mohraz A (2010) Microstructural response of dilute colloidal gels to nonlinear shear deformation. *Soft Matter* **6**: 2246-2259.

[10] Masschaele K, Vermant J (2009) Direct visualization of yielding in model two-dimensional colloidal gels subjected to shear flow. *J. Rheol.* **53:** 1437-1460.

[11] Koumakis N, Petekidis G (2011) Two step yielding in colloidal gels: transition from gels to attractive glasses. *Soft Matter* **7:** 2456-2470.

[12] Chan HK, Mohraz A (2012) Two-step yielding and directional strain-induced strengthening in dilute colloidal gels. *Phys. Rev. E* **85**: 041403.

[13] Potanin AA, De Rooij R, Van den Ende D, Mellema J (1995) *J. Chem. Phys.* **102**: 5845-5853.

[14] Pantina JP, Furst EM (2005) Elasticity and critical bending moment of model colloidal aggregates. *Phys. Rev. Lett.* **94:** 138301.

[15] Studart AR, Amstad E, Gauckler LJ (2011) Yielding of weakly attractive nanoparticle networks. *Soft Matter* **7**: 6408-6412.

[16] Bonn D, Tanaka H, Coussot P, Meunier J (2004) Ageing, shear rejuvenation and avalanches in soft glassy materials. *J. Phys.: Condens. Matter* **16**: S4987-S4992.

[17] Besseling R, Isa L, Petekidis G, Cates ME, Poon WCK (2010) Shear banding and flow-concentration coupling in colloidal glasses. *Phys. Rev. Lett.* **105:** 268301.

[18] Besseling R, Weeks ER, Schofield AB, Poon WCK (2007) Three-dimensional imaging of colloidal glasses under steady shear. *Phys. Rev. Lett.* **99:** 028301.

[19] Cheng X, McCoy JH, Israelachvili JN, Cohen I (2011) Imaging the microscopic structure of shear thinning and thickening colloidal suspensions. *Science* **333**: 1276-1279.

[20] Maxwell JC (1864) On the calculation of the equilibrium and stiffness of frames. *Phil. Mag.* **27**: 294-299.

[21] Mossa S, Sciortino F, Tartaglia P, Zaccarelli E (2004) Ground state clusters for short-range attractive and long-range repulsive potentials. *Langmuir* **20**: 10756-10763.

[22] Campbell AI, Anderson VJ, van Duijneveldt JS, Bartlett P (2005) Dynamical arrest in attractive colloids: the effect of long-range repulsion. *Phys. Rev. Lett.* **94**: 208301.

[23] Haji-Akbari A. *et al*. (2009) Disordered, quasicrystalline and crystalline phases of densely packed tetrahedra. *Nature* **462:** 773-778.
[24] Zaccone A, Gentili D, Wu H, Morbidelli M, Del Gado E (2011) Shear-driven solidification of dilute colloidal suspensions. *Phys. Rev. Lett.* **106:** 138301.
[25] Seth JR, Mohan L, Locatelli-Champagne C, Cloitre M, Bonnecaze RT (2011) A micromechanical model to predict the flow of soft particle glasses. *Nature Mater.* **10**: 838-843.
[26] Ovarlez G, Barral Q, Coussot, P (2010) Three-dimensional jamming and flows of soft glassy materials. *Nature Mater.* **9:** 115-119.
[27] Broedersz CP, Mao X, Lubensky TC, MacKintosh FC (2011) Criticality and isostaticity in fibre networks. *Nature Phys.* **7:** 983-988.
[28] Liu AJ, Nagel SR (1998) Jamming is not just cool any more. *Nature* **396**: 21-22.
[29] van Hecke M (2010) Jamming of soft particles: geometry, mechanics, scaling and isostaticity. *J. Phys.: Condens. Matter* **22**: 033101.
[30] Wyart M, Liang H, Kabla A, Mahadevan L (2008) Elasticity of floppy and stiff random networks. *Phys. Rev. Lett.* **101:** 215501.
[31] Dullaert K, Mewis J (2005) Stress jumps on weakly flocculated dispersions: steady state and transient results. *J. Coll. Int. Sci.* **287:** 542-551.
[32] Masschaele K, Fransaer F, Vermant J (2011) Flow-induced structure in colloidal gels: direct visualization of model 2D suspensions. *Soft Matter* **7**: 7717-7726.
[33] Nguyen TD, Philips CL, Anderson JA, Glotzer SC (2011) Rigid body constraints realized in massively-parallel molecular dynamics on graphics processing units. *Comp. Phys. Comm.* **182**: 2307-2313.
[34] Keys AS, Iacovella CR, Glotzer SC (2011) Characterizing structure through shape matching and applications to self-assembly. *Annu. Rev. Condens. Matter Phys.* **2:** 263-285.
[35] Mewis J, Wagner NJ (2012) in *Colloidal Suspension Rheology* (Cambridge Univ Press, Cambridge).
[36] Kogan M, Dibble CJ, Rogers RE, Solomon MJ (2008) Viscous solvent colloidal system for direct visualization of suspension structure, dynamics and rheology. *J. Coll. Int. Sci.* **318**: 252-263.
[37] Dullens RPA, Claesson M, Derks D, van Blaaderen A, Kegel WK (2003) Monodisperse core-shell poly(methyl methacrylate) latex colloids. *Langmuir* **19**: 5963-5966.
[38] Shereda LT, Larson RG, Solomon MJ (2008) Local stress control of spatiotemporal ordering of colloidal crystals in complex flows. *Phys. Rev. Lett.* **101**: 038301.
[39] Shah AA *et al.* (2012) Liquid crystal order in colloidal suspensions of spheroidal particles by direct current electric field assembly. *Small* **8:** 1551-1562.
[40] Crocker JC, Grier DG (1996) Methods of digital video microscopy for colloidal studies. *J. Coll. Int. Sci.* **179:** 298-310.
[41] Dibble CJ, Kogan M, Solomon MJ (2006) Structure and dynamics of colloidal depletion gels: coincidence of transitions and heterogeneity. *Phys. Rev. E* **74:** 041403.
[42] Soskey PR, Winter HH (1984) Large step shear strain experiments with parallel-disk rotational rheometers. *J. Rheol.* **28**: 625-645.
[43] Buscall R (2010) Letter to the editor: wall slip in dispersion rheometry. *J. Rheol.* **54**: 1177-1183.

[44] Kaffashi B, O'Brien V, Mackay ME, Underwood SM (1997) Elastic-like and viscous-like components of the shear viscosity for nearly hard sphere, Brownian suspensions. *J. Coll. Int. Sci.* **187**: 22-28.
[45] Taylor JR (1997) in *An Introduction to Error Analysis - The Study of Uncertainties in Physical Measurements* (Univ Science Books, Sausalito).
[46] Weeks JD, Chandler D, Andersen HC (1971) Role of repulsive forces in determining the equilibrium structure of simple liquids. *J. Chem. Phys.* **54**: 5237-5247.

CHAPTER 3

Role of shear-induced dynamical heterogeneity in the nonlinear rheology of colloidal gels[†]

Abstract

We report the effect of flow-induced dynamical heterogeneity on the nonlinear elastic modulus of weakly aggregated colloidal gels that have undergone yielding by an imposed step strain deformation. The gels are comprised of sterically stabilized poly(methyl methacrylate) colloids interacting through short-ranged depletion attractions. When a step strain of magnitude varying from γ = 0.1 to 80 is applied to the quiescent gels, we observe the development of a bimodal distribution in the single-particle van Hove self-correlation function. This distribution is consistent with the existence of a fast and slow subpopulation of colloids within sheared gels. We show that the predictive power of recent mode coupling theory [17] that connects strain-dependent nonlinear elasticity to localization length is significantly improved by incorporating the properties of the slow, rigid subpopulation of the colloids into the modeling. The text in this chapter is reprinted with permission from [L.C. Hsiao, H. Kang, K.H. Ahn & M.J. Solomon, *submitted* (2014)].

Introduction

[†] Dr. Heekyoung Kang (Seoul National University) performed a majority of the experiments and part of the data analysis. She is a co-author in this work.

Weak, reversible colloidal gels are important model systems for studying the underlying physics of attractive interactions, slow dynamics, and yielding transitions. They exhibit structural and dynamical heterogeneity [1-4], ergodic/nonergodic transitions [5-8], and complex linear and nonlinear flow properties [9-11]. In contrast to the caging mechanism that gives rise to slow dynamics in dense colloidal suspensions, the elasticity imparted by gels arises from three-dimensional network structures that are assembled by attractive bonding between individual colloids. The reversible fluid-to-gel transition brought on by short-ranged attractions is well described by mode coupling theory (MCT), which models the dynamics of collective modes of the disordered gel structure [12, 13]. The gel structure factor has been obtained from a two-component polymer interaction model (PRISM) and has been used with MCT to predict its zero-frequency elastic modulus. A key finding is that the elastic modulus is inversely related to the ensemble-averaged single particle localization length [14]. While linear rheological experiments show good agreement with the MCT-PRISM prediction for gels at low volume fractions [15], significant discrepancies have been observed in weak, transient systems [16]. The discrepancy has been attributed to the MCT assumption of a homogenous fluid, in which the large cluster length scales associated with heterogeneous gel structure have been neglected [17]. A prefactor corresponding to the average number of colloids in each cluster has been used to reconcile the theoretical predictions with experimental measurements [14, 17, 18].

Structural and dynamical heterogeneity in quiescent gels are correlated, particularly in the cluster regime close to the gelation transition [3, 4, 19, 20]. Heterogeneity can also arise from yielding, where sequences of bond rupture occur beyond a critical applied strain or stress. Nonlinear rheological phenomenon such as shear banding [21], slip [22], and strain-induced hardening/softening [23] are often encountered in flows that are sufficiently large to cause

yielding. Strong flows perturb the nonequilibrium free energy landscape and affect slow colloidal dynamics in surprising ways [24]. For example, nonergodic clusters exhibit ballistic motion at short time scales [25], followed by a gradual relaxation of internal stress after flow ceases [26]. Despite the importance of structural and dynamical heterogeneity in microscopic models, no experiments probe the effect of flow on dynamical heterogeneity and its role in the nonlinear rheological behavior of yielded gels. In this Letter, we report experiments that show the existence of strain-induced dynamical heterogeneity in colloidal gels. The dynamical heterogeneity takes a simple form comprised of slow and fast subpopulations of colloids. We show that the MCT-PRISM theory agrees well with experimental measurements of nonlinear elasticity when we consider that only the slow, hydrodynamically rigid subpopulation of colloids contributes to the elastic component of the stress.

Materials and Methods

Confocal microscopy imaging of gels under shear

The gels studied are comprised of poly(methyl methacrylate) (PMMA) spheres (diameter, $2a$ = 900 nm ± 6%) sterically stabilized with diphenyl-dimethyl siloxane, dyed with fluorescent Nile Red [2, 4], and dispersed in a refractive-index and density matched solvent (55/10/35 vol% cyclohexyl bromide/decalin/dioctyl phthalate, $\Delta n = 1.0 \times 10^{-3}$, $\Delta\rho/\rho = 4.0 \times 10^{-3}$). This solvent composition was selected to optimize observation of dynamical changes within experimental time scales (solvent viscosity, $\eta = 2.7 \times 10^{-2}$ Pa·s, diffusivity $D = 1.8 \times 10^{-14}$ m^2/s). We add non-adsorbing polystyrene (molecular weight = 900,000 g/mol) where the radius of gyration, R_g = 38 ± 2 nm, is determined by static light scattering (DAWN EOS, Wyatt Technology, 690 nm laser). The small polystyrene molecule is added at a dilute concentration (overlap concentration c* =

0.007 ± 0.001 g/ml, c/c* = 0.31 ± 0.05) to the PMMA colloids, generating gels with moderate volume fraction ($\phi = 0.15$) and short-ranged attractions ($\xi = R_g/a = 0.08$). Tetrabutylammonium chloride is added at a concentration of 1 μM (zeta potential, $\zeta \leq 10$ mV [2], Debye length, $\kappa^{-1} =$ 70 nm) to provide charge screening. The net interparticle potential is estimated at $U \sim (-2.2 \pm 0.5)\ k_BT$ (k_B is the Boltzmann constant, and temperature $T = 298$K) and is comparable to weak colloidal gels [4, 27].

The dynamics of the gels are monitored at waiting times of t_w = 10 min, 30 min, 1 hour and 2 hours after sample loading. Representative confocal images of the effect of waiting time on the microstructure of these gels are shown in Fig. 3.1(a)-(d). The mean-squared displacement (MSD) values and the van Hove self-correlation functions plotted in the figure show that the colloids become increasingly arrested over the course of 2 hours. Fig. 3.1(e) shows that the MSD of the gels attain a plateau localization length of $\langle \Delta x2(t) \rangle = (6.5 \pm 2.0) \times 10\text{-}4$ μm2 at tw = 2 hours. Similarly, Fig. 3.1(f) shows that the single particle displacement probability is narrow and non-Gaussian. The asymmetry in the van Hove self-correlation function at the longest time characterized indicates that there is some center-of-mass drift occurring at that instance. These quiescent gels are cluster-like and exhibit non-Gaussian dynamics typical of weakly-aggregated gels [4], but without a bimodal distribution that is sometimes observed close to the gelation transition [3, 20].

Gel samples are loaded into a custom-built shearing device set at a gap of 120 μm [2, 28] and mounted on a confocal laser-scanning microscope (Leica SP2, 100x, 1.4 numerical aperture oil immersion objective). The gels are allowed to rest for 2 hours in the shear cell, and step strains of various magnitudes ($\gamma = 0.1, 0.6, 6.0, 30, 80$) are applied at a shear rate of 40 s^{-1} (Péclet number, $Pe = 1300$). The high shear rate is chosen to avoid shear banding [2]. Single particle

dynamics of the sheared gels are tracked over a total period of 130 s with a delay time, t, of 0.652 s. A small center-of-mass drift of specimens is addressed with a constant velocity correction. Three independent samples are analyzed for each strain, except for $\gamma = 0.6$ where only one replication was available for analysis because of large image center-of-mass drift velocities. The resulting mean-squared displacement (MSD) of sheared gels at each γ is determined with respect to the velocity and vorticity directions of the applied flow [29]. The static error in the MSD sets the lower bound on the MSD due to instrument and environmental fluctuations. A control experiment on an immobile, photopolymerized gel sample [2] establishes this lower bound at 3.20×10^{-4} μm^2. Because of backflow at high strains (γ = 30 and 80) that is predominantly in the flow direction, we wait up to an additional 5 minutes after the step strain to acquire images in these cases, and analyze single particle dynamics in only the vorticity direction. The backflow observed is reminiscent of the elastic recoil reported for other complex fluids undergoing nonlinear flow [30, 31]. In Fig. 3.2, we show the complete dataset for the van Hove self-correlation for all applied strains (γ = 0.1, 0.6, 6.0, 30, and 80) and five lag times (t = 1.30 s, 4.56 s, 9.78 s, 20.2 s, and 30.0 s). The distributions broaden with the applied deformation and are relatively time-independent, except for the case of γ = 80 where the distributions widen with time. An anomalous measurement at γ = 6.0 and t = 30.0 s is included in the data set but excluded from further analysis. The pixel size for measurements at all strains is 97 nm except for γ = 0.6, for which the pixel size is 60 nm.

Rheological characterization of the nonlinear elastic modulus

The nonlinear elastic modulus of the yielded colloidal gels is measured using a stress-controlled rheometer (AR-G2, TA Instruments) with a 40 mm parallel steel plate geometry (gap

= 500 μm). A solvent trap is used to minimize evaporation of the volatile solvent. Gels are presheared at 200 rad/s for 2 minutes and allowed to equilibrate for 2 hours prior to measurements. The strain-dependent elastic modulus, G'(γ), is measured using oscillatory stress sweep experiments performed at four different angular frequencies (ω = 0.1, 1, 10, 40 rad/s, Fig. 3.3). The dependence of $G'(\gamma)$ on ω and the relative similarity of the linear elastic and viscous moduli at low γ, G' and G'', show that the gels are weak, consistent with the strength of pair attractions in this system. As a basis for comparison with MCT-PRISM, which predicts the zero-frequency elastic modulus of gels in both the linear and nonlinear regime, we normalize the experimentally measured $G'(\gamma)$ at different ω by the linear plateau value, G' (Fig. 3.3, inset).

Results and Discussion

Fig. 3.4(a) and 3.4(b) show representative images of gels imaged at h = 60 μm above the coverslip after applying a small (γ = 0.6) and large (γ = 80) step strain. While the yielded structures appear visually similar, the dynamical signatures at each applied strain are very different from each other. The application of step strain results in an increase in the one-dimensional MSD, measured in the vorticity direction, $\langle \Delta x^2(t) \rangle$, relative to the unsheared gels. Over the duration of the measurement, the MSD is approximately constant, particularly for small step strains (γ = 0.1 – 30). The plateau is the mean squared localization length shown in Fig. 3.4(c). Quiescent gels exhibit a mean squared localization length at $\langle \Delta x^2(t) \rangle = (6.5 \pm 2.0) \times 10^{-4}$ μm^2. At t > 9.78 s, the functionality seen in some of the MSD curves (γ = 0.1 – 30) is due to the loss of linked trajectories at long times for the subset of particles that diffuse out of the field of view. At γ = 80, the sheared samples display subdiffusive motion with a MSD with a power law exponent of 0.75 ± 0.01. The increase in MSD of particles in the sheared gels is an indication

that increasing the magnitude of the applied step strain results in increased delocalization of colloids within the samples.

The emergence of a distinctive, shear-induced dynamical heterogeneity accompanies the increase in $<\Delta x^2(t)>$ as a function of γ. The self-part of the one-dimensional van Hove correlation function, $G_s(x,t) = \frac{1}{N}\left\langle \sum_{i=1}^{N} \delta\left(x + x_i(t=0) - x_i(t)\right)\right\rangle$, characterizes the probability distribution of single-particle displacements, where N is the total number of particles. This quantity is computed from the colloidal trajectories and plotted for low, intermediate, and high γ at t = 9.78 s in Fig. 3.5. This particular time point is chosen as a balance between data quality, which favors short times, and measurement in the plateau regions of the MSD, which favors longer times. (Plots of $G_s(x,t)$ for all γ and t are available in Fig. 3.2). Free particles experiencing Brownian fluctuations exhibit a normal distribution in the van Hove self-correlation function:

$$G_s^g(x,t) = \sqrt{\frac{1}{2\pi\left\langle \Delta x^2(t)\right\rangle}} \exp\left[\frac{-x^2}{2\left\langle \Delta x^2(t)\right\rangle}\right] \qquad (3.1)$$

The variance of the distribution, σ^2, is related to the MSD through $\left\langle \Delta x^2(t)\right\rangle = \sigma^2$. Deviation from a Gaussian distribution in $G_s(x,t)$ signifies departure from free particle behavior. A narrow, non-Gaussian function is seen in Fig. 3.5(a) for quiescent gels at t = 9.78 s. The distribution is nearly time-independent, consistent with the particle localization that is characteristic of dynamical arrest in gels. Applying a step strain deformation results in a superimposed bimodal distribution that is functionally distinct from the quiescent $G_s(x,t)$, as seen in Fig. 3.5(b) – (d). The bimodal distributions found in the yielded gels are absent from the quiescent gels. This bimodality indicates two subpopulations of particles with different MSD values [3, 20, 32]. Bimodal Gaussian fits are used to distinguish fast particles (dashed lines in Fig. .5) from slow

particles (solid lines in Fig. 3.5) based on the discontinuous slope in $G_s(x,t)$. The value of $\Delta G_s(x,t)/\Delta x$ is computed for neighboring data points and a deviation of a factor of ten is assigned as the cutoff between slow and fast subpopulations.

Fig.3.5 shows that the measured distributions are well represented by the Gaussian functions, $G_s^g(x,t)$. The width and the relative contributions of the two modes to the van-Hove self correlation functions vary considerably with the step strain magnitude. At γ = 0.1, the variance of the slow subpopulation, σ^2_{slow}, differs little from the quiescent gel (Fig. 3.5(b)). As the amplitude of the step strain increases, the mobilities of both the slow and fast subpopulations of particles increase. This increase is seen as a broadening of the distributions as a function of γ for both subpopulations (Fig. 3.5(c) and (d)). The variances of the distributions (both σ^2_{slow} and σ^2_{fast}) are equivalent to the MSD of the subpopulations. We therefore separate the MSD values of fast and slow particles, $<\Delta x^2_{\text{fast}}(t)>$ and $<\Delta x^2_{\text{slow}}(t)>$, based on σ^2_{slow} and σ^2_{fast} and plot them in Fig. 3.6. The relative contributions of the slow and fast populations are quantified by the area under the two distributions, A_{slow} and A_{fast}, normalized by the total area A_{t} (Fig. 3.6, inset). The contribution of the fast subpopulation is small compared to the overall distribution.

The displacement of fast particles remains approximately constant throughout all applied γ. The mobility is about 40% of that expected for a free particle (Fig. 3.4(c)), suggesting that fast particles consist of free particles or very small clusters that diffuse rapidly. The mobility of the slow subpopulation increases with γ, with MSD values that increase by nearly two orders of magnitude between γ = 0.1 and γ = 80. This implies that slow colloids belong to the subpopulation that is most affected by the applied strain. These combined observations suggest that strain-induced yielding of gels is accompanied by two dynamical changes. In the first change, which is already seen at γ = 0.1, the single dynamical population present in the colloidal

gel bifurcates into subpopulations with fast and slow dynamics. The fast colloids displace nearly as free particles whereas the slow colloids have mobility that remains unchanged relative to the original quiescent population of colloids. The second change is seen as the strain is further increased, where the relative contributions of the fast and slow populations to the van Hove self-correlation function shifts toward the fast subpopulation. In addition, the mobility of the slow population itself increases as particles in this subpopulation become increasingly delocalized.

It is interesting to compare these observations about colloidal dynamics with previous studies of structural evolution upon yielding. These structural studies have shown that the contact number distribution in yielded gels changes with strain in a way that is consistent with the erosion of rigid clusters [2, 33], in which the abundance of high contact number colloids is depleted as strain is increased while the abundance of low contact number colloids increases. The remnant high contact number particles are sequestered in rigid, dense clusters and are responsible for the finite elastic modulus of yielded gels. These earlier measurements are in accord with the present work if the low contact number colloids from the structural measurements are identified with the fast subpopulation, and if the high contact number colloids are identified with the slow subpopulation. As the rigid clusters are eroded by the applied step stain, their size decreases and their mobility increases, consistent with the data shown in Fig. 3.6. Linking the structural and dynamic heterogeneity of yielded colloidal gels in this way has strong implications for the nonlinear elastic modulus of the gels, which we now explore through rheological measurements and application of recent results from MCT-PRISM [17].

MCT-PRISM predicts the zero-frequency elasticity of short-ranged attractive colloidal gels [17]. The result is an expression that relates the strain-dependent elastic modulus, $G'_{micro}(\gamma)$, to the strain-dependent single-particle localization in the sample, $\langle \Delta r^2(\gamma) \rangle$:

$$\frac{G'_{micro}(\gamma)(2a)^3}{k_BT} = 2.32\frac{\phi a^2}{\langle \Delta r^2(\gamma)\rangle} \tag{3.2}$$

Here, $<\Delta r^2(\gamma)> = 3<\Delta x^2(\gamma)>$ is the mean-squared strain-induced localization length. The theoretical predictions are normalized by the zero-frequency elastic modulus, $G'_{micro}(0)$, which is calculated from the mean-squared localization length of the quiescent gel shown in Fig. 3.1(c). Fig. 4 shows that the theoretical prediction for $G'_{micro}(\gamma)/G'_{micro}(0)$ deviates significantly from the experimental data, with underprediction at low strains and overprediction at high strains.

The strain-dependent localization length in equation (3.2) is computed for an ensemble average of all colloids in the sheared gels. However, the dynamical heterogeneity shown in Fig. 3.5, combined with the nearly free-particle motion of the fast colloids in Fig. 3.6, suggest that the fast subpopulation does not contribute to the nonlinear elastic modulus of the yielded gel. We therefore test a simple revision of the MCT-PRISM in equation (3.2) to reflect a case in which the contribution to elasticity arises only from the subpopulation of colloids that is slow and rigid. The modified expression predicts the nonlinear elastic modulus, $G'_{slow}(\gamma)$, by accounting for the strain-dependent volume fraction of structurally rigid clusters, $\phi_{rigid}(\gamma)$, in addition to their slow dynamics, $<\Delta r^2_{slow}(\gamma)>$, with the following relation:

$$\frac{G'_{slow}(\gamma)(2a)^3}{k_BT} = 2.32\frac{\phi_{rigid}(\gamma)a^2}{\langle \Delta r^2_{slow}(\gamma)\rangle} \tag{3.3}$$

This expression consists of two components: 1) The localization length of the yielded gel is defined as that from the slow subpopulation of colloids from Fig. 3.6; 2) The volume fraction of colloids contributing to the nonlinear elasticity is taken as the high contact number subpopulation as the gel, compiled for the results of this work and of Ref. [2] and plotted in Fig. 3.7. These values of $\phi_{rigid}(\gamma)$ are obtained by fitting a stretched exponential function to samples used in [2]. The incorporation of $\phi_{rigid}(\gamma)$ into equation (3.3) addresses the effect of rapid structural relaxation

of the mobile subpopulation and provides an accurate depiction of the 3D structural landscape immediately after the cessation of flow. Ref. [2] found that the decrease in ϕ_{rigid} is a general function of γ for depletion gels ($0.375 \leq c/c^* \leq 1.1$) tested at large strain deformations ($0.5 \leq \gamma \leq 60$) and in the volume fraction range $0.10 \leq \varphi \leq 0.20$. This range of conditions includes the gel of the present study. We further checked the consistency of this relation with the gels used in this study by a direct measurement of the value of ϕ_{rigid} at $\gamma = 6.0$ using the methods of [2]. We find that the measurement for this study agrees with the full correlation of Ref. [2] to within experimental error (Fig. S4). The exponential fit of data in Fig. 3.7 takes a compressed form of $\phi_{rigid}(\gamma) = 0.060 \exp\left[-(\gamma/35)^{1.5}\right]$ and is used in equation (3.3).

We find that equation (3.3), reflecting contribution from just the slow/rigid colloids, significantly improves the agreement between theory and experiment (Fig. 3.8, solid line). The largest improvement is seen at both low and high strains. At low applied strains, slow colloids are more localized than the full population, giving rise to an increased modulus prediction. The decrease in elastic modulus in the revised model at high strain is due to two effects: the slow subpopulation is highly delocalized (Fig. 3.6), and the percentage of slow/rigid colloids contributing to the modulus is very small due to shear-induced cluster erosion. The combination of these factors are key to the improvement of theoretical predictions in Fig. 3.8. We emphasize that, after the modification of the MCT-PRISM result to resolve just the slow subpopulation of colloids in the gel, all inputs for equation (3.3) are available from direct experimental measurements and that there are no adjustable parameters in the comparison shown in Fig. 3.8.

In this work, we show that yielded colloidal gels display a distinctive form of dynamical heterogeneity involving two classes of particles. The dynamics of the fast subpopulation is similar to that of free particles. As the applied deformation is increased, the mobility of the slow

subpopulation progressively increases. Application of MCT-PRISM based on the complete ensemble of dynamics cannot predict the nonlinear elastic modulus of the gels. However, if the MCT-PRISM result is expressed in a form where only the slow, rigid subpopulation of colloids contributes to the elasticity, then excellent agreement between MCT-PRISM, the measured dynamical heterogeneity, and the measured elasticity is obtained. These results point to the importance of strain-induced dynamical heterogeneity in the nonlinear rheological response of colloidal gels, and suggest scope for connection of these two quantities in a variety of dense colloidal systems with slow dynamics, for example in soft particle glasses [34] and in shear thickening fluids where hydrocluster formation is important.

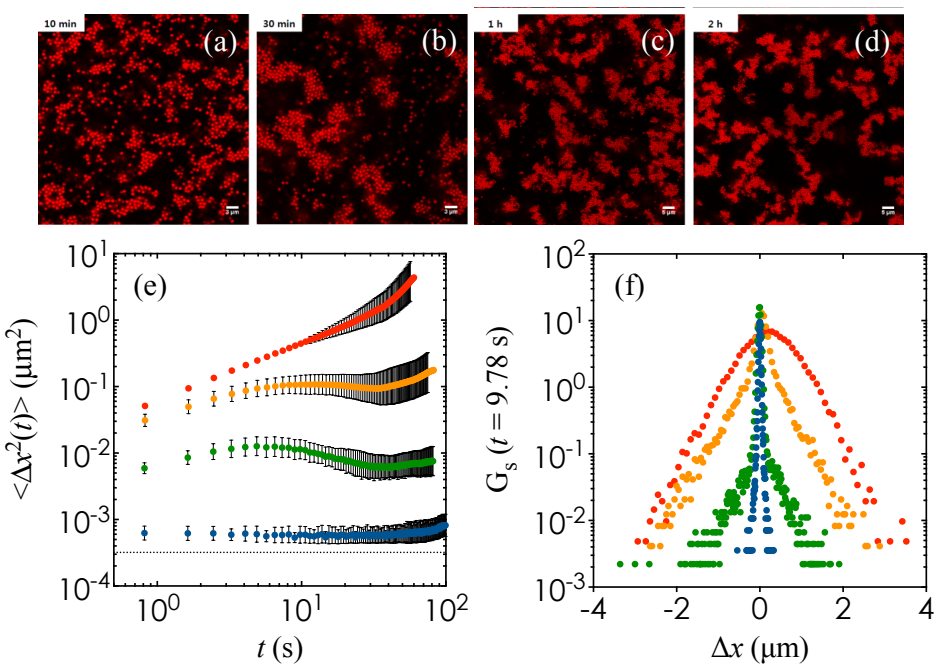

Figure 3.1. Representative 2D confocal images of quiescent gels at (a) t_w = 10 min, (b) t_w = 30 min, (c) t_w = 1 hour, and (d) t_w = 2 hours after sample loading. Scale bars represent 3 μm. In (e), the MSD of the gels at t_w = 10 min (red), 30 min (orange), 1 hour (green), and 2 hours (blue) are shown. Error bars are standard deviations from independent measurements. The dashed line shows the static noise floor of the instrument. The van Hove self-correlation of the gels at t_w = 10 min (red), 30 min (orange), 1 hour (green), and 2 hours (blue) are shown in (f). This Figure is reprinted with permission from [L.C. Hsiao, H. Kang, K.H. Ahn & M.J. Solomon, *submitted* (2014)].

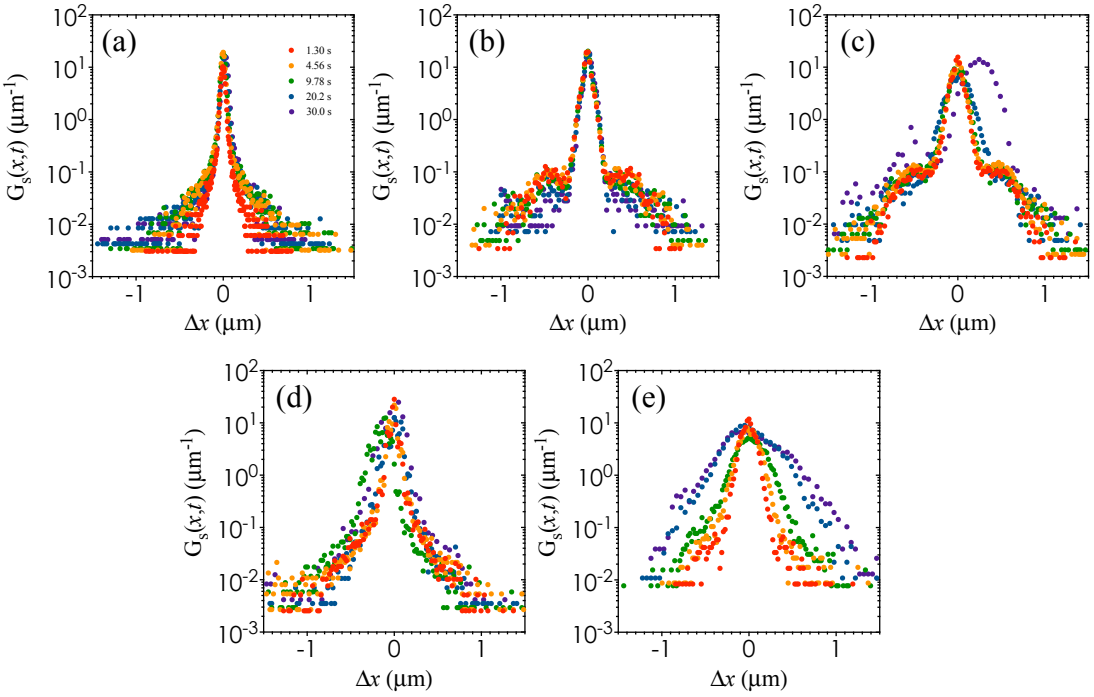

Figure 3.2. Self-part of van Hove correlation for all strains: (a) γ = 0.1, (b) γ = 0.6, (c) γ = 6.0, (d) γ = 30, and (e) γ = 80. In each plot, five lag times are shown: t = 1.30 s (red), 4.56 s (orange), 9.78 s (green), 20.2 s (blue), and 30.0 s (purple). This Figure is reprinted with permission from [L.C. Hsiao, H. Kang, K.H. Ahn & M.J. Solomon, *submitted* (2014)].

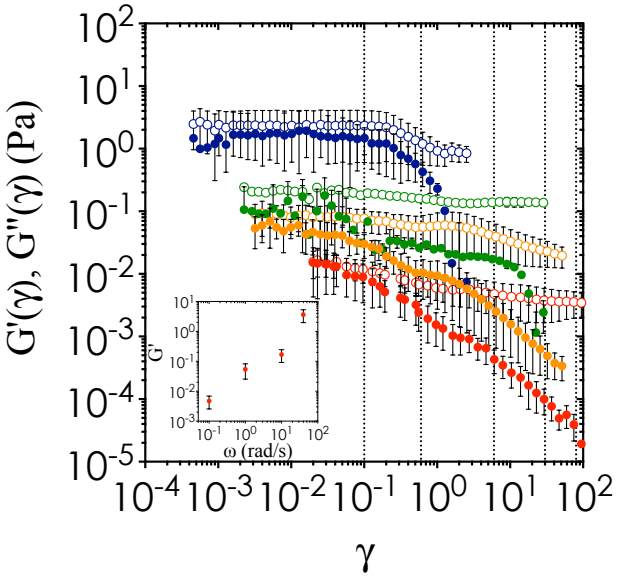

Figure 3.3. Oscillatory stress sweep data at an angular frequency ω = 0.1 rad/s (red), 1.0 rad/s (orange), 10 rad/s (green), and 40 rad/s (blue). Closed symbols represent G'(γ) and open symbols represent G"(γ). Inset: Linear plateau value, G', plotted as a function of ω. Error bars are standard error of the mean from 3 independent measurements. This Figure is reprinted with permission from [L.C. Hsiao, H. Kang, K.H. Ahn & M.J. Solomon, *submitted* (2014)].

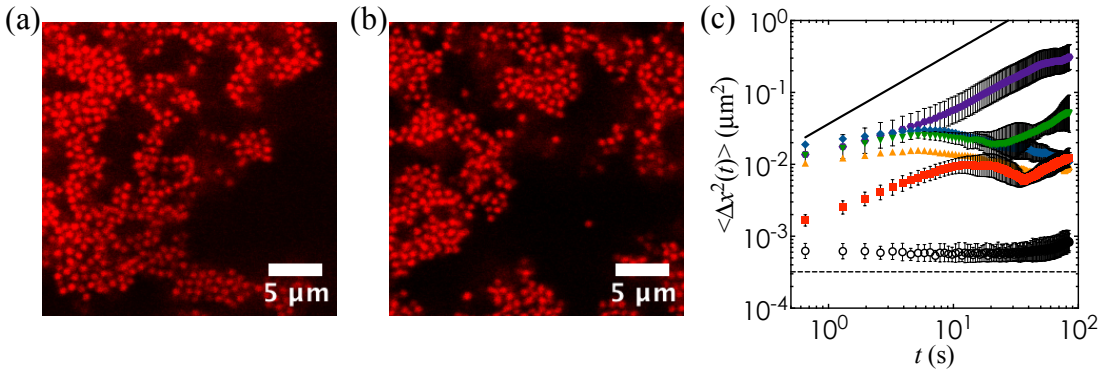

Figure 3.4. Representative 2D confocal images of colloidal gels after applying (a) γ = 0.6 and (b) 80 at $\dot{\gamma} = 40s^{-1}$ in a shearing device. (c) Evolution of $<\Delta x^2>$ as a function of t from a completely arrested gel state (black open symbols) to a completely fluidized suspension (solid line), with the following applied deformations: γ = 0.1 (red), γ = 0.6 (orange), γ = 6.0 (green), γ = 30 (purple), and γ = 80 (brown). Dashed line represents the static noise level obtained from a photopolymerized sample. Error bars shown here are standard deviations from 3 independent measurements. This Figure is reprinted with permission from [L.C. Hsiao, H. Kang, K.H. Ahn & M.J. Solomon, *submitted* (2014)].

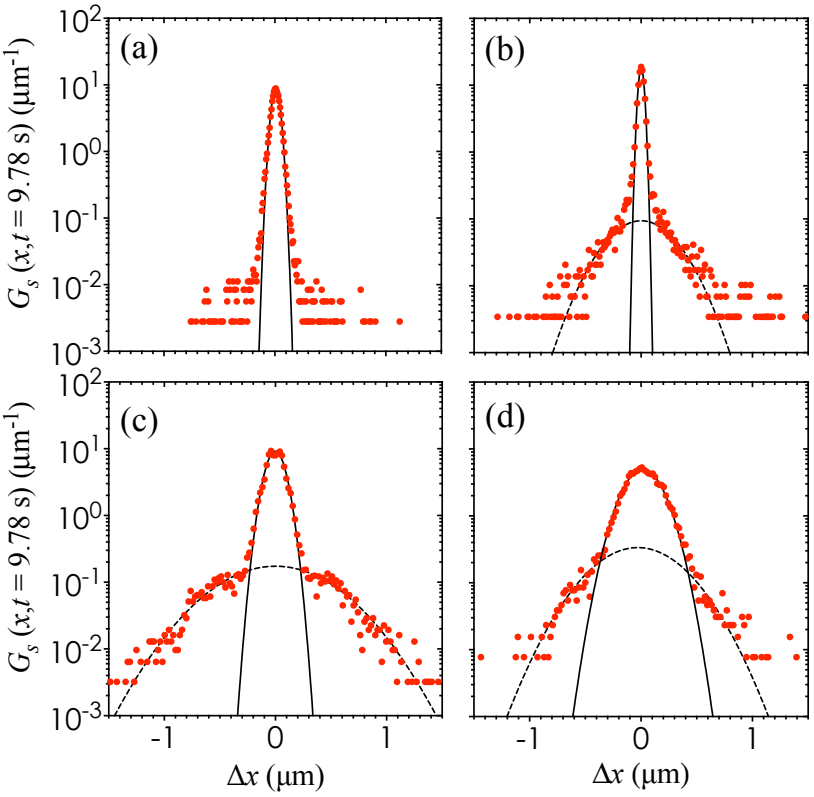

Figure 3.5. Superimposed bimodal single particle displacement distributions of sheared colloidal gels showing slow and fast subpopulations. Comparison between the $G_s(x,t = 9.78\ \text{s})$ of (a) quiescent colloidal gels and that of gels sheared at (b) $\gamma = 0.1$, (c) $\gamma = 6.0$, and (d) $\gamma = 80$. Gaussian distributions are fitted to the slow (solid line) and fast (dashed line) subpopulation of particles. This Figure is reprinted with permission from [L.C. Hsiao, H. Kang, K.H. Ahn & M.J. Solomon, *submitted* (2014)].

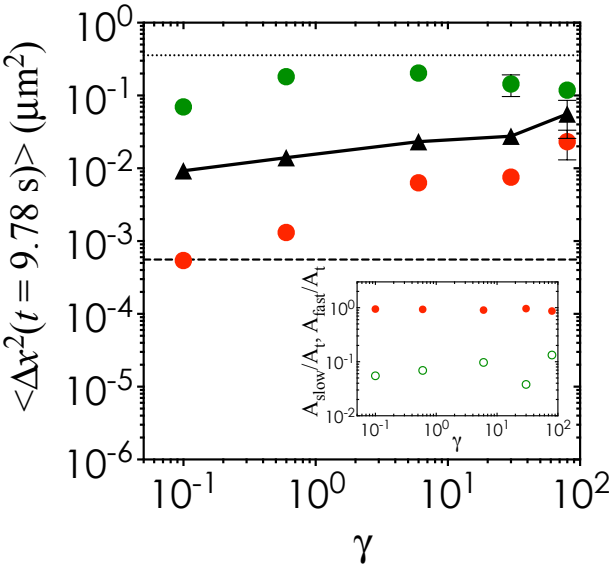

Figure 3.6. MSD curves for the overall dynamics (black triangles) versus the slow (red circles) and fast subpopulation (green circles) of particles in sheared colloidal gels at t = 9.78 s. Error bars shown are standard deviations. A solid line is drawn through the overall dynamics to guide the eye. The free particle upper limit (dotted line) and the MSD of a quiescent gel (dashed line) are also shown. Inset: Relative contribution of the slow (red filled circles) and fast (green open circles) colloids, quantified as the area under the distributions in Fig. 3.5, as a function of strain. This Figure is reprinted with permission from [L.C. Hsiao, H. Kang, K.H. Ahn & M.J. Solomon, *submitted* (2014)].

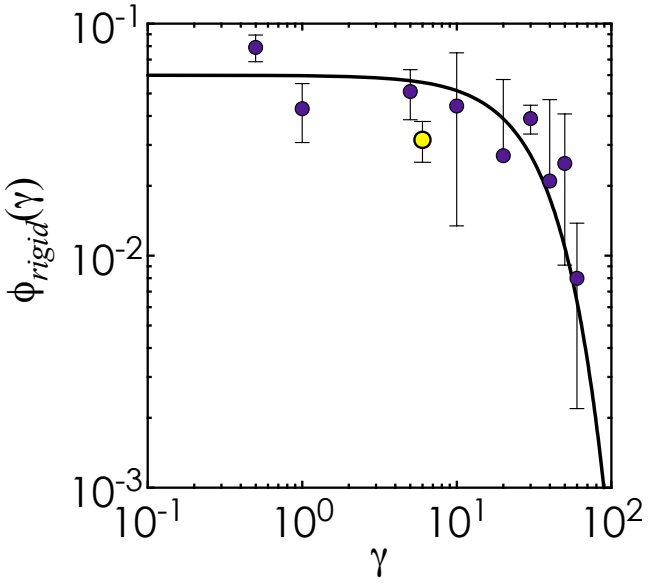

Figure 3.7. Strain-dependent volume fraction of slow/rigid clusters after yielding, obtained from Ref. [2] (purple) and this work at $\gamma = 6.0$ (yellow). Error bars are standard error of the mean from 3 independent measurements. The solid line shows the exponential decay fitting for the data points. This Figure is reprinted with permission from [L.C. Hsiao, H. Kang, K.H. Ahn & M.J. Solomon, *submitted* (2014)].

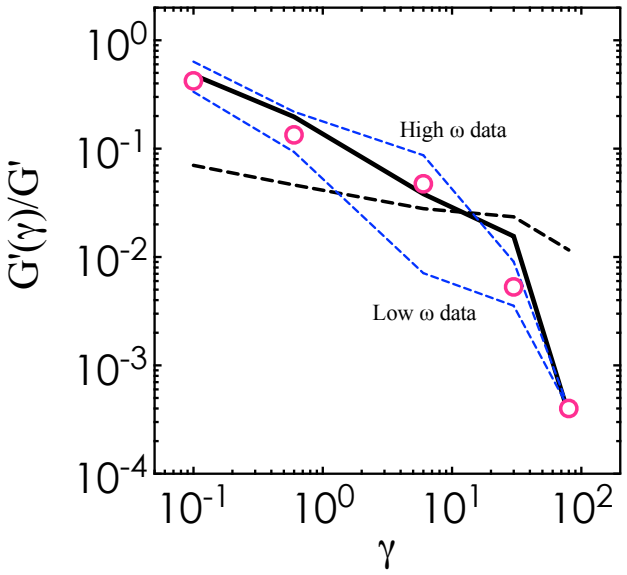

Figure 3.8. Comparison of experimental elastic modulus (red open circles) with high and low frequency bands (blue dashed lines) to theoretical predictions from classical MCT-PRISM (black dashed line). The modified MCT-PRISM predictions from equation (3.3) are shown as a black solid line. This Figure is reprinted with permission from [L.C. Hsiao, H. Kang, K.H. Ahn & M.J. Solomon, *submitted* (2014)].

References

[1] C. P. Royall, S. R. Williams, T. Ohtsuka and H. Tanaka. *Nat. Mater.* **7**, 556 (2008).
[2] L. C. Hsiao, R. S. Newman, S. C. Glotzer and M. J. Solomon. *Proc. Natl. Acad. Sci. U.S.A.* **109**, 16029 (2012).
[3] A. Puertas, M. Fuchs and M. Cates. *Phys. Rev. E* **67**, 31406 (2003).
[4] C. J. Dibble, M. Kogan and M. J. Solomon. *Phys. Rev. E* **74**, 041403 (2006).
[5] A. P. R. Eberle, N.J. Wagner and R. Castañeda-Priego. *Phys. Rev. Lett.* **106**, 105704 (2011).
[6] E. Zaccarelli and W. C. K. Poon. *Proc. Natl. Acad. Sci. U.S.A.* **106**, 15203 (2009).
[7] F. Sciortino, S. Mossa, E. Zaccarelli and P. Tartaglia. *Phys. Rev. Lett.* **93**, 055701 (2004).
[8] S. Ilett, A. Orrock, W. C. K. Poon and P. N. Pusey. *Phys. Rev. E* **51**, 1344 (1995).
[9] J. C. Conrad, H. M. Wyss, V. Trappe, S. Manley, K. Miyazaki, L. J. Kaufman, A. B. Schofield, D. R. Reichman and D. A. Weitz. *J. Rheol.* **54**, 421 (2010).
[10] M. Laurati, G. Petekidis, N. Koumakis, F. Cardinaux, A. B. Schofield, J. M. Brader, M. Fuchs and S. U. Egelhaaf. *J. Chem. Phys.* **130**, 134907 (2009).
[11] N. Koumakis and G. Petekidis. *Soft Matter* **7**, 2456 (2011).
[12] J. Bergenholtz, W. C. K. Poon and M. Fuchs. *Langmuir* **19**, 4493 (2003).
[13] T. R. Kirkpatrick and P. G. Wolynes. *Phys. Rev. A* **35**, 3072 (1987).
[14] Y. L. Chen and K.S. Schweizer. *J. Chem. Phys*. **120**, 7212 (2004).
[15] H. Guo, S. Ramakrishnan, J. L. Harden and R. L. Leheny. *Phys. Rev. E* **81**, 050401 (2010).
[16] H. Guo, S. Ramakrishnan, J. L. Harden and R. L. Leheny. *J. Chem. Phys.* **135**, 154903 (2011).
[17] S. A. Shah, Y. L. Chen, K. S. Schweizer and C. F. Zukoski. *J. Chem. Phys.* **119**, 8747 (2003).
[18] S. Ramakrishnan, V. Gopalakrishnan and C. F. Zukoski. *Langmuir* **21**, 9917 (2005).
[19] C. J. Dibble, M. Kogan and M. J. Solomon. *Phys. Rev. E* **77**, 050401(R) (2008).
[20] Y. Gao and M. L. Kilfoil. *Phys. Rev. Lett.* **99**, 078301 (2007).
[21] A. Fall, J. Paredes and D. Bonn. *Phys. Rev. Lett.* **105**, 225502 (2010).
[22] P. Ballesta, R. Besseling, L. Isa, G. Petekidis and W. C. K. Poon. *Phys. Rev. Lett.* **101**, 258301 (2008).
[23] C. O. Klein, H. W. Spiess, A. Calin, C. Balan and M. Wilhelm. *Macromolecules* **40**, 4250 (2007).
[24] V. Kobelev and K. S. Schweizer. *J. Chem. Phys.* **123**, 164902 (2005).
[25] B. Chung, S. Ramakrishnan, R. Bandyopadhyay, D. Liang, C. F. Zukoski, J. L. Harden and R. L. Leheny. *Phys. Rev. Lett.* **96**, 228301 (2006).
[26] L. Mohan, R. Bonnecaze and M. Cloitre. *Phys. Rev. Lett.* **111**, 268301 (2013).
[27] P. J. Lu, E. Zaccarelli, F. Ciulla, A. B. Schofield, F. Sciortino and D. A. Weitz. *Nature* **453**, 7194 (2008).
[28] L. T. Shereda, R.G. Larson and M.J. Solomon. *Phys. Rev. Lett.* **101**, 038301 (2008).
[29] J. C. Crocker and D.G. Grier. *J. Coll. Interf. Sci.* **179**, 298 (1996).
[30] M. I. Smith, R. Besseling, M. E. Cates and V. Bertola. *Nat. Comm.* **1**, 114 (2010).
[31] J. Vermant, P. Moldenaers and J. Mewis. *J. Rheol.* **38**, 1571 (1994).
[32] W. K. Kegel and A. van Blaaderen. *Science* **287**, 290 (2000).
[33] J. D. Park and K. H. Ahn. *Soft Matter* **9**, 11650 (2013).
[34] A. Zaccone, H. Wu and E. Del Gado. *Phys. Rev. Lett.* **103**, 208301 (2009).

CHAPTER 4

A model colloidal gel for coordinated measurements of force, structure, and rheology[‡]

Abstract

We introduce a model gel system in which colloidal forces, structure, and rheology are measured by balancing the requirements of rheological and microscopy techniques with those of optical tweezers. Sterically stabilized poly(methyl methacrylate) (PMMA) colloids are suspended in cyclohexane (CH) and cyclohexyl bromide (CHB) with dilute polystyrene serving as a depletion agent. A study of the optical trap strength, rheology, and microscopic structure of the gels as a function of CH/CHB solvent composition identifies the conditions for which these measurements can be applied to characterize gel properties. The results indicate that a solvent comprising of 37% weight fraction CH (w_{CH} = 0.37) provides sufficient refractive index contrast to enable optical trapping, while maintaining good confocal imaging quality and minimal sedimentation effects on the bulk rheology. At this condition, and at a depletant concentration c = 8.64 mg/mL (c/c^* = 0.81), results from optical trapping in a dilute sample show that 50% of bonds rupture at (3.3 ± 0.5) pN. The linear strain-dependent elastic modulus of the corresponding gel (ϕ = 0.20) is G' = (1.8 ± 0.6) Pa, and the mean contact number of the colloids in the gel

[‡] Kathryn A. Whitaker (University of Delaware) is a co-author in this work.

structure is $\langle z \rangle = 5.4 \pm 0.1$. The development of this model colloidal gel system yields a concomitant characterization of the interparticle forces, microstructure, and bulk rheology in a single experimental system, thereby allowing the simultaneous comparison of these different measures. The text in this chapter is reprinted with permission from [L.C. Hsiao, K.A. Whitaker, M.J. Solomon & E.M. Furst, *submitted* (2014)].

Introduction

The solid-like elastic properties in colloidal gels, which have significant technological and scientific applications [1, 2], are a result of the three-dimensional stress-bearing structures that are formed by physical or chemical attraction between the individual components of the network [3, 4]. The short range of the interactions used to induce gelation and distinct separation of bound and unbound states between colloids is analogous to physical or chemical bonds between molecules and macromolecules. Bond rupture occurs when a sufficiently large force is applied to overcome the deep potential wells. This phenomenon is known as yielding, in which structural evolution such as local rearrangement [5], bond and cage breakage [6], and flow anisotropy occur [7, 8]. These complex structural changes are manifest in the yield stress and other rheological measures such as the nonlinear creep compliance [9] and the relaxation modulus [10]. The microscopic origins of rheological phenomenon are commonly probed through a combination of rheometry and characterization of the local structure and dynamics, either by direct visualization [11-14] or by scattering methods [15-19].

Micromechanical models seek to predict the rheological properties of gels in shear flow based on the transient microstructure and were originally developed for fractal gels at low volume fractions [20-22]. Current models show system-specific discrepancies in the power-law

scaling between nonlinear rheology and interparticle attraction [23, 24]. Despite the importance of the colloid-level forces that give rise to gelation and the viscoelastic response in shear flow, none of these scaling laws accounts for the spectrum of forces and relaxation time scales responsible for bond rupture [25, 26]. Instead, models rely on the athermal force limit of rupture as an input [23], where the maximum slope of the potential is used to predict the force required for colloids to escape from the potential minimum. For instance, the athermal limits of the van der Waals attraction and depletion interaction encountered in many colloidal systems can be analytically obtained from classical derivations at dilute limits [27]. Despite its simplicity, the assumption of a singular force that is responsible for bond rupture is problematic because of the stochastic nature of bond breaking [28]. External fields (such as gravity or an applied strain acting on a colloidal gel) can lower the energy barrier [29, 30], making it possible for bonds to rupture at a force below the athermal limit. A realistic micromechanical model should account for the effect of field-induced thermal fluctuations on the probability of bond rupture.

Testing such theoretical models requires working with an experimental model system in which interparticle bond strength can be measured along with rheological characterization. Direct manipulation of colloids using optical and magnetic tweezers for instance, is a suitable method to determine the distribution of particle-level forces responsible for linear and nonlinear rheology [26, 31-35]. Nevertheless, a model experimental depletion-driven system that allows for direct force measurements has not been reported in the literature due to the challenges in satisfying a number of physical limitations, particularly if force measurements are sought in a system in which rheology and microstructure can also be measured. Characterization of 3D gel microstructure using confocal microscopy requires a close refractive index match between the colloids and the solvent. In addition, systems are commonly density-matched to minimize

sedimentation effects on microstructure and rheology. Most studies incorporate a specific solvent mixture to meet these requirements [36-38]. The low refractive index contrast between the colloids and the solvent in this type of model system prevents the measurement of thermal rupture forces. Here, we present a model colloidal system in which the interparticle forces generated through a short-ranged depletion interaction are directly measured with laser tweezers, concomitant with characterizations of the microstructure and viscoelastic modulus of the gel at a specific solvent composition. The three challenges of imaging quality, sedimentation, and optical trapping strength are balanced by a systematic investigation of a variety of solvent mixtures spanning a large range of refractive index contrast ratios and density differences.

Materials and Methods

Colloidal synthesis and gelation at various solvent compositions

Monodisperse poly(methyl methacrylate) (PMMA) colloids (diameter $2a$ = 1.15 μm ± 3% and 2.7 μm ± 3%; density ρ_p = 1.19 g/mL; refractive index n_p = 1.488) stabilized by a grafted layer of poly(12-hydroxystearic acid) (PHSA) are used in this study [39]. The steric layer stabilizes the colloids in the solvent and has a thickness of 10 – 14 nm [40]. PMMA colloids are dyed with fluorescent Nile Red to allow for direct visualization with confocal microscopy. Gelation is induced in colloids of $2a$ = 1.15 μm by addition of monodisperse polystyrene (molecular weight M_w = 900,000 g/mol, M_w/M_n = 1.10) at a fixed concentration, c = 8.64 mg/mL. The polystyrene is a non-interacting depletant that induces an entropically driven attraction between the colloids. For microstructural and rheological characterization, gels of intermediate volume fraction (ϕ = 0.20) are used. Laser tweezer experiments are performed on a dilute system containing the larger PMMA colloids ($2a$ = 2.7 μm). The viscoelastic moduli of

colloidal gels has been shown by Shah, et al. (2003) to collapse when scaled on the size of the colloids and the range of the attraction, R_g/a. By such approaches, it will be possible to reconcile the different sized colloids used for the experiments so as to correlate the force measurements with the bulk rheology.

Mixtures of cyclohexane (CH) and cyclohexyl bromide (CHB) at various solvent compositions are chosen for this study. Combining CH with CHB provides a sufficiently large refractive index contrast so that the traps generated by the laser tweezers are strong enough to measure rupture forces. (The most common solvents used to achieve buoyancy-matching in studies of colloidal suspensions, CHB and decalin, do not provide sufficient refractive index contrast for optical trapping.) These mixtures result in a density difference between the colloids and the solvent, but we show that there are conditions where the sedimentation does not significantly affect the microstructural characterization or rheology. The solvents are washed with deionized water and filtered through a 0.2 μm polytetrafluoroethylene syringe filter prior to use. Table I shows the full range of solvent mixtures used in this study along with their physical properties, where w_{CH} and w_{CHB} are the mass fractions of CH and CHB in the solvents, respectively. The Péclet number, defined as $Pe = 4\pi\Delta\rho g a^4/(3kT)$, characterizes the ratio of single-colloid sedimentation to that of Brownian diffusion in the rheological and microstructural characterization experiments. Here $\Delta\rho = \rho_S - \rho_P$, ρ_s is the measured density of the mixed solvent (Anton Paar DMA 4500 M), ρ_P is the density of the colloid, k is the Boltzmann constant, and $2a$ = 1.15 μm, the size of the colloids used for microstructural and rheological characterization. For the proposed system of CH and CHB, increasing the concentration of CH results in a large density mismatch, which also corresponds to a large refractive index contrast, $n_{ct} = n_p/n_s$, where n_s is the refractive index of the mixed solvent. A differential refractometer

(C. N. Wood Mfg. Co., model RF-600) is used to measure n_s at a wavelength of 546 nm and 20°C.

Because CHB is a better solvent for polystyrene than CH, increasing the percentage of CH in the solvent mixture causes a decrease in the radius of gyration, R_g, of the polystyrene depletant. The change in R_g as a function of solvent quality consequently determines the depletion interaction due to its effect on c^*, the overlap concentration of the polystyrene which dictates the strength of the potential. Here, $c^* = 3M_w/\left(4\pi R_g^3 N_A\right)$, where N_A is Avogadro's number. The values of R_g and the second virial coefficient representing solvent quality, A_2, are measured using a multi-angle laser light scattering device (DAWN EOS, GaAs laser at 690 nm, Wyatt Technology) [41]. The light scattered by the polystyrene at five different concentrations is analyzed with Zimm's theory. Mixed solvent effects are negligible in the range of solvents tested [42].

Optical trapping experiments[§]

A 4W CW Nd:YVO_4 near-infrared (NIR, λ = 1064 nm) laser (Compass 1064-4000M) is used as part of a custom-built laser tweezer set up. Briefly, two orthogonal acousto optic deflectors (AOD) are used to steer the laser position in the sample, and back-focal plane (BFP) interferometry is used to detect the displacement of the colloids from the center of the trap based on the interference pattern of the scattered and unscattered light that pass out of the sample. By collimating the laser light after it passes through the sample and directing it onto a quadrant photodiode (QPD), we measure the lateral displacement of the colloids from the traps in the x and y directions as shown by [43].

[§] All optical tweezer measurements and characterization are done by Kathryn A. Whitaker.

To study the effect of index of refraction contrast on QPD sensitivity and trapping strength, dilute suspensions of PMMA colloids in mixtures of CH and CHB are sealed in custom microscopy chambers made using a slide and coverslip spacers (No. 1.5) and sealed using a UV curable adhesive (Norland Optical Adhesive 81). A single colloid is trapped and positioned ~35-40 μm into the sample and the trap is calibrated using a drag calibration technique [44]. The microscope stage is moved at a constant velocity to impose a drag force on the colloid. For a Newtonian solvent, the drag force is $F_{drag} = 6\pi\eta a v$, where η is the solvent viscosity and v is the solvent velocity around the colloid. By varying v and measuring the displacement with the QPD, we determine the relationship between applied force and colloid displacement. In addition to the relationship between force and displacement, the QPD detector also has a response for large displacements. In order to measure the large displacements in the drag calibration, a QPD response curve is needed for each solvent composition. To generate the QPD response curves, the QPD signal is recorded for discrete displacements by moving the trap known distances using the AOD.

Thermal rupture forces are measured using two time-shared optical traps with a laser power of 215 mW measured at the back aperture to the objective. A pair of PMMA colloids are trapped in a mixture of CH and CHB (w_{CH} = 0.37) with c = 8.64 mg/mL. One colloid is held in a stationary trap while a second particle is brought into contact with the first by controlling the motion of the second trap. A triangle wave signal is used to control the motion of the second colloid to ensure that the trap moves at a constant velocity at all points during the experiment. The displacement of the particle from the static trap upon the approach and retraction of the moving colloid is averaged over 120 cycles and used to calculate the cumulative probability distribution of rupture forces by using trajectory averaging as described by Swan et al [26]. The

colloids are imaged with a CCD camera (Hitachi, KP-M1AN, 30 fps) using brightfield microscopy. The brightness intensity of the images is normalized to a reference image for comparison.

Microstructural characterization of gels

An inverted confocal microscope (Nikon A1Rsi) equipped with a resonant scanner head and a high-speed piezo stage is used to capture the 3D structure of the gels. Gels are loaded into custom-built glass capillaries with 300 μm spacers to match the gap used in the rheometer. The top and bottom of the capillaries are sealed using glass coverslips suitable for microscopy (0.17 mm thickness). The gels are set quiescently for 30 minutes before imaging. 3D image stacks are taken from the bottom coverslip at a speed of 15 slices per second. Image processing is performed on stacks with dimensions 42 μm × 42 μm × 10 μm, but only for $w_{CH} \leq 0.37$ due to the significant decrease in refractive index contrast beyond $w_{CH} > 0.37$. The images captured for visualization of refractive index mismatch are taken at 42 μm × 42 μm × 30 μm. The voxel dimensions are 83 nm × 83 nm × 83 nm in both cases. After the initial image volume is captured, the sample is quickly flipped upside down and another stack of the same dimension is obtained from the top coverslip to visually assess the role of sedimentation on gel structure. Image processing is performed using an algorithm that uses a Gaussian mask to filter out digital noise and that identifies centroids based on their intensity maxima [45]. The static error in the colloid location is ± 20 nm in the *x*-*y* plane and ± 31 nm in the *x*-*z* plane as determined by Dibble et al [37]. Colloids are considered to be nearest neighbors if they are closer than the distance that defines the first minimum in the radial distribution function, $g(r)$.

Rheological characterization of gels

Oscillatory rheometry is performed on a stress-controlled rheometer (AR-G2, TA Instruments) at T = 25°C. Colloidal gels are loaded onto a Peltier plate and a stainless steel parallel plate geometry (d = 6 cm, gap h = 300 μm) is lowered to the gap distance while rotating at ω = 1 rad/s to minimize the formation of bubbles at the sample interface. A parallel plate geometry is chosen to minimize confinement effects and a correction factor for the nonhomogeneous strain rate is implemented [46]. We analyze the strain-dependent linear elastic modulus for poly(ethylene oxide) standards ($M_w = 2\times10^6$ g/mol, 4 wt%) at h = 50, 100, 150, 200, 300, 400, and 500 μm, and for gel samples at h = 300 and 500 μm. The results show the absence of gap size effects at h > 150 μm for this geometry. To reduce evaporation of the volatile solvent, a solvent trap is used. The absence of slip is verified by comparing results of a smooth fixture and a fixture with a sand-blasted surface (parallel plate geometry d = 6 cm) [47]. The measured viscoelastic modulus are similar in both cases to within experimental error. After sample loading, gels are pre-sheared unidirectionally for 1 minute (strain = 37,700, shear rate = 628.3 s^{-1}). Oscillatory strain sweep (fixed angular frequency, ω = 10 rad/s) and frequency sweep measurements (fixed strain amplitude, γ = 0.01) are performed after a waiting time of 30 minutes. This fixed waiting time is chosen to allow direct comparison between the gel microstructure and the rheological measurements on the gels.

Results and Discussion

Study Design and Solvent Composition Parameter Space

A successful model material should provide a compromise among the needs for refractive index contrast (for optical trapping), for refractive index matching (for microstructural characterization by confocal microscopy), and for density matching (for mechanical rheometry). The experimental requirements place major constraints on the model system: the refractive index contrast $n_{ct} = n_p / n_s$ must be greater than 1 for trapping, but should also be kept as low as possible to maintain resolution during 3D confocal imaging and to reduce the $\Delta\rho$ which introduces sedimentation effects into the rheology data.

Because the n_{ct} required by optical trapping greatly increases the scattering of PMMA colloids deep within the specimen, images captured with confocal microscopy are limited to a depth of field of 30 μm in the w_{CH} range in which trapping is possible. This depth of field is achieved up to the largest n_{ct} at which confocal microscopy is performed (w_{CH} = 0.64, n_{ct} = 1.045). At $n_{ct} \sim 1$ (w_{CH} = 0.10), the depth of field is limited only by the working distance of the objective (110 μm). The n_{ct} requirement also means that a perfectly density matched system that is optimal for rheometry measurements (w_{CH} = 0.16, $n_{ct} \sim 1$, $\Delta\rho/\rho_p \sim -0.002$) will not be compatible with optical trapping. To address these challenges and balance the conflicting constraints imposed on solvent composition for the three sets of measurements, the solvent composition is systematically varied, as per the systems reported in Table 4.1, to search for a balance of physical properties in which bulk rheology, confocal microscopy, and laser tweezer measurements can all be performed on the same specimen.

Athermal limit of the interparticle potential

The derivative of the interparticle potential, $U(r)$, determines the maximum athermal rupture force, $f_{\max}(r) = -dU(r)/dr$. The analytical form of $U(r)$ is obtained from the

superposition of the Derjaguin-Landau-Verwey-Overbeek (DLVO) and Asakura-Oosawa (AO) theories [27] for our model system. The electrostatic contributions are calculated using a Debye length of 1.3 μm (solvent conductivity for w_{CH} = 0.37 mixture is 1.06 × 10^{-8} S/m) and a constraint on the zeta potential of the solvent mixtures to be ≤ 10 mV [48]. The contact potential takes into consideration that the PHSA comb steric stabilizer is ~10 nm [40]. We assume the stabilizer does not penetrate and use the slope of $U(r)$ evaluated at $r = 2a + 20$ nm to calculate f_{max}. At a constant polymer concentration (c = 8.64 mg/mL), f_{max} decreases with CH content because R_g and consequently c/c^* decrease with a drop in solvent quality. Static light scattering measurements show that the second virial coefficient (a measure of polymer-solvent quality), A_2, decreases from 2.4 × 10^{-6} to 1.5 × 10^{-6} mL.mol/g^2 as CH concentration is increased from w_{CH} = 0.16 to 0.84 [Fig. 4.1(a)], while the measured R_g decreases from 37 nm to 25 nm [Fig. 4.1(b)]. Least-squares regression is used to fit the change in R_g (in nm) as a function of w_{CH} with the form of $R_g = (-16 \pm 4)w_{CH} + (38 \pm 2)$. This fit is used to compute the contribution of the depletion potential to f_{max}, the athermal force limit, which will be compared to the thermal rupture forces obtained from optical trapping.

Microstructural characterization of gels

The cluster-like structures of gels produced in the CH-CHB solvent system are similar to those that have been reported for other systems with weak aggregation due to short-ranged attraction [37]. Figs. 4.2(a)-(c) show the representative images of quiescent gels in the x-y plane, parallel to a bounding surface, where Fig. 4.2(a) corresponds to w_{CH} = 0.16 (Pe = -0.002), (b) corresponds to w_{CH} = 0.37 (Pe = 0.132), and (c) corresponds to w_{CH} = 0.64 (Pe = 0.301). These images are captured at z = 10 μm above the bottom of the sample to ameliorate potential wall

effects on gel microstructure. When $w_{CH} \geq 0.37$, the effects of sedimentation on gel structure are readily observed from *x*-*z* images. Fig. 4.2(d)-(f) show representative images of the gels in the *x*-*z* plane (the *z* dimension origin is defined as the bottom; $z = 300$ μm is the top coverslip). For example, compaction of the bottom layer from sedimentation is significant at $w_{CH} = 0.64$ [Fig. 4.2(f)]. This compaction is quantified by measurement of the near-wall volume fraction, ϕ_{wall}, which is defined as the number of colloids found in a thin region centered at $z = 10$ μm, divided by the volume of that region given by the length and width of the image and a thickness equal to the colloid diameter (42 μm × 42 μm × 1.15 μm). For comparison, the homogeneous (as prepared) volume fraction of these specimens is $\phi_{gel} = 0.20$, and this value would be expected for the sedimentation-free condition [49]. Fig. 4.2(g) shows the change in ϕ_{wall} as a function of the amount of CH in the mixture, where an increasing amount of CH results in a larger $\Delta\rho/\rho$ and *Pe*. Experimental error of ϕ_{wall} from instrument limitations and image processing are ~ 10% of the mean value. Thus, we consider values of $\phi_{wall} \geq 0.22$ to be cases where a significant amount of compaction has arisen due to sedimentation. At $w_{CH} = 0.37$ ($Pe = 0.132$), the value of ϕ_{wall} increases to 0.234 ± 0.006 and supports the visual observations of compaction through sedimentation.

This type of compaction is reminiscent of delayed sedimentation in weakly aggregated gels with short-ranged attractions [50] but in our case we observe a sudden, rapid settling at a fixed waiting time at $w_{CH} \geq 0.37$ as opposed to a critical sedimentation time scale. It is interesting to note that the Péclet number in our case is quite high, but a stable gel structure is maintained at a fixed waiting time of 30 minutes with minimal sedimentation effects on the microstructure. For example, recent literature for thermoreversible adhesive hard spheres report a critical gravitational Péclet number, Pe_g, of 0.01 or less for stable gels [51]. This Péclet number also

compares sedimentation to Brownian diffusion with added effect of percolation in gel networks. (We do not work with fractal gels in our system.) Regardless, when we substitute system-specific variables and assume a DLCA limit for fractal gels ($d_f \sim 1.8$) [52], we find that the Pe_g of the system at $w_{CH} = 0.37$ is ~ 4, which is far greater than the critical criterion for stability. This suggests that delayed sedimentation is likely to occur in our system, but not at the time scale of the experiment for samples at $w_{CH} \leq 0.37$.

Linear and nonlinear rheology of gels

Colloidal gels produced in solvents of different w_{CH} display variable rheology that depends on a number of factors: (i) sedimentation propensity due to differences in the degree of density matching; (ii) van der Waals attraction due to differences in the dielectric spectra of CH and CHB; (iii) depletion attraction due to solvent-quality induced change in the radius of gyration of polystyrene. Specifically, as a result of the decrease in n_{ct} when w_{CH} decreases, the van der Waals attraction between colloids decreases. However, the van der Waals interaction at contact is negligible ($< 10^{-4}$ pN at all rheological experimental conditions) compared to the change in the depletion attraction caused by the increase in R_g (~10^0 pN). Gravitational sedimentation is an additional factor that complicates the understanding of the rheological phenomenon. Here, we use information gained from confocal microscopy to delineate the region in which sedimentation is the dominant factor contributing to the rheological phenomena.

The linear viscoelasticity of the gels is reported as a function of frequency [Fig. 4.3] for different w_{CH}. The slopes of the frequency-dependent elastic and viscous moduli, G'(ω) and G"(ω), are characteristic of the solid-like properties of the gels. For viscoelastic samples, a large slope corresponds to liquid-like behavior. At the gel point, the samples become sufficiently

solid-like such that G'(ω) and G"(ω) should only be weakly dependent on ω [53]. The frequency sweep data shows that gels become weaker in strength as w_{CH} increases, consistent with the decrease in both c/c* and R_g, which affect the strength of the depletion attraction (see Table 4.1).

In Fig. 4.3, sedimentation effects do contribute to the decrease in the frequency-dependent moduli, but these effects cannot be easily distinguished from those due to the solvent-quality induced change in attraction strength. The strain-dependent viscoelasticity of the gels provides a much clearer picture [Fig. 4.4] of the role of sedimentation. A gradual decrease in the plateau value, G', is observed from w_{CH} = 0.16 to 0.37 [Fig. 4.5(a), from (1) to (4)]. For w_{CH} > 0.37 [Fig. 4.5(a), from (4) to (5)], G' decreases much more rapidly. Although the change in G' appears non-monotonic at w_{CH} = 0.47, a similarly sharp and monotonic decrease is seen in the frequency-dependent modulus. This sharp decline in the elastic modulus can likely be attributed to gel detachment from the rheometer geometry, consistent with observations of compaction [Fig. 4.5(b-k)]. This correspondence suggests that at conditions of large density mismatch (Pe > 0.132), the gel strength is insufficient to maintain sample integrity, and the collapse of the gel results in a fluid layer at the top of the sample and compaction of colloids at the bottom [Figs. 4.5(j) and (k)]. This fluid region acts as a slip layer in the rheometer that reduces the elastic modulus in a manner that is far more significant than the decrease in gel strength due to the decrease in depletion attraction. It is important to note that the effect of sedimentation on the rheological measurements is only observed at a fixed waiting time of 30 minutes when w_{CH} > 0.37. The sedimentation is due to the density mismatch and the decrease in gel strength as a function of w_{CH}. Furthermore, for $w_{CH} \leq 0.37$, measurements with a sandblasted fixture having roughness much greater than that of the particle size indicated that no slip is observed for gels produced at this t_w [54, 55]. We therefore conclude that of the three potential contributions to the

variability in G' with w_{CH}, the effect of density mismatch is the most significant when w_{CH} > 0.37. The sedimentation effects limit measurements of rheology in this system to $w_{CH} \leq 0.37$. These findings are for the particular case of depletant concentration c = 8.64 mg/mL studied here.

Characterization of the selected model system

Although maximizing the refractive index contrast n_{ct} enhances trapping strength and therefore allows characterization of thermally induced rupture, the resultant refractive index and density mismatch complicates confocal microscopy and rheology experiments. The solvent that is density matched with PMMA (w_{CH} = 0.16), and therefore optimal for confocal microscopy and rheology, has very low index contrast (n_{ct} = 1.007) that reduces the resolution of the force measurements with the laser tweezers to unacceptable levels. We show that the detector sensitivity is significantly reduced at $w_{CH} \leq 0.16$ as $n_{ct} \rightarrow 1$ with a decrease in trapping strength. The maximum trapping strength sets the range of w_{CH} where forces can be measured for a selected depletant concentration. For c = 8.64 mg/mL, interparticle forces can be measured at $w_{CH} > 0.30$, whereas compaction from sedimentation occurs at $w_{CH} \geq 0.37$, complicating microscopy and rheological measurements. The intersection of these two constraints indicates that w_{CH} = 0.37 is an optimal condition at which there is sufficient optical trapping strength and detector sensitivity for two-particle force measurements with minimal deleterious effects on microstructural characterization and rheological measurement.

A complete characterization of rupture force, gel microstructure, and linear viscoelasticity using this new gel system involving CH and CHB is therefore possible at w_{CH} = 0.37 and c = 8.64 mg/mL (Fig. 4.6). This particular gel (ϕ = 0.20, c/c* = 0.81) has a cluster-like

structure that is typical of weak depletion gels [Fig. 4.6(a)] [Dibble et al. (2006)], as seen in a broad contact number distribution, $p(z)$, with a mean contact number, $\langle z \rangle$, of 5.39 ± 0.06 [Fig. 4.6(b)]. A sensitivity test performed by varying the cutoff for determining nearest neighbors by ± 3% of the particle diameter (slightly greater than the static error associated with the particle location) determined that the contact number distribution at w_{CH} = 0.37 varies by ± 6%. The solvent of the gel has a refractive index contrast of n_{ct} = 1.029, which is sufficiently high for measuring interparticle forces. The cumulative probability distribution of a pair of colloids being bonded as a function of applied force is shown in Fig. 4.6(c). At low applied forces, there is a high probability that the colloids will still be bonded, but the distribution decays for higher applied forces. For a normal distribution, the force at which 50% of the bonds have broken, f_{50}, corresponds to the peak in the probability density function and is the most frequently measured rupture force. The f_{50} value calculated from the rupture force distribution for this gel is 3.3 ± 0.5 pN. The forces where 5% and 95% of the bonds are still bonded set a range of forces describing the width of the distribution. The high end of that distribution is f_{05} = 4.8 ± 0.9 pN, which is approximately equal to the calculated athermal rupture force (f_{max} = 4.6 ± 0.4 pN), demonstrating that we have the ability to measure the maximum possible pair bonding force expected in this gel. The good agreement with f_{max} suggests that the DLVO-AO potential is an acceptable model for describing the pair interactions in a dilute sample. Because the colloid sizes for resolvable trapping force measurements and for rheological characterization are different, the viscoelasticity measurements would need to be scaled with colloid size [55, 56] for comparison with the thermal force measurements.

The linear and nonlinear rheological properties of the gel are shown in Figs. 4.6(d)-(f). Fig. 4.6(d) shows the frequency-dependent elastic and viscous moduli, G'(ω) and G"(ω). The

moduli are weakly dependent on ω, which is typical for gels with arrested dynamics. Fig. 4.6(d) shows that G'(γ) and G"(γ) cross over at the rheological yield strain, $\gamma_c = 0.016$. The yield strain indicates a critical point after which further deformation results in a significant fluidization of the sample. The yield stress, defined by $\tau_y = \gamma G'$ [6, 57], shows a first peak at the onset of nonlinear elastic response [Fig. 4.6(f)], which is typically seen for colloidal gels undergoing bond breaking [6]. For this particular gel, the value of τ_y is 0.04 ± 0.01 Pa. We do not observe two yield strains in this model system. This finding is likely due to the low volume fraction of our samples relative to the range needed for cage yielding [6] as well as the lack of intracluster bond breakage, as seen in gels that are more dilute than the ones studied here [38].

Summary

We have introduced a new model depletion gel in which the interparticle forces, microstructure, and rheology can all be measured. The system uses CH and CHB as the solvent mixture so as to balance the constraints imposed by optical trapping, confocal microscopy, and rheometry. At a weight ratio of $w_{CH} = 0.37$, the refractive index contrast ($n_{ct} = 1.029$) is sufficient to allow measurement of forces as high as 6-7 pN, yet low enough to enable confocal imaging of the microstructure. The density difference between the PMMA and the solvent ($\Delta\rho/\rho_p = 0.102$) is sufficiently small that sedimentation does not significantly impact rheological measurements at short experimental time scales.

This new system serves as a tool for studying the relationship between microscopic properties and the rheology of depletion gels. Current micromechanical models rely on the athermal force limit calculated from theory to predict yielding behavior. Our pair force measurements agree well with the athermal force limit calculated from the DLVO-AO potential

and show that there is a distribution of rupture forces that result in bond breakage. The way to account for the force distribution in order to explain yielding behavior or microstructure rearrangements is not yet available; however, measurements of the kind described here are a precondition to generating such understanding. Although the bond strength is directly related to the yield stress in colloidal gels, the consequences of the coupling between the distribution of interparticle forces and the collective gel structure is less clear for other linear and nonlinear rheological properties. The localization length is too short to be directly measured with optical trapping for use with micromechanical models that predict the elastic modulus. However, the verification of the DLVO-AO potential from the measured force distributions suggests that the localization length calculated from the potential provides a good way to indirectly predict the modulus of the gels. By expanding the results presented here to include gels in a range of depletant concentrations, this model system will enable future exploration of the connection between the microscopic interparticle forces and linear and nonlinear rheology of colloidal gels with short-ranged attractions. A comprehensive study of polymer concentrations will provide information for further discussion about the scaling appropriate for relating the bond strength to the yield stress and moduli of the gels.

Table 4.1. Physical properties of CH and CHB solvent mixtures (reprinted with permission from [L.C. Hsiao, K.A. Whitaker, M.J. Solomon & E.M. Furst, *submitted* (2014)])

w_{CH}	w_{CHB}	ρ_s[†] (g/mL)	$\Delta\rho/\rho_p$ (%)	Pe	n_s[††]	n_{ct}[†††]	R_g (nm)	c/c^*[††††]
0.10	0.90	1.243	-4.6	-0.060	1.501	1.007	–	1.33
0.16	0.84	1.190	-0.2	-0.002	1.493	1.012	37 ± 1	1.18
0.20	0.80	1.162	2.2	0.028	1.489	1.016	39 ± 2	1.09
0.28	0.72	1.105	7.0	0.091	1.480	1.021	33 ± 2	0.94
0.37	0.63	1.067	10.2	0.132	1.469	1.029	26 ± 3	0.81
0.47	0.53	1.049	11.7	0.152	1.461	1.035	31 ± 2	0.69
0.58	0.42	0.941	20.8	0.270	1.451	1.041	28 ± 2	0.58
0.64	0.36	0.912	23.2	0.301	1.447	1.045	32 ± 2	0.53
0.70	0.30	0.884	25.6	0.332	1.442	1.048	27 ± 2	0.48
0.84	0.16	0.829	30.2	0.392	1.434	1.054	25 ± 2	0.40

[†] measurements at 25°C
[††] measurements at 546 nm, 20°C
[†††] shifted to 1046 nm, 20°C
[††††] calculated from linear regression of R_g as a function of w_{CH}

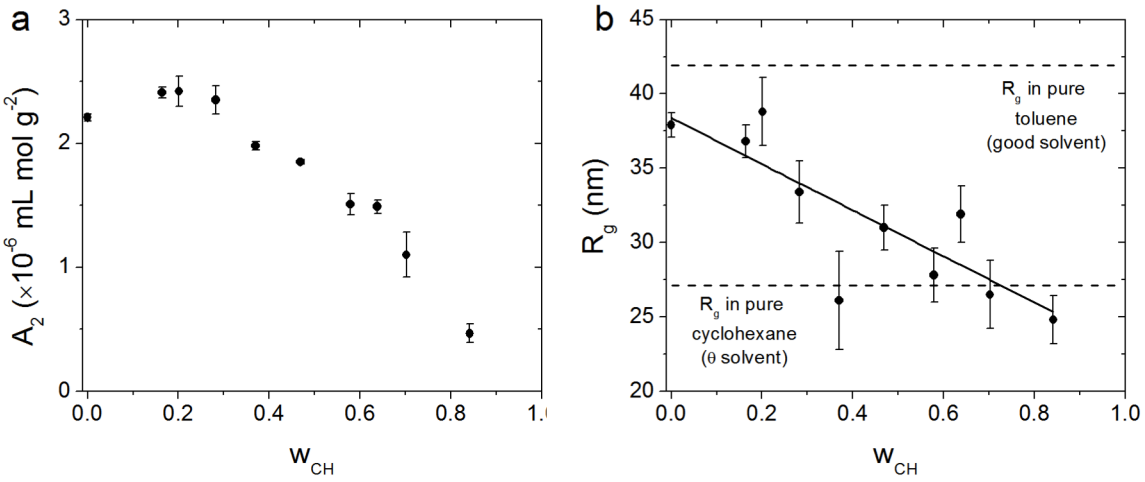

Figure 4.1. Static light scattering of polystyrene in CH/CHB mixtures. (a) Changes in solvent quality, and (b) R_g of 900,000 g/mol polystyrene in the solvents used in this study. In (b), the solid line is a least-squares fit of the change in R_g as a function of w_{CH}. Literature values of R_g in a good solvent (pure toluene) and a theta-solvent (pure CH) are provided for reference [58]. This Figure is reprinted with permission from [L.C. Hsiao, K.A. Whitaker, M.J. Solomon & E.M. Furst, *submitted* (2014)].

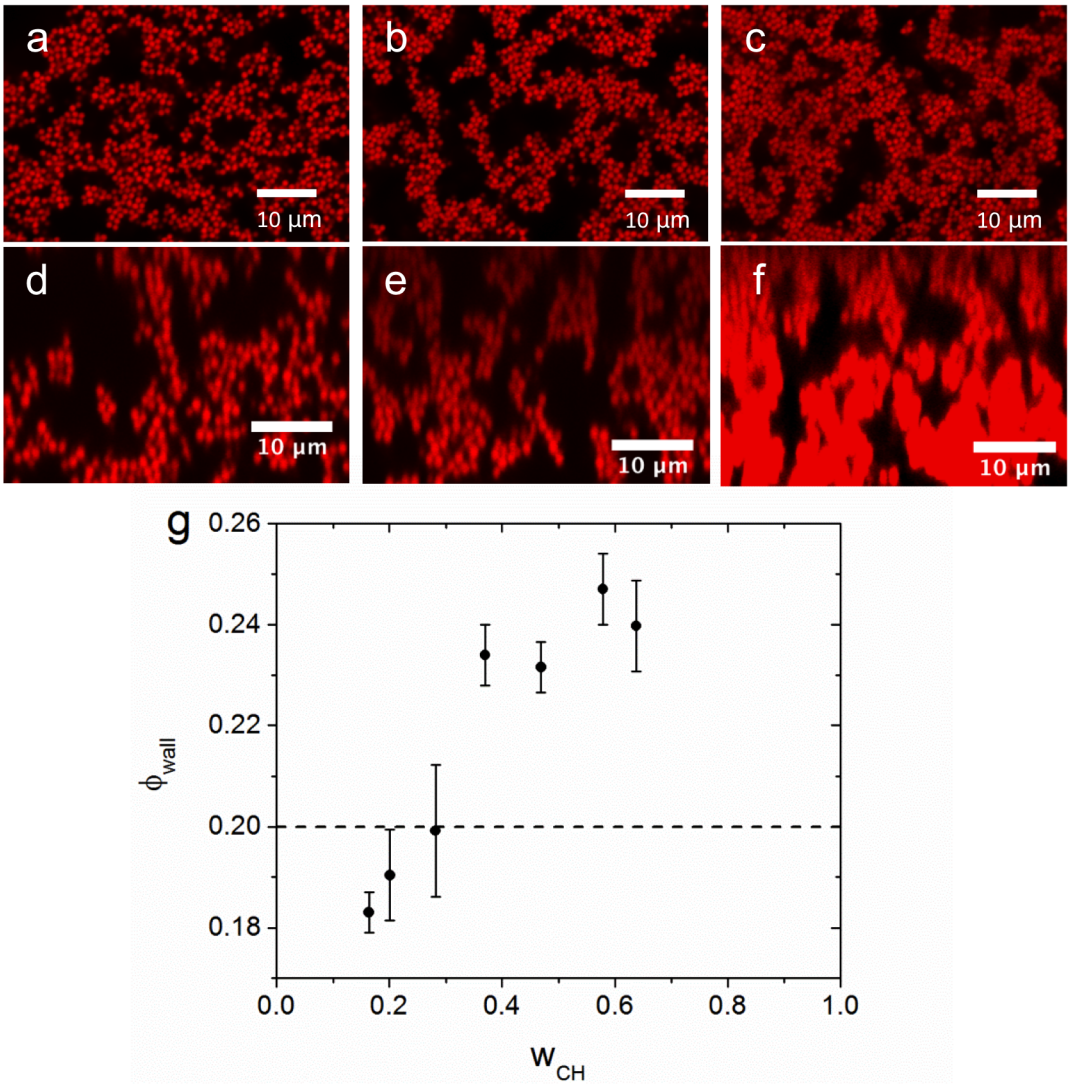

Figure 4.2. Sedimentation of gels (φ = 0.20) at different solvent compositions. (a-c), Representative 2D *x*-*y* plane CLSM images of gels with w_{CH} = 0.16, 0.37, and 0.64; images are taken at *z* = 10 μm; (d-f), representative 2D *x*-*z* plane (*z* = 0-30 μm, *z* = 0 μm is at the bottom of the images) CLSM images of gels at the same solvent compositions; (g), φ_{wall} as a function of w_{CH} estimated from the number of particles in the *x*-*y* plane at *z* = 10 μm. Error bars shown are standard deviations of the mean. This Figure is reprinted with permission from [L.C. Hsiao, K.A. Whitaker, M.J. Solomon & E.M. Furst, *submitted* (2014)].

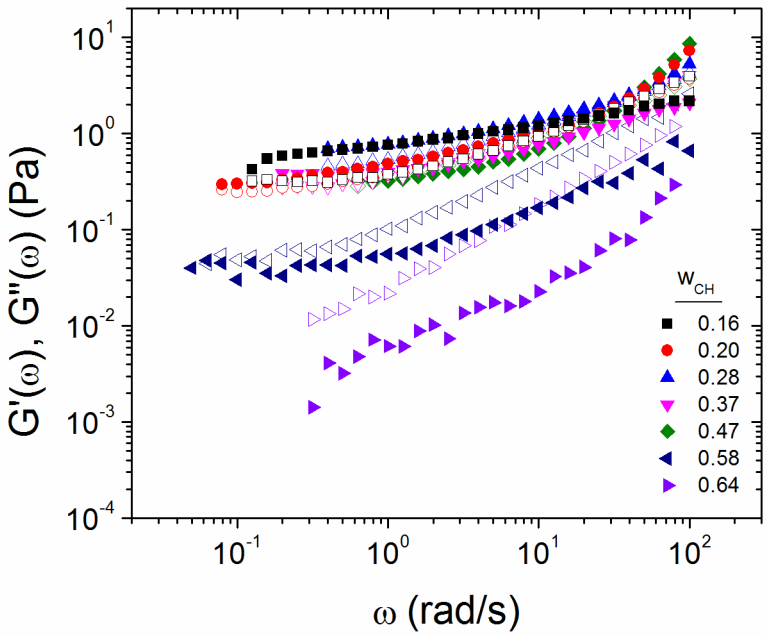

Figure 4.3. Linear oscillatory frequency sweep dataset for gels with w_{CH} = 0.16, 0.20, 0.28, 0.37, 0.47, 0.58, and 0.64. Closed symbols represent G' and open symbols represent G". This Figure is reprinted with permission from [L.C. Hsiao, K.A. Whitaker, M.J. Solomon & E.M. Furst, *submitted* (2014)].

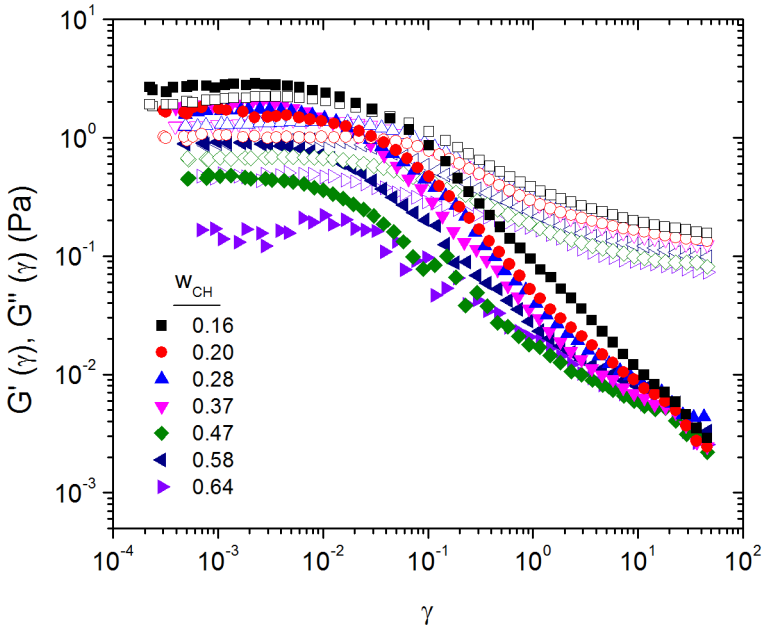

Figure 4.4. Linear oscillatory strain sweep dataset for gels with w_{CH} = 0.16, 0.20, 0.28, 0.37, 0.47, 0.58, and 0.64. Closed symbols represent G' and open symbols represent G". This Figure is reprinted with permission from [L.C. Hsiao, K.A. Whitaker, M.J. Solomon & E.M. Furst, *submitted* (2014)].

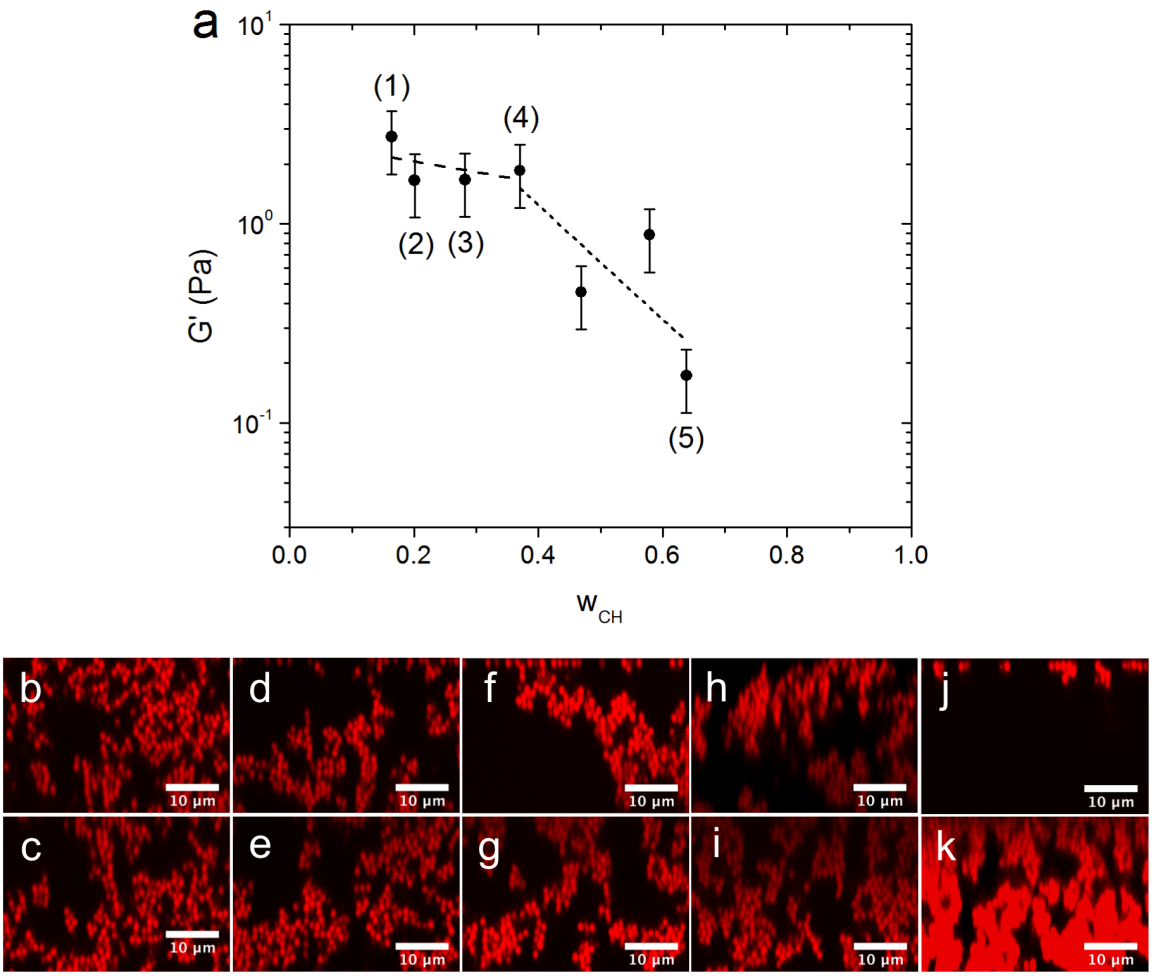

Figure 4.5. Visualization of sedimentation and effect on linear rheology. (a) Linear strain-dependent G' as a function of w_{CH}. Dashed and dotted lines separate the two different regimes. Error bars shown are standard errors of the mean from seven independent measurements of one sample at w_{CH} = 0.64. Representative 2D x-z confocal images of gels at (b,c), w_{CH} = 0.16, (d,e), w_{CH} = 0.20, (f,g), w_{CH} = 0.28, (h,i), w_{CH} = 0.37, and (j,k) w_{CH} = 0.64. (b-j) show the z = 270 to 300 μm and (c-k) show z = 0 to 30 μm for the gels. In (a), (1) refers to the measured rheology at a gelation condition corresponding to (b,c), (2) = (d,e), (3) = (f,g), (4) = (h,i), and (5) = (j,k). This Figure is reprinted with permission from [L.C. Hsiao, K.A. Whitaker, M.J. Solomon & E.M. Furst, *submitted* (2014)].

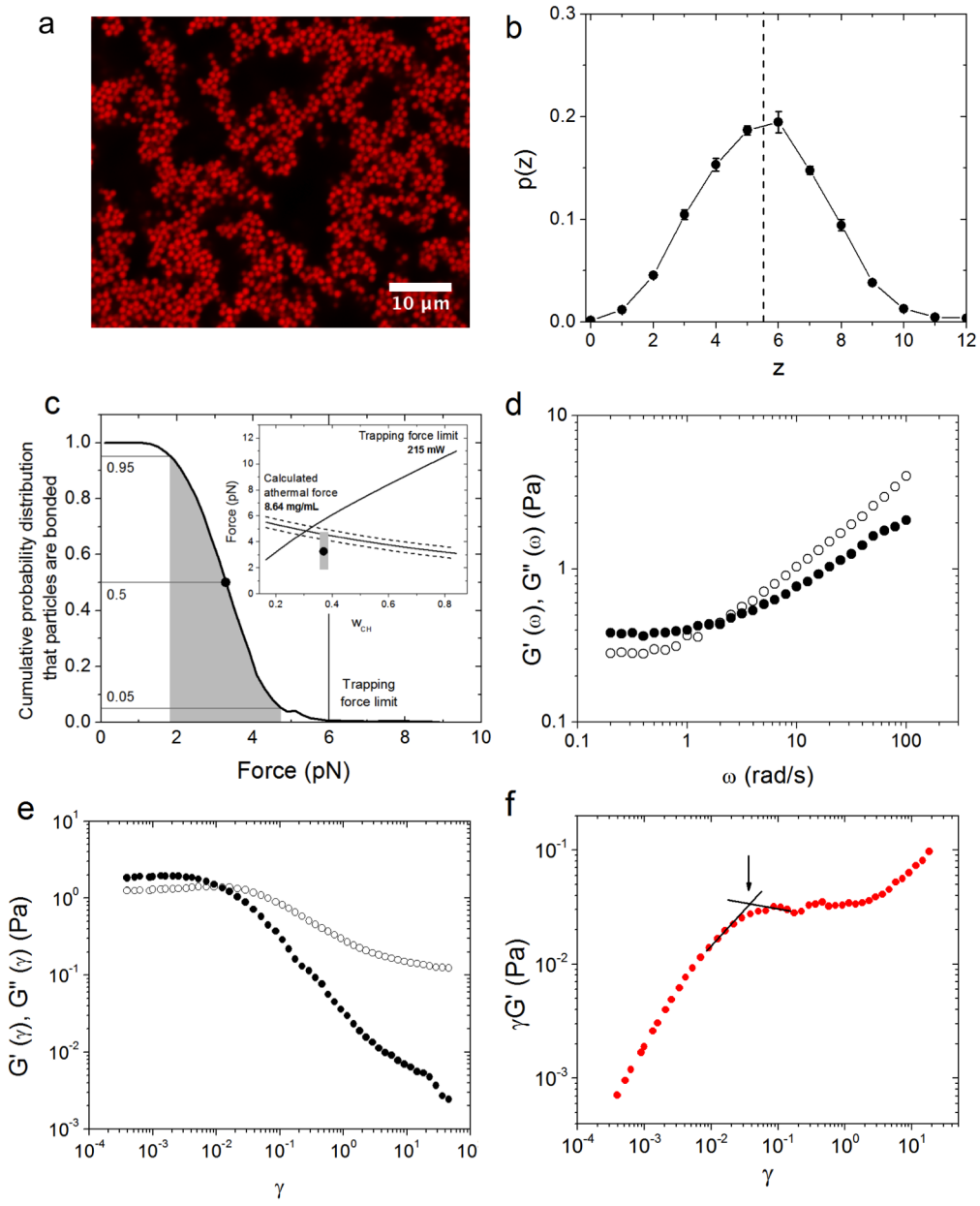

Figure 4.6. Characterization of a model colloidal gel (w_{CH} = 0.37, c = 8.64 mg/ml). (a) 2D x-y image of the gel at z = 10 µm; (b) 3D contact number distribution $p(z)$, where the dotted line is the mean contact number, ‹z›; (c) Cumulative probability distribution of rupture forces between PMMA particles calculated from 120 rupture cycles. The highlighted forces mark the range in which 5% and 95 % of bonds are bonded. The inset shows where the force distribution fits on the trapping operating regime. The dashed lines mark the 95% confidence intervals around the athermal limit due to uncertainty in R_g. (d) Frequency-dependent viscoelasticity and (e) strain - dependent viscoelasticity. Closed symbols represent G'(ω) and G'(γ) and open symbols represent G"(ω) and G"(γ). (f) Elastic yield stress of gel with the arrow indicating the first yield stress, τ_y. The particle size used in (a), (b), and (d-f) is 2a = 1.15µm and in (c) 2a = 2.7 µm. This Figure is reprinted with permission from [L.C. Hsiao, K.A. Whitaker, M.J. Solomon & E.M. Furst, *submitted* (2014)].

References

[1] J. Sun, X. Zhao, W. R. K. Illeperuma, O. Chaudhuri, K. H. Oh, D. J. Mooney, J. J. Vlassak, and Z. Suo, *Nature* **489**, 133 (2012).
[2] M. E. Helgeson, S. E. Moran, H. Z. An and P. S. Doyle, *Nature Materials* **11**, 344 (2012).
[3] J. Vermant and M. J. Solomon, J*ournal of Physics: Condensed Matter* **17**, R187 (2005).
[4] E. Zaccarelli, *Journal of Physics: Condensed Matter* **19**, 323101 (2007).
[5] J. D. Park and K. H. Ahn, *Soft Matter* **9**, 11650 (2013).
[6] N. Koumakis and G. Petekidis, *Soft Matter* **7**, 2456 (2011).
[7] B. Rajaram and A. Mohraz, *Soft Matter* **6**, 2246 (2010).
[8] H. Hoekstra, J. Vermant, J. Mewis, and G. G. Fuller, *Langmuir* **19**, 9134 (2003).
[9] V. Gopalakrishnan and C. F. Zukoski, *Journal of Rheology* **51**, 623 (2007).
[10] G. Yin and M. J. Solomon, *Journal Of Rheology* **52**, 785 (2008).
[11] P. Schall, D. A. Weitz, and F. Spaepen, *Science* **318**, 1895 (2007).
[12] H. Emady, M. Caggioni, and P. Spicer, *Journal of Rheology* **57**, 1761 (2013).
[13] K. Masschaele, J. Fransaer, and J. Vermant, *Soft Matter* **7**, 7717 (2011).
[14] M. H. Lee and E. M. Furst, *Physical Review E* **77**, 41408 (2008).
[15] J. Vermant, P. Van Puyvelde, P. Moldenaers, J. Mewis, and G. G. Fuller, *Langmuir* **14**, 1612 (1998).
[16] P. Varadan and M. J. Solomon, *Journal of Rheology* **47**, 943 (2003).
[17] B. J. Maranzano and N. J. Wagner, *Journal of Rheology* **45**, 1205 (2001).
[18] S. Ramakrishnan, V. Gopalakrishnan, and C. F. Zukoski, *Langmuir* (2005).
[19] N. Krishna Reddy, Z. Zhang, M. Paul Lettinga, J. Dhont, and J. Vermant, *Journal of Rheology* **56**, 1153 (2012).
[20] W. H. Shih, W. Y. Shih, S. I. Kim, J. Liu, and I. A. Aksay, *Physical Review A* **42**, 4772 (1990).
[21] A. H. L. West, J. R. Melrose, and R. C. Ball, *Physical Review E* **49**, 4237 (1994).
[22] A. A. Potanin, *Journal of Colloid and Interface Science* **157**, 399 (1998).
[23] A. R. Studart, E. Amstad, and L. J. Gauckler, *Soft Matter* **7**, 6408 (2011).
[24] A. Hess and N. Aksel, *Langmuir* **29**, 11236 (2013).
[25] E. Evans, *Faraday Discussions* **111**, 1 (1999).
[26] J. Swan, M. Shindel, and E. Furst, *Physical Review Letters* **109**, 198302 (2012).
[27] S. Asakura and F. Oosawa, *Journal of Chemical Physics* **22**, 1255 (1954).
[28] H. A. Kramers, *Physica* **7**, 284 (1940).
[29] S. M. Fielding, P. Sollich, and M. E. Cates, *Journal of Rheology* **44**, 323 (2000).
[30] S. Manley *et al.*, *Physical Review Letters* **93**, 108302 (2004).
[31] J. C. Crocker, J. A. Matteo, A. D. Dinsmore, and A. G. Yodh, *Physical Review Letters* **82**, 4352 (1999).
[32] E. M. Furst and J. P. Pantina, *Physical Review E* **75**, 050402 (2007).
[33] J. P. Pantina and E. M. Furst, *Physical Review Letters* **94**, 138301 (2005).
[34] J. P. Rich, J. Lammerding, G. H. McKinley, and P. S. Doyle, *Soft Matter* **7**, 9933 (2011).
[35] I. Sriram, E. M. Furst, R. J. DePuit, and T. M. Squires, *Journal of Rheology* **53**, 357 (2009).
[36] C. P. Royall, M. E. Leunissen, and A. van Blaaderen, *Journal of Physics: Condensed Matter* **15**, S3581 (2003).
[37] C. J. Dibble, M. Kogan, and M. J. Solomon, *Physical Review E* **74**, 41403 (2006).

[38] H. Chan and A. Mohraz, *Physical Review E* **85**, 41403 (2012).
[39] L. Antl, J. W. Goodwin, R. D. Hill, R. H. Ottewill, S. M. Owens, S. Papworth, and J. A. Waters, *Colloids and Surfaces* **17**, 67 (1986).
[40] A. Campbell and P. Bartlett, *Journal of Colloid and Interface Science* **256**, 325 (2002).
[41] M. Ganesan, E. J. Stewart, J. Szafranski, A. E. Satorius, J. G. Younger, and M. J. Solomon, *Biomacromolecules* **14**, 1474 (2013).
[42] M. J. Solomon and S. Muller, *Journal of Polymer Science: Part B: Polymer Physics* **34**, 1 (2002).
[43] F. Gittes and C. F. Schmidt, *Opt. Lett.* **23**, 7 (1998).
[44] K. C. Neuman and S. M. Block, *Review of Scientific Instruments* **75**, 2787 (2004).
[45] J. C. Crocker and D. G. Grier, *Journal of Colloid and Interface Science* **179**, 298 (1996).
[46] P. R. Soskey and H. H. Winter, *Journal of Rheology* **28**, 625 (1984).
[47] R. Buscall, *Journal of Rheology* **54**, 1177 (2010).
[48] L. C. Hsiao, R. S. Newman, S. C. Glotzer, and M. J. Solomon, *Proceedings of the National Academy of Sciences USA* **109**, 16029 (2012).
[49] J. Guo and J. A. Lewis, *J. Am. Ceram. Soc.* **83**, 266 (2000).
[50] H. Sedgwick, S. U. Egelhaaf, and W. C. K. Poon, *Journal of Physics: Condensed Matter* **16**, S4913 (2004).
[51] J. M. Kim, J. Fang, A. P. R. Eberle, and N. J. Wagner, *Physical Review Letters* **110**, 208302 (2013).
[52] C. Allain, M. Cloitre, and M. Wafra, *Physical Review Letters* **74**, 1478 (1995).
[53] F. Chambon and H. H. Winter, *Journal of Rheology* (1987).
[54] P. Ballesta, R. Besseling, L. Isa, G. Petekidis, and W. C. K. Poon, *Physical Review Letters* **101**, 258301 (2008).
[55] P. Ballesta, N. Koumakis, R. Besseling, W. C. K. Poon, and G. Petekidis, *Soft Matter* **9**, 3237 (2013).
[56] S. A. Shah, Y. L. Chen, K. S. Schweizer, and C. F. Zukoski, *Journal of Chemical Physics* **119**, 8747 (2003).
[57] M. C. Yang, L. E. Scriven, and C. W. Macosko, *Journal of Rheology* **30**, 1015 (1986).
[58] L. J. Fetters, N. Hadjichristidis, J. S. Lindner, and J. W. Mays, *J. Phys. Chem* **23**, 619 (1994).

CHAPTER 5

Orientational order and kinetics in the three-dimensional self-assembly of colloidal ellipsoids

Abstract

The axial asymmetry of oblate spheroids promotes bottom-up self-assembly into structures with long-ranged orientational order. We synthesize monodisperse colloidal oblate spheroids by applying a uniaxial thermomechanical compression. Stable spheroids are suspended in a refractive index and density-matched solvent and a long-ranged depletion attraction is induced by the addition of polystyrene. The phase behavior and aggregation kinetics of the three-dimensional self-assembled structures are quantified by measuring the degree of clustering and local orientational order. We observe the formation of orientational aggregates in a narrow range of volume fractions ($0.018 \leq \phi \leq 0.023$). A concurrent study of cluster growth kinetics show that fraction of particles in these oriented clusters grows as a function of time for systems with high attraction strengths ($c/c^* = 4.0$). The text in this chapter is taken from a manuscript in preparation [L.C. Hsiao, B.A. Schultz, S.C. Glotzer & M.J. Solomon, *In preparation* (2014)].

Introduction

Helical structures are commonly encountered in nature, but are difficult to achieve artificially without strong applied fields [1, 2] or pre-fabricated templates [3, 4]. The axial

asymmetry of discotic (oblate) spheroids promotes bottom-up self-assembly into tilted, columnar arrangements for attractions with ranges that are a few factors larger than the particle dimensions [5]. Simulations show that the tilted stack configuration is the most energetically favorable state for oblate spheroids, leading to long-ranged orientational order [6, 7]. Because of this tendency to tilt, the global order parameters are often insensitive to the resultant self-assembled structures.

Experiments to probe features of discotic assembly commonly utilize colloidal clay suspensions consisting of nanometer-sized platelets as model systems, due to the ease of synthesizing bulk quantities of these materials. Nematic ordering, in which platelets show orientational but no positional order, are frequently observed even given the polydispersity of these materials, suggesting that the axial anisotropy leads to strong face-to-face entropic forces [8, 9]. Wax disks tend to arrange in columnar stacks even at dilute concentrations [10]. The interaction anisotropy can also manifest as arrested liquids at exceedingly low particle loading [11], and a house-of-cards stress-bearing structure has been previously observed in shear flow [12]. Despite their scientific and technological importance, clay platelets are challenging model systems due to their polydispersity [13]. In addition, their entropic preference for face-to-face ordering competes with the complex face-to-edge and face-to-face charged interactions [11, 14]. Few experimental methods are known to generate high quality model colloidal oblate spheroids in bulk quantities; existing techniques utilize biaxial stretching [15] and blown films [16].

Here we show that uniaxial compression is a reliable method to generate monodisperse colloidal PMMA oblate spheroids that can be suspended in refractive index and density-matched solvents. The addition of polymer molecules to these suspensions induces a depletion attraction of tunable strength and range. Our motivation to use a long-ranged attraction comes from the suppression of dynamic arrest when the polymer-colloid ratio exceeds about 0.3 [17]. Intuitively,

a full equilibrium process unhindered by kinetic arrest should promote the formation of long-ranged structures by allowing spheroidal colloids in contact to fully explore energetically favorable configurations through rotation. A systematic variation of the packing fraction and attraction strength shows that aggregates with orientational order only form in a narrow range of volume fractions and with strong attractions. In a concurrent study of aggregation kinetics, we find that the radial distribution function develops a sharp peak at the minor axis of the ellipsoids, indicating the stacking of spheroids in samples with high levels of polymer depletant. In addition, we find that the orientational order within these samples, quantified by the fraction of particles that exist in ordered clusters of a certain length, increases as a function of time. This orientational growth is not observed for samples below a critical value of c/c*.

Materials and Methods

Colloidal synthesis, stability, and self-assembly of PMMA oblate spheroids

Colloidal oblate spheroids are obtained by uniaxial compression of spherical particles. We synthesize the precursor monodisperse poly(methyl methacrylate) (PMMA) spherical colloids (diameter $2a_0$ = 1.49 μm ± 4%) stabilized by a grafted layer of poly(12-hydroxystearic acid) (PHSA) and cross-linked with ethylene glycol dimethacrylate (EGDM) at a 0.5 wt % ratio to the monomer [18]. The steric layer has a thickness of 10 – 14 nm [19]. PMMA colloids are dyed with fluorescent Nile Red to allow for direct visualization with confocal microscopy [19]. The spheres are embedded at a 2.0 wt % concentration in a hydroxy-terminated poly(dimethyl siloxane) (PDMS) (M_n ~ 110,000, viscosity ~ 50,000 cSt) matrix, in which tin (II) ethylhexanoate and poly(dimethylsiloxane-co-methylhydrosiloxane) are added as a catalyst and a cross-linker respectively (Fig. 5.1(a)). The PDMS matrix is heated to a temperature (T = 150°C)

above the glass transition temperature, T_g, of the PMMA. A uniaxial compression is applied at a pressure of 1144 kPa (starting thickness of film = 2.6 mm, final thickness = 0.6 mm, strain = 0.23) using two flat poly(tetrafluoroethylene) (PTFE) plates (Fig. 5.1(b), (c)) to generate oblate spheroids of aspect ratio, $l = b/a = (0.46 \pm 0.09)$, where a is the radius of the major axis and b is the radius of the minor axis. Fig. 5.1(d) shows a representative scanning electron microscopy image of a cluster of monodisperse oblate spheroids in random orientations. The value of a is measured from scanning electron microscopy images of dilute samples, in which spheroids lie flat on the substrate and are far apart from each other. The value of b is obtained from the conservation of volume of the starting sphere (Fig. 5.1(e)), using the relation $ab^2 = a_0^3$ [15]. These values are also independently verified during the image processing of confocal microscopy images. For the spheroids used in this study, $a = (1.07 \pm 0.06)$ μm and $b = (0.48 \pm 0.08)$ μm from scanning electron microscopy images.

The thermomechanically pressed sample is allowed to cool under pressure to room temperature. A degrading solution consisting of 0.75 wt % sodium methoxide dissolved in isopropyl alcohol and hexane is used to release the PMMA spheroids from the PDMS matrix. The complete removal of PDMS is critical for self-assembly experiments. Because this degradation process also removes the PHSA graft copolymer from the surface of the spheroids [20], we re-introduce the PHSA steric layer onto the spheroids through a 72-hour covalent bonding reaction catalyzed by 0.24 vol % dimethylaminoethanol at $T = 80°C$. The reaction is performed at $T < T_g$ to avoid any change to the shape of the spheroids. The restabilized particles are cleaned by multiple washings with pure hexane and passed through a 11.0 μm nylon filter to remove residue. Spheroids are suspended via solvent transfer in a refractive-index and density-matched solvent at a volume fraction varying from $\phi = 0.003$ to 0.036. The solvent is washed

with deionized water and filtered prior to use, and consists of 81 vol % cyclohexylbromide (CHB) and 19 vol % decalin with 1 vol % PHSA and 3 μM tetrabutylammonium chloride (TBAC) to provide charge screening. From conductivity measurements, the Debye length is κ^{-1} = 151 nm and the zeta potential is estimated to be $\zeta \leq 10$ mV [21]. The solvent viscosity (η = 2.5 × 10^{-3} Pa·s) is measured with a cone-and-plate geometry on a controlled stress rheometer (TA Instruments, AR-G2).

Single-particle dynamics from particle tracking suggest that the PMMA spheroids are stable in this solvent for approximately 4 days (Fig. 5.1(f)). Specifically, the 1D mean-squared displacement of the spheroids as a function of the delay time, $\left\langle \Delta x^2(\Delta t) \right\rangle$, show that spheroids exhibit fully diffusive behavior where $\left\langle \Delta x^2(\Delta t) \right\rangle \sim \Delta t$ for measurements conducted at experimental wait times, $t_w \leq 192$ hours (Fig. 5.1(g)). The measured orientationally-averaged translational diffusivity of the dilute suspension is D_T = (0.08 ± 0.01) μm^2/s. This value agrees with the theoretical prediction of the orientationally-averaged diffusivity calculated from parallel and perpendicular components of the Stokes-Einstein diffusivity, $D_{T,\parallel} = k_B T / \eta \hat{K}_{s,\parallel}$ and $D_{T,\perp} = k_B T / \eta \hat{K}_{s,\perp}$, to a relative error of ~15%. $\hat{K}_{s,\parallel}$ and $\hat{K}_{s,\perp}$ are material constants that depend on the geometry of the oblate spheroids [22]. Here, $D_{T,\parallel} = 0.10 \mu \text{m}^2/\text{s}$ and $D_{T,\perp} = 0.11 \mu \text{m}^2/\text{s}$ (the orientationally averaged value is plotted as a dashed line in Fig. 5.1(g)). The self-part of the 1D time-dependent van Hove correlation function characterizes the probability distribution of single-particle displacements. Fig. 5.1(h) shows that the spheroids exhibit a Gaussian distribution in the van Hove correlation that is characteristic of a fluid suspension for $t_w \leq 192$ hours [23]. Non-Gaussian dynamics and aggregation begin to set in thereafter, and is seen as a sharp peak in Fig. 5.1(h) (open purple circles).

Self-assembly of the spheroids is induced by addition of a polystyrene standard (molecular weight M_w = 2.1 × 10^7 g/mol, radius of gyration R_g = 194 nm determined through static light scattering) at various concentration (c/c^* = 1.1, 1.6, 2.1, 2.7, 3.2, 4.0, and 5.3, where c^* is the overlap concentration of the polystyrene) to the suspension. The value of c^* = 1.12 mg/ml for the solvent mixture used in this study is determined using the relation $c^* = 3M_w/4\pi R_g N_A$ [24]. The polystyrene molecule acts as a depleting agent and generates a long-ranged anisotropic attraction (polymer-colloid size ratio, $\xi_a = R_g/a$ = 0.40, $\xi_b = R_g/b$ = 0.18) that favors the formation of fluid-fluid equilibrium structures [17].

Confocal microscopy imaging

An inverted confocal microscope (Nikon A1Rsi) equipped with a resonant scanner head and a high-speed piezo stage is used to capture the 3D structure of the self-assembled structures. The spheroids are allowed to quiescently equilibrate for a minimum of t_w = 120 min, and images are captured at a distance of $z \geq 10$ μm above the coverslip to avoid wall interactions. The image dimensions are 63.5 × 63.5 × 30.0 μm^3, with voxel dimensions of 124 × 124 × 124 nm^3. The acquisition time for each image volume is ~ 17 s. Three image volumes are obtained from independent locations within the same sample. In addition, we collect 3D image volumes of two select cases (ϕ = 0.018, c/c* = 4.0; ϕ = 0.023, c/c* = 1.7) at regular intervals from t_w = 0 to 150 minutes to study the kinetics of oriented self-assembly. These image volumes are independently captured as a function of time within the same sample.

Image processing and quantification of cluster aggregation and orientational order[**]

From the confocal microscopy image volumes, we compute the positions and orientations of the oblate spheroids with a watershed-cut based algorithm. This method extends the identification of particle centroids based on the local brightness to arbitrary shapes [25, 26]. Briefly, images are segmented based on a threshold intensity value, and the eigenvectors and eigenvalues of a covariance matrix is used to compute the shape and orientation of individual particles [27]. Using the watershed-cut method, we find that the aspect ratio of the oblate spheroids used in the self-assembly studies is $l = 0.50 \pm 0.01$. This value is equivalent to the measurements obtained from scanning electron microscopy, to within experimental error. A photopolymerized sample is used to determine the static error in the particle positions and the orientational angle. The positional uncertainty is ± 30 nm (± 0.24 voxel size); the angular uncertainty is ± 3°.

Particles are considered to be bonded when they are within a separation that is equivalent to the first minimum of the radial surface distribution function, computed using the elliptic contact function [6]. The fraction of particles in these cluster aggregates determines the value of f_{clust}. Local orientation order is quantified using an additional angular criterion: particles in contact are considered to be orientationally aggregated if the difference between their orientational vectors, θ, is $\leq 45°$. This gives us the fraction of particles in oriented clusters, $f_{ordered}$. We examine changes in f_{clust} and $f_{ordered}$ as a function of the cumulative number of particles in clusters containing s particles. The characteristic hydrodynamic radius of the clusters, R_H, is obtained from the mean cluster size. High values of f_{clust} and R_H indicates a large subpopulation of particles that reside within large clusters. Assemblies with high degree of

[**] The 3D image processing suite described here is developed by Benjamin A. Schultz.

orientational ordering are expected to have higher values of $f_{ordered}$ compared to less oriented assemblies, because of the existence of longer thread-like structures within the sample.

Results

Phase behavior of self-assembled oblate spheroids

We perform a systematic study of the effect of c/c* and ϕ on the self-assembly behavior of colloidal oblate spheroids (Fig. 5.3(a)). The clustering and orientational tendencies of the self-assembled structures are visually apparent in the confocal microscopy images as shown in Fig. 5.3 (b-g). For $3.2 \leq c/c^* \leq 4$, an increase in ϕ results in a transition from fluid clusters with local orientational order (Fig. 5.3(b), $\phi = 0.009$, $f_{clust} = 0.44$, $f_{ordered} = 0.04$) to string-like structures with high orientational order (Fig. 5.3(c), $\phi = 0.018$, $f_{clust} = 0.89$, $f_{ordered} = 0.34$), and finally to large clusters with little orientational order at the highest ϕ tested (Fig. 5.3(d), $\phi = 0.035$, $f_{clust} = 0.76$, $f_{ordered} = 0.030$). A similar trend in the aggregation behavior is observed at lower attraction strengths ($1.1 \leq c/c^* \leq 1.6$). At dilute colloids concentrations (Fig. 5.3(e), $\phi = 0.004$, $f_{clust} = 0.02$, $f_{ordered} = 0.00$), spheroids are freely mobile and do not exhibit any clustering or orientational behavior. As ϕ increases, heterogeneous regions with large voids and clusters of low orientational order are seen (Fig. 5.3(f), $\phi = 0.023$, $f_{clust} = 0.95$, $f_{ordered} = 0.08$). This type of structure is reminiscent of cluster-like gels formed with weak, short-ranged attractions [21, 24]. Large clusters with little orientational order are observed at high ϕ (Fig. 5.3(g), $\phi = 0.038$, $f_{clust} = 0.70$, $f_{ordered} = 0.04$). These values of f_{clust} and $f_{ordered}$ are plotted for all samples in Fig. 5.3(h) and (i). Our results suggest that orientational aggregation is the preferred configuration only in a specific range of c/c*, particularly at volume fractions that are sufficiently large to support

stacked structure (Fig. 5.3(h)). Fig. 5.3(i) shows that significant quantities of orientational aggregates with $s \geq 3$ are found only within a narrow region ($0.018 \leq \phi \leq 0.023$ and $c/c^* = 4.0$).

Kinetics of orientational self-assembly

Fig. 5.3(b) and (e) show that samples with similarly large subpopulations of particles in clusters of $s \geq 3$ ($f_{clust} = 0.89$ and 0.95) can show distinctly different degree of orientational order ($f_{ordered} = 0.34$ and 0.08). The difference in clusters of $s \geq 4$ is even more distinct ($f_{ordered} = 0.20$ and 0.02). In order to better understand the relationship between orientational ordering and cluster aggregation, we study the growth kinetics of systems for which a distinct transition from orientational to nonorientational aggregation is observed as c/c^* is reduced. Fig. 5.4(a-f) show the time-dependent evolution of assembled structures for a system a propensity to form sample with local orientation ($\phi = 0.018$, $c/c^* = 4.0$, $f_{clust} = 0.89$, $f_{ordered} = 0.34$). At $t_w = 5$ min (Fig. 5.4(a)), the system is comprised of mostly free, mobile spheroids along with short chains of oriented fluid clusters. Between $t_w = 10$ min (Fig. 5.4(b)) and 30 min (Fig. 5.4(c)), there is an increase in the population of oriented clusters, which connect to form longer structures. These structures continue to combine and grow in a linear manner until orientational order ($f_{ordered} = 0.34$) is reached at $t_w = 120$ min (Fig. 5.4(d-f)). Fig. 5.4(g) shows a close-up of a representative oriented cluster of size $s = 6$ found at $t_w = 120$ min.

In contrast, there is no sustained, long-ranged orientational assembly for a similar system with reduced attraction strength. Fig. 5.4(h-m) show the structural evolution for a system with low orientational order ($\phi = 0.023$, $c/c^* = 1.7$, $f_{clust} = 0.95$, $f_{ordered} = 0.08$). Fig. 5.4(h) shows that the structure initializes in a similar manner to Figure 4(a) at $t_w = 5$ min. At $t_w = 10$ min, Fig. 5.4(i) shows that larger fluid clusters with reduced orientational order compared to Fig. 5.4(b)

begin to appear. At t_w = 30 min, the clusters aggregate into larger clusters in which little orientational order is observed (Fig. 5.4(j)). From this point onwards until t_w = 120 min, the clusters coalesce continuously until heterogeneous regions of dense clusters and large voids are formed (Fig. 5.4(k-m)). Fig. 5.4(o) shows a region in which a high concentration of particles with little orientational order with respect to each other are seen.

The time-dependent radial distribution function, $g(r)$, reflects the appearance of stacked particles seen in Fig. 5.4(a-f). In Fig. 5.5(a), the $g(r)$ for the sample with the highest degree of visual orientational ordering (ϕ = 0.018, c/c* = 4.0) exhibits a sharp peak at $r = 2b$ for all t_w. The intensity of the peak increases as a function of t_w. Fig. 5.5(b) shows a limiting case of the experiments for which no long-ranged orientational order is observed (ϕ = 0.023 and c/c* = 1.7). Here, the peaks of the $g(r)$ at all t_w are far lower than that shown in Fig. 5.5(a), and a broad peak is fully established at t_w = 90 min.

The subpopulation of particles in clusters and orientational aggregates of size s provide direct physical measures of the microstructural evolution. Fig. 5.6 shows that f_{clust} for $s \geq 2$ uniformly increases for all samples as self-assembly proceeds and reaches a plateau at large t_w. Fig. 5.6(b) shows that two regimes of growth is observed for samples with low c/c* (ϕ = 0.023 and c/c* = 1.7). Fig. 5.7 shows the time-dependent behavior of R_H using the mean cluster size of the self-assembled structures. At c/c* = 4.0 (Fig. 5.7(a)), samples grow slowly with a power law scaling, $R_H \sim t_w^{0.12}$. A further reduction of c/c* to 1.7 results in the appearance of two scalings: at $t_w \leq 20$ min, $R_H \sim t_w^{0.04}$; at $t_w > 120$ min, $R_H \sim t_w^{0.31}$ (Fig. 5.7(b)). The kinetics of orientational growth is shown in Fig. 5.8. Orientational order grows more quickly for the sample at lower ϕ (Fig. 5.8(a), c/c* = 4.0, ϕ = 0.018), where $f_{ordered}$ for $s \geq 3$ grows to 0.34 at t_w = 120 min. Reducing the c/c* even further (Fig. 5.8(b), (c/c* = 1.7, ϕ = 0.023) results in a plateau value of

$f_{ordered}$ up to t_w = 60 min, after which it remains at 0.08 at t_w = 120 min. The same trends are observed for $s \geq 4$.

Discussion

Nematic gels have been previously observed in gels of shape-anisotropic particles [28, 29]. The degree of orientational ordering in our systems is relatively low. The highest value of $f_{ordered}$ is observed in the sample with $\phi = 0.018$ and $c/c^* = 4.0$ at t_w = 120 min ($f_{ordered}$ = 0.34 at $s \geq 3$, $f_{ordered}$ = 0.20 for $s \geq 4$). Despite the small subpopulation of particles that exist in long thread-like chains, the difference between the most ordered and the least ordered sample is significant: exceedingly low values of $f_{ordered}$ are observed in the sample with $\phi = 0.023$ and $c/c^* = 1.6$ ($f_{ordered}$ = 0.08 at $s \geq 3$, $f_{ordered}$ = 0.02 for $s \geq 4$). We also observe a significant decrease in the value of $f_{ordered}$ at $t_w \sim 60$ min for samples with the lowest degree of orientational ordering (Fig. 5.8(b)). These results, contrary to our intuition that a low value of c/c^* should encourage structural rearrangements through rotational motion, show that orientational aggregation of oblate spheroids is favored at high c/c^* and intermediate ϕ. At $\phi = 0.018$, $c/c^* = 4.0$, the interparticle forces are strong enough to form and maintain chain-like structures when particles come into contact, as shown in Fig. 5.4 (a-f). Our work shows that orientational preference is achieved at high c/c^* and intermediate ϕ, but the microscopic origin of orientational order arising at only these values of ϕ remains unclear. Additional information from a structure factor plot where the characteristic cluster size is obtained as a function of time would provide a more precise explanation of the interplay between cluster growth and orientational ordering.

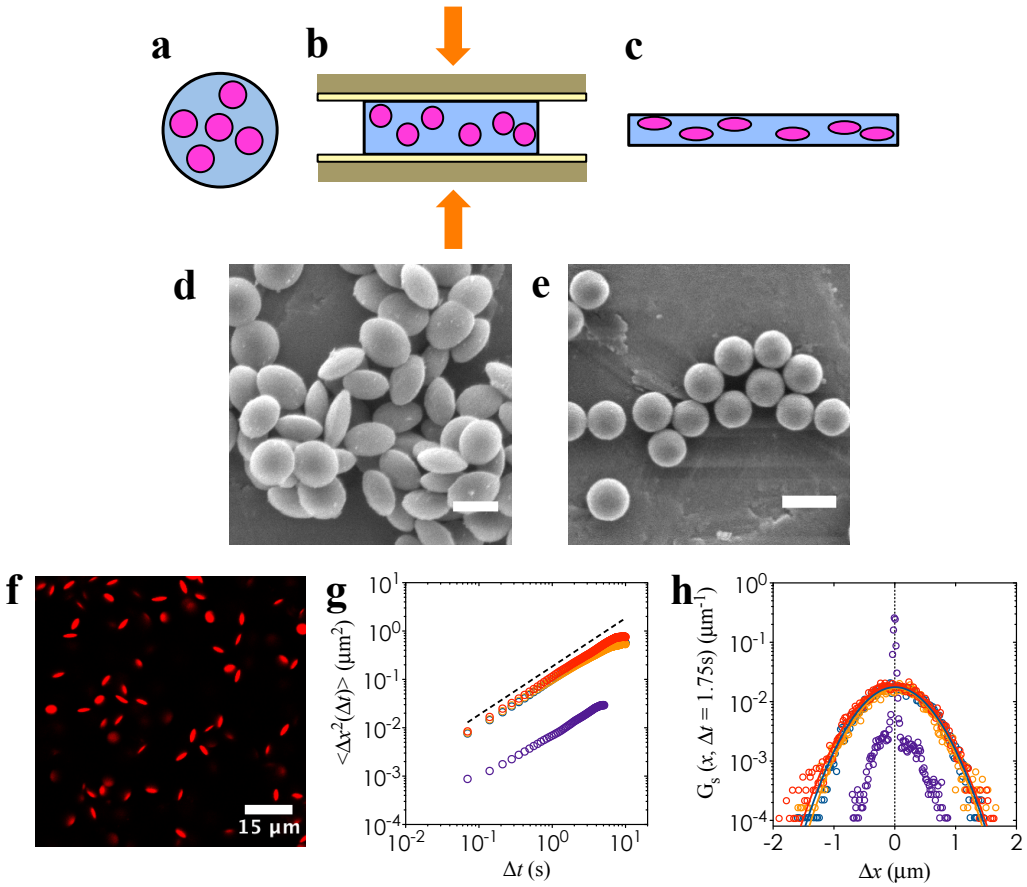

Figure 5.1. Synthesis and stability of PMMA oblate spheroids. Monodisperse PMMA oblate spheroids are generated by (a) embedding PMMA spherical colloids in a PDMS matrix, (b) applying a uniaxial compression at $T > T_g$, and (c) cooling under pressure to room temperature. (d) Representative scanning electron microscopy image of oblate spheroids used in this study, with aspect ratio $l = b/a = 0.46$. (e) Representative scanning electron microscopy image of the PMMA spheres prior to thermomechanical compression. (f) Representative confocal image of a dilute suspension ($\phi = 0.010$) of covalently stabilized spheroids. (g) The 1D mean-squared displacement as a function of lag time and (h) the single-particle van Hove correlation function for $t_w = 48$ hours (red), 60 hours (orange), 96 hours (blue), and 168 hours (purple). Dashed line in (g) represents the orientation-averaged Stokes Einstein translational diffusivity. Both (g) and (h) are generated from the dilute suspension shown in (f). This Figure is taken from a manuscript in preparation [L.C. Hsiao, B.A. Schultz, S.C. Glotzer & M.J. Solomon, *In preparation* (2014)].

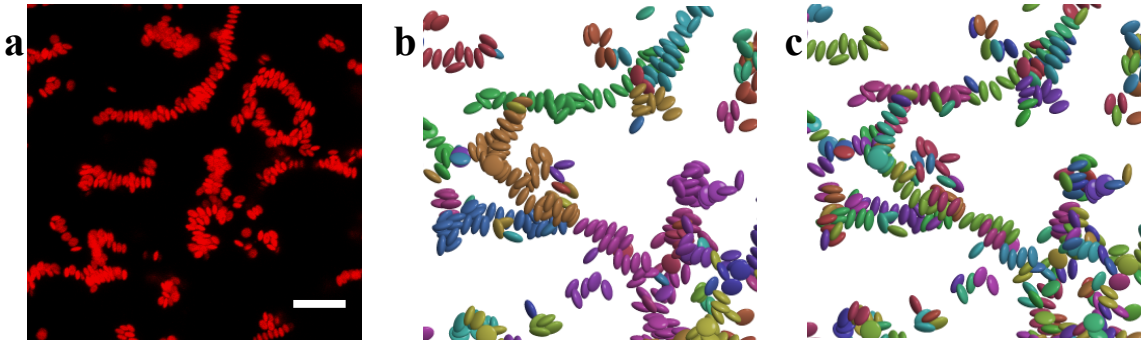

Figure 5.2. 3D image processing of assembled structures. (a) A representative 3D confocal image volume for a sample at $\phi = 0.018$, $c/c^* = 4.0$. (b,c) Renderings of the processed image shown in (a), where particles are colored based on their cluster. In (b), cluster are identified by surface-to-surface distance. In (c), clusters are identified based on the surface-to-surface distance and also by an angular constraint ($\theta \leq 45°$). This Figure is taken from a manuscript in preparation [L.C. Hsiao, B.A. Schultz, S.C. Glotzer & M.J. Solomon, *In preparation* (2014)].

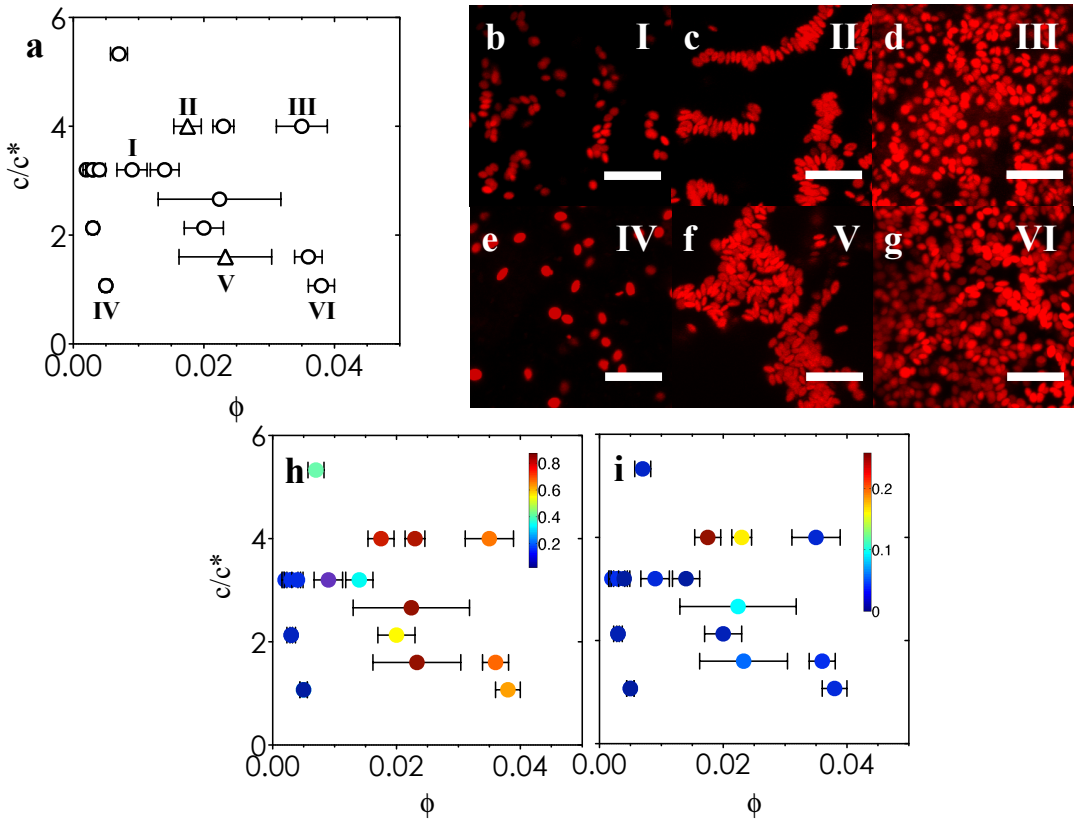

Figure 5.3. Phase behavior and confocal microscopy images of self-assembled structures at t_w = 120 min. (a) Experimental conditions tested in this study. Triangles represent data with corresponding cluster aggregation kinetics study. The representative confocal images of samples with numerical labels (I-VI) in (a) are shown in (b-g): (b, I) $\phi = 0.009 \pm 0.002$, c/c* = 3.2, (c, II) $\phi = 0.018 \pm 0.002$, c/c* = 4.0, (d, III) $\phi = 0.035 \pm 0.004$, c/c* = 4.0, (e, IV) $\phi = 0.005 \pm 0.001$, c/c* = 1.1, (f, V) $\phi = 0.023 \pm 0.02$, c/c* = 1.6, and (g, VI) $\phi = 0.038 \pm 0.002$, c/c* = 1.1. Images in (b-g) are obtained from projections of 80 images (Δz = 9.92 μm) at $z \geq 10$ μm above the coverslip. Scale bars represent 10 μm. The experimental data points are plotted as a function of c/c* and ϕ based on (h) fraction of particles with surface-to-surface cluster size $s \geq 3$, and (i) fraction of particles with orientational cluster size $s \geq 3$. The inset legend shows the color key for different values of f_{clust} and $f_{ordered}$. This Figure is taken from a manuscript in preparation [L.C. Hsiao, B.A. Schultz, S.C. Glotzer & M.J. Solomon, *In preparation* (2014)].

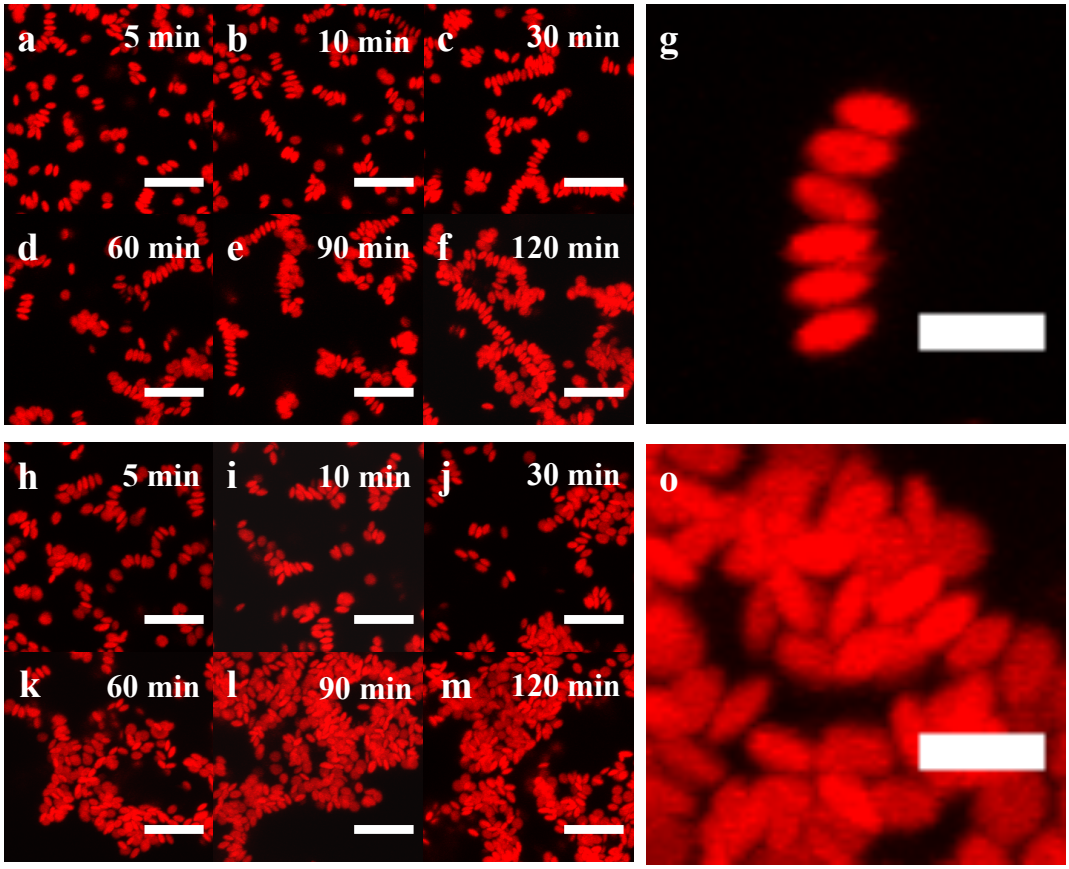

Figure 5.4. Representative confocal images showing structural evolution for an orientationally ordered and a less ordered structure as a function of t_w. An orientationally ordered assembly (ϕ = 0.018, c/c* = 4.0) is shown in (a - f), and an assembly with less orientational order (ϕ = 0.023, c/c* = 1.7) is shown in (g - l). (a, g) t_w = 5 min, (b, h) t_w = 10 min, (c, i) t_w = 30 min, (d, j) t_w = 60 min, (e, k) t_w = 90 min, and (f, l) t_w = 120 min. (f) and (l) are shown in the phase diagram in Figure 4. Images in (a - l) are obtained from projections of 80 images (Δz = 9.92 μm) at $z \geq 10$ μm above the coverslip. Scale bars represent 10 μm. This Figure is taken from a manuscript in preparation [L.C. Hsiao, B.A. Schultz, S.C. Glotzer & M.J. Solomon, *In preparation* (2014)].

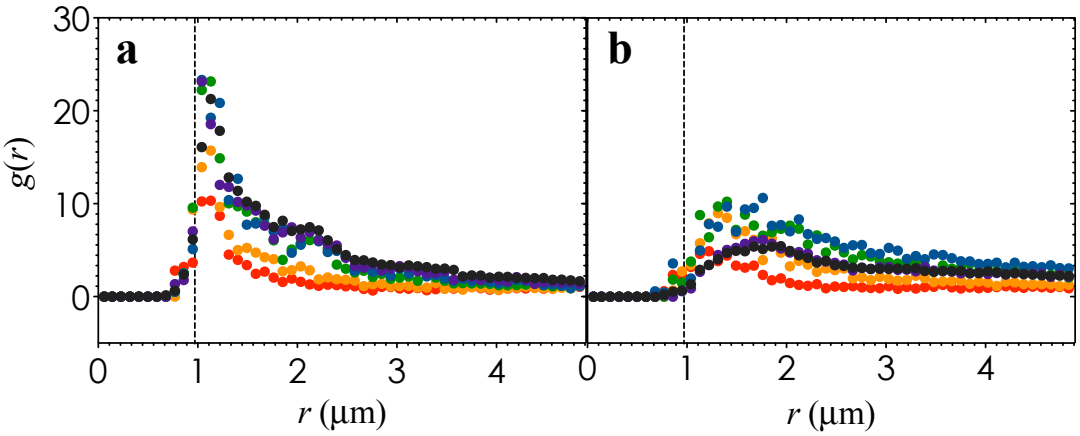

Figure 5.5. Time-dependent radial distribution function. The radial distribution function, $g(r)$, as a function of t_w for: (a) $\phi = 0.018$, $c/c^* = 4.0$, and (b) $\phi = 0.023$, $c/c^* = 1.7$. For clarity, the $g(r)$ is only shown for $t_w = 0$ min (red), $t_w = 10$ min (orange), $t_w = 30$ min (green), $t_w = 50$ min (blue) $t_w = 90$ min (purple), and $t_w = 120$ min (black). Dashed lines indicate the minor axis of the spheroids at $r = 2b$. This Figure is taken from a manuscript in preparation [L.C. Hsiao, B.A. Schultz, S.C. Glotzer & M.J. Solomon, *In preparation* (2014)].

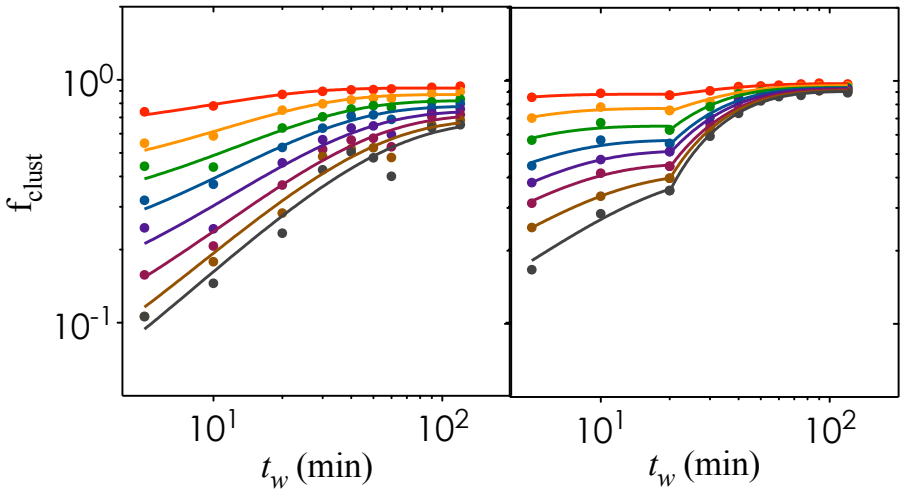

Figure 5.6. Fraction of particles in clusters of size *s* as a function of t_w. The value of f_{clust} is plotted for clusters of: $s \geq 2$ (red), $s \geq 3$ (orange), $s \geq 4$ (green), $s \geq 5$ (blue), $s \geq 6$ (purple), $s \geq 7$ (maroon), $s \geq 8$ (brown), and $s \geq 9$ (grey). Solid lines indicate second order rate equations fitted to the data points. Samples shown here are (a) $\phi = 0.018$, $c/c^* = 4.0$, and (b) $\phi = 0.023$, $c/c^* = 1.6$. This Figure is taken from a manuscript in preparation [L.C. Hsiao, B.A. Schultz, S.C. Glotzer & M.J. Solomon, *In preparation* (2014)].

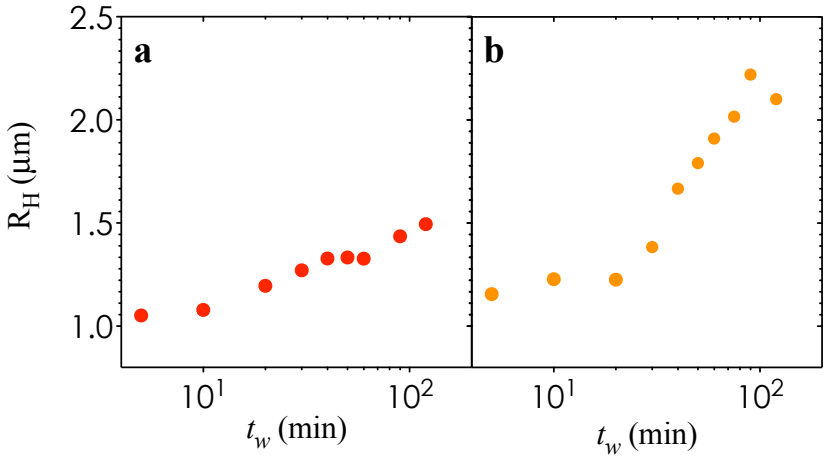

Figure 5.7. Hydrodynamic radius of clusters as a function of t_w. The value of R_H is plotted for (a) $\phi = 0.018$, $c/c^* = 4.0$, and (d) $\phi = 0.023$, $c/c^* = 1.6$. This Figure is taken from a manuscript in preparation [L.C. Hsiao, B.A. Schultz, S.C. Glotzer & M.J. Solomon, *In preparation* (2014)].

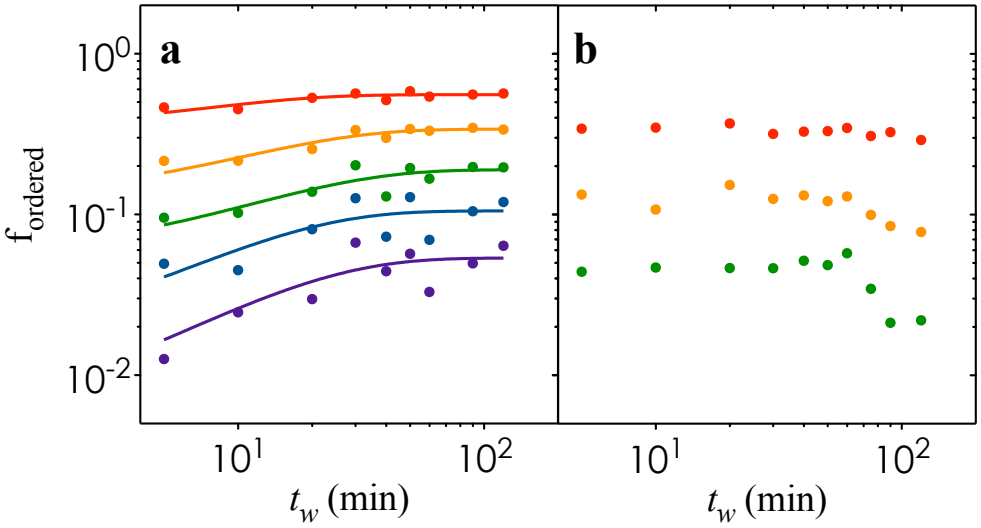

Figure 5.8. Fraction of particles in orientationally-ordered aggregates of size *s*. The value of $f_{ordered}$ is plotted for clusters of: $s \geq 2$ (red), $s \geq 3$ (orange), $s \geq 4$ (green), $s \geq 5$ (blue), and $s \geq 6$ (purple). Solid lines indicate second order rate equations fitted to the data points. Samples shown here are (a) $\phi = 0.018$, $c/c^* = 4.0$, and (b) $\phi = 0.023$, $c/c^* = 1.7$. The data for $s \geq 4$ and $s \geq 5$ are not shown in (c) and (d). This Figure is taken from a manuscript in preparation [L.C. Hsiao, B.A. Schultz, S.C. Glotzer & M.J. Solomon, *In preparation* (2014)].

References

[1] L. Jiang, J. W. J. de Folter, J. Huang, A. P. Philipse, W. K. Kegel, and A. V. Petukhov, *Angewandte Chemie (International ed.)* **52**, 3364 (2013).
[2] T. Gibaud *et al.*, *Nature* **481**, 348 (2012).
[3] A. Kuzyk, R. Schreiber, Z. Fan, G. Pardatscher, E.-M. Roller, A. Högele, F. C. Simmel, A. O. Govorov, and T. Liedl, *Nature* **483**, 311 (2012).
[4] R. P. Goodman, I. a. T. Schaap, C. F. Tardin, C. M. Erben, R. M. Berry, C. F. Schmidt, and A J. Turberfield, *Science* **310**, 1661 (2005).
[5] D. Chakrabarti and D. Wales, *Physical Review Letters* **100**, 127801 (2008).
[6] S. Fejer and D. Wales, *Physical Review Letters* **99**, 86106 (2007).
[7] P. Prybytak, W. Frith, and D. Cleaver, *Interface Focus* **2**, 651 (2012).
[8] K. Zhao and T. Mason, *Physical Review Letters* **99**, 268301 (2007).
[9] F. M. V. D. Kooij and H. N. W. Lekkerkerker, *Journal of Physical Chemistry* **5647**, 7829 (1998).
[10] F. M. van der Kooij, K. Kassapidou, and H. Lekkerkerker, *Nature* **406**, 868 (2000).
[11] B. Ruzicka, E. Zaccarelli, L. Zulian, R. Angelini, M. Sztucki, A. Moussaïd, T. Narayanan, and F. Sciortino, *Nature Materials* **10**, 56 (2010).
[12] M. Okamoto, P. H. Nam, P. Maiti, T. Kotaka, N. Hasegawa, and A. Usuki, *Nano Letters* **1**, 295 (2001).
[13] E. Paineau *et al.*, *Phys Chem B* **113**, 15858 (2009).
[14] M. Dijkstra, J. Hansen, and P. Madden, *Phys Rev Lett* **75**, 1 (1995).
[15] D. Florea and H. M. Wyss, *Journal of Colloid and Interface Science* **416**, 30 (2014).
[16] Y. Hu, J. Ge, T. Zhang, and Y. Yin, *Advanced Materials* **20**, 4599 (2008).
[17] I. Zhang, C. P. Royall, M. A. Faers, and P. Bartlett, *Soft Matter* **9**, 2076 (2013).
[18] L. Antl, J. W. Goodwin, R. D. Hill, R. H. Ottewill, S. M. Owens, S. Papworth, and J. A. Waters, *Colloids and Surfaces* **17**, 67 (1986).
[19] A. I. Campbell and P. Bartlett, *Journal of Colloid and Interface Science* **256**, 325 (2002).
[20] Z. Zhang, P. Pfleiderer, A. B. Schofield, C. Clasen, and J. Vermant, *Journal of the American Chemical Society* **133**, 392 (2010).
[21] L. C. Hsiao, R. S. Newman, S. C. Glotzer, and M. J. Solomon, *Proceedings of the National Academy of Sciences USA* **109**, 16029 (2012).
[22] H. Brenner, *International Journal of Multiphase Flow* **1**, 195 (1974).
[23] D. Mukhija and M. J. Solomon, *Journal of Colloid and Interface Science* **314**, 98 (2007).
[24] C. J. Dibble, M. Kogan, and M. J. Solomon, *Physical Review E* **74**, 041403 (2006).
[25] G. Crocker J.C., D.G., *Journal of Colloid and Interface Science* **179**, 298 (1996).
[26] A. Mohraz and M. J. Solomon, *Langmuir* **21**, 5298 (2005).
[27] S. Wegner, T. Borzsonyi, T. Bien, G. Rose, and R. Stannarius, *Soft Matter* **8**, 10950 (2012).
[28] K. R. Purdy, Z. Dogic, S. Fraden, A. Rühm, L. Lurio, and S. G. J. Mochrie, *Physical Review E* **67**, 031708 (2003).
[29] M. J. Solomon and P. T. Spicer, *Soft Matter* **6**, 1391 (2010).

CHAPTER 6

Effect of surface roughness on the rheology and dynamics of concentrated suspensions

Abstract

Surface roughness is known to increase the mechanical properties of concentrated suspensions and jammed systems. We synthesize monodisperse smooth (particle diameter, $2a$ = 2.3 μm ± 4%) and rough PMMA colloids ($2a$ = 2.1 μm ± 4%, root-mean-squared roughness = 94 nm, largest features ~ 300 nm) and suspend them in a solvent that is refractive index and density matched. Tetrabutylammonium chloride is added at a concentration of 1 mM to provide charge screening. We note a significant reduction of the critical shear rate required for shear thickening in suspensions of rough colloids at high particle loading (weight fraction, $\phi_w \geq 0.50$). These results motivate a comparison of the translational diffusivity of suspensions consisting of smooth and rough colloids using fast confocal laser scanning microscopy. We find a negligible difference in the time-dependent translational diffusivity between smooth and rough colloids. The text in this chapter is taken from a manuscript in preparation [L.C. Hsiao, D. Beltran-Villegas, I. Saha Dalal, E. Glynos, M.E. Szakasits, P.F. Green, R.G. Larson & M.J. Solomon, *In preparation* (2014)].

Introduction

Brownian motion and thermal fluctuations play an important role on colloidal length scales: phase behavior and rheological phenomenon are affected by hydrodynamic interactions experienced by individual particles. For instance, attractive bonding in colloidal gels results in arrested dynamics, and the resultant viscoelastic modulus can be modeled as a function of the ensemble-averaged localization length of constituent particles [1, 2]. Another example is that of a colloidal glass, where the linear elasticity can be predicted from the glassy dynamics imposed by crowding [3]. Surface asperities can lead to tangential forces between colloids and significantly increase stress-bearing capabilities [4]. For example, frictional contacts play a critical role in the discontinuous shear thickening behavior seen at high particle loading [5], where surface roughness reduces the shear rate needed for jamming to occur [6]. Although there are a number of potential origins of these rheological effects, a likely contributor would be the effect of roughness on microscopic dynamics such as translational and rotational diffusion.

Quantifying the translational motion in concentrated colloidal suspensions in real time and space has been accomplished with fast confocal laser scanning microscopy. Three-dimensional imaging provided experimental support of dynamical heterogeneities near the colloidal glass transition [7], and showed that the local dynamics is a function of the structural relaxation on characteristic cluster size scales [8]. The diffusive behavior of concentrated suspensions can be separated into regimes corresponding to short, intermediate, and long time scales. The short-time behavior plays an important role in the high frequency viscosity in hard spheres [9] where the perturbation from equilibrium structure is sufficiently small [10]. At intermediate times, subdiffusive behavior is correlated with caging. The long time self-diffusivity diverges close to the maximum packing fraction [11] and is particularly sensitive to

the hydrodynamic interactions imposed by long-ranged electrostatics in concentrated suspensions [12, 13].

Here, we examine the effect of surface roughness on the rheological behavior of colloidal suspensions with weight fractions ranging from 0.30 to 0.55. We measure changes in both shear thickening and viscoelastic properties as a function of surface roughness. The microscopic origins of these observations is explored by measurement of the translational diffusivity of smooth and rough colloids within these suspensions.

Materials and Methods

Smooth and rough PMMA colloids in dense suspensions

We synthesize size-monodisperse poly(methyl methacrylate) (PMMA) colloids sterically stabilized with a grafted layer of poly(12-hydroxystearic acid) (PHSA) using the method of Antl et al. [14]. The thickness of the PHSA steric layer is estimated to be 10 - 14 nm [15]. Smooth colloids with diameter $2a$ = 2.3 μm ± 4% (Figure 6.1a) and rough colloids with diameter $2a$ = 2.1 μm ± 4% (Figure 6.1b) are used in this study. (For rough colloids, the value of $2a$ is determined using the edge-to-edge distance of ~ 80 independent colloids.) Surface roughness is introduced through the controlled addition of the cross-linking agent ethylene glycol dimethacrylate (EGDM) at a concentration of 1.8 wt% compared to the monomer concentration [16] during the synthesis. The cross-linker is thought to induce the formation of large oligomers early on in the reaction, which gradually aggregate into rough colloids. Atomic force microscopy (AFM) measurements[††] show that the root-mean-squared (RMS) surface roughness, σ, is 94 nm and that the deepest features observed are on the order of ~ 300 nm[‡‡] (Figure 6.1(c)). The RMS roughness

[††] AFM measurements are collected by Dr. Emmanouil Glynos.
[‡‡] Roughness characterization is performed by Dr. Daniel Beltran-Villegas.

is obtained by fitting the measurements from the AFM to a sphere with the same value of $2a$ as the rough particle. All PMMA colloids are dyed with fluorescent Nile Red to allow for direct visualization with confocal microscopy.

Particles are suspended at weight fractions, ϕ_w, ranging between 0.02 and 0.55 in a mixture of cyclohexylbromide (CHB) and decalin (66%:34% v/v) that provides optimal refractive index and density matching between the solvent and the colloids. We choose to report the weight fractions here because of the difficulty in determining the volume of a particle with large surface asperities. For smooth spherical colloids, the value of ϕ_w corresponds to the volume fraction. Tetrabutylammonium chloride salt (TBAC) is added at a concentration of 1 mM to provide charge screening. The Debye length of the solvent, κ^{-1} = 78 nm, is obtained from conductivity measurements of the solvent, and the zeta potential, ζ, is estimated to be $\leq$ 10 mV. We note that the surface roughness length scale is comparable to the Debye length (σ/κ^{-1} = 1.2). The solvent viscosity at infinite dilution (η = 2.5 × 10^{-3} Pa·s at T = 22°C) is measured with a Canon viscometer.

Image acquisition and processing of dense suspensions

We use confocal microscopy to directly visualize the dynamics of individual colloids in these dense suspensions. Suspensions are loaded into 2 ml vials attached to a 1.5 coverslip, and are allowed to rest for 10-15 minutes prior to imaging. A confocal microscope (Nikon A1Rsi) equipped with a resonant scanner head is used to capture 2D images at high speed (lag time, Δt = 0.0737 s). Images are captured with dimensions of 41.0 × 41.0 μm (pixel size = 80 nm) at a minimum of $\Delta z \geq$ 10 μm above the coverslip to avoid wall interactions from interfering with dynamical measurements. Three independent image series are captured at random locations

within each sample. In specific cases (ϕ_w = 0.02, 0.30, 0.45 with smooth colloids), the dynamical measures are verified using an additional independent sample. Representative confocal images of dense suspensions of smooth colloids (ϕ_w = 0.20, 0.30, 0.35, 0.40, 0.45, 0.50, and 0.55) and of rough colloids (ϕ_w = 0.20, 0.30, 0.35, 0.40, 0.45, 0.49 and 0.54) are shown in Figures 6.2 and 6.3 respectively.

The time-resolved images are processed using a edge-detection Hough transform algorithm [17]. Briefly, the gradient at the edges of individual colloids is used to determine the boundary between the colloid and the solvent. Multiple circles fitted to the edge of the colloids are used to locate the center of the particle in a region where the frequency of overlap is at a maximum. The Hough transform is particularly suitable for dense and gelled systems, where the brightest pixel is located at an offset to the geometric center of a particle. Representative images of dense suspensions (smooth and rough colloids, $\phi_w \geq 0.535$) that have been processed with the Hough transform are shown in Figures 6.4(a) and (b), where the particle centroids are overlaid on the raw images. The processed images show that the position of individual colloids, regardless of their surface roughness, are identified correctly even in the densest suspensions used in this study.

The self-part of the one-dimensional (1D) van Hove correlation at Δt = 1.75 s for suspensions of smooth and rough colloids are shown in Figures 6.4(c) and (d). These correlations show that subpixel resolution is achieved, and that suspensions display Gaussian dynamics. The 1D mean-squared displacement (MSD), $<\Delta x^2(\Delta t)>$, of the suspensions are obtained for each ϕ_w. For fully diffusive samples, the long-time self-diffusion coefficient, D_∞^s, is given by [18]

$$\lim_{\Delta t \to \infty} \left\langle \Delta x^2 (\Delta t) \right\rangle = 2 D_\infty^s (\Delta t) \qquad (6.1)$$

For subdiffusive behavior in the intermediate regimes between short- and long-time behavior, a time-dependent self-diffusivity, $D_s(\Delta t)$, can be obtained by calculating $\Delta x^2(\Delta t)/\Delta t$ at individual values of Δt [19]. The translational Stokes-Einstein diffusivity at infinite dilution is given by $D_0 = k_B T / 6\pi\eta a$, where k_B is the Boltzmann constant, T is the temperature, η is the solvent viscosity, and a is the radius of the particle. The Brownian time scale, t_I, is estimated as the time required for a particle to diffuse its own radius at infinite dilution (a^2/D_0).

Rheological characterization

The viscoelasticity and viscosity of all samples are characterized using a stress-controlled rheometer (TA Instruments, AR-G2). Colloidal suspensions are loaded onto a Peltier plate at T = 25°C. A 6 cm steel cone-and-plate geometry is lowered to a truncation gap of 48 μm while rotating slowly (angular frequency, ω = 0.1 rad/s) to minimize the formation of bubbles at the interface. A solvent trap filled with CHB and decalin is used to minimize evaporation over the duration of the experiments. The suspensions are presheared at 287 s^{-1} for 1 minute, with the exception of dense suspensions (suspensions with $\phi_w \geq 0.50$ are presheared at 0.5 s^{-1} for 5 minutes due to the risk of fracturing the sample). The strain-dependent elastic and viscous moduli, $G'(\gamma)$ and $G''(\gamma)$, are measured for smooth and rough colloids (ϕ_w = 0.35, 0.40, 0.45, 0.50, 0.535, and 0.55) using oscillatory stress sweep measurements where the applied stress, τ, varies from 0.01 to 1000 Pa at a fixed frequency of ω = 1 rad/s. In addition, a unidirectional shear (τ = 0.01 to 1000 Pa) is applied to characterize the viscosity and the shear thickening behavior of select samples (smooth colloids: ϕ_w = 0.40, 0.50, 0.535, and 0.55; rough colloids: ϕ_w = 0.40, 0.50, and 0.535). Viscosity measurements are taken by averaging 10 seconds of data after

shearing at a particular value of τ for 1 minute (Figure 6.6(d)). Increasing ϕ_w beyond 0.535 for rough colloids results in a jammed suspension that is difficult to load evenly onto the rheometer.

Results

Viscoelastic behavior

The strain-dependent elastic and viscous moduli normalized by the diameter of the particle and thermal energy, $G'(\gamma)(2a)^3/k_BT$ and $G''(\gamma)(2a)^3/k_BT$, are plotted as a function of the applied strain, γ, for suspensions of smooth and rough colloids in Figure 6.5(a) and (b). The size-normalized linear plateau of the strain-dependent elastic modulus, $G'(2a)^3/k_BT$, is plotted against ϕ_w in Figure 6.5(c). At $\phi_w \leq 0.50$, the value of $G'(2a)^3/k_BT$ remains constant for both smooth and rough colloids, to within experimental error. At $\phi_w = 0.535$, the value of $G'(2a)^3/k_BT$ for rough colloids is a factor of five larger than measured for smooth colloids, and a factor of three larger than theoretical predictions of the high frequency elastic modulus [20, 21]. This modest increase is larger than the largest experimental error measured in the system of smooth colloids ($\Delta G'/G' \sim 93\%$). Additional replicates at this condition is necessary to decouple the effect of roughness from experimental error. The suspension of rough colloids at $\phi_w = 0.535$ also displays strain stiffening behavior at $\gamma \geq 0.1$ (Figure 6.5(b)), which is not seen in suspensions of smooth colloids even at $\phi_w = 0.55$. These results suggest that the effect of roughness on the linear elastic modulus is modest, observable only at the highest weight fractions ($\phi_w \geq 0.535$) close to the jamming transition of the rough colloids.

Shear thickening behavior

The effect of surface roughness on the shear thickening behavior of dense suspensions is pictorially shown in Figure 6.6(a). Here, two glass vials loaded with the same weight fraction of colloids (ϕ_w = 0.52) are photographed immediately after being turned upside down. The vial on the left shows that the suspension containing rough colloids relax on a timescale that is far greater than the vial on the right containing a suspension of smooth colloids, resulting in shear thickening flow under the influence of gravity. The particle loading at which the onset of shear thickening is observed is quantified for both smooth (Figure 6.6(b)) and rough particles (Figure 6.6(c)). These plots show that shear thinning of smooth particles occurs at low shear rates, where $\dot{\gamma} < 10^0 s^{-1}$. The shear thickening transition appears as an upturn in the plot at a critical shear rate, $\dot{\gamma}_c$. Figure 6.6(b) shows that smooth particles begin to exhibit shear thickening at ϕ_w = 0.50, with $\dot{\gamma}_c = 367 s^{-1}$. At ϕ_w = 0.55, the value of $\dot{\gamma}_c$ decreases slightly to 287 s^{-1}. A significant difference in the onset of shear thickening is observed in the suspension of rough colloids, as shown in Figure 6.6(c). Shear thickening is seen at ϕ_w = 0.40 ($\dot{\gamma}_c = 181 s^{-1}$). As ϕ_w increases to 0.50, $\dot{\gamma}_c$ decreases drastically to 13 s^{-1}, and at the largest ϕ_w tested (ϕ_w = 0.535), the value of $\dot{\gamma}_c$ further decreases to 0.62 s^{-1}.

The time-dependent nature of Figures 6.6(b) and (c) are illustrated by measuring the viscosity as a function at three shear rates (τ = 0.1 Pa, $\dot{\gamma} = (0.011 \pm 0.004) s^{-1}$; τ = 10 Pa, $\dot{\gamma} = (2.1 \pm 0.4) s^{-1}$; and τ = 100 Pa, $\dot{\gamma} = (4.6 \pm 1.1) s^{-1}$) for suspensions of rough colloids at ϕ_w = 0.50. Figure 6.6(d) shows that at $\dot{\gamma} = 0.011 s^{-1}$, the viscosity fluctuates continuously and does not appear to reach a steady state. The viscosity at $\dot{\gamma} = 2.1 s^{-1}$ decreases towards a plateau value at large times ($t \sim 10^3$ s), but no similar plateau value in viscosity can be observed in for $\dot{\gamma} = 4.6 s^{-1}$. These results show that the viscosity we plot in Figures 6.6(b) and (c) is not at steady state,

because shear thickening is a transient process which involves fluctuations in shear stress from frictional motion and large-scale strain heterogeneities [22].

Effect of surface roughness on the translational self-diffusivity

The 1D translational MSD plots for suspensions of smooth and rough colloids are shown in Figures 6.7(a) and (b). Figure 6.7(a) shows that for dilute suspensions of smooth colloids (ϕ_w = 0.02), the slope of the MSD is 0.94 ± 0.08 and is characteristic of diffusive behavior to within experimental error. As ϕ_w increases, the suspensions display increasingly subdiffusive behavior; the slope of the MSD decreases from 0.90 ± 0.12 at ϕ_w = 0.20 to 0.39 ± 0.03 at ϕ_w = 0.55. The suspensions of rough colloids display the same behavior as the smooth colloids (Figure 6.7(b)). A closer comparison between the MSD curves for smooth and rough colloids (Figure 6.8) show that there is quantitatively no difference in the measured translational motion of colloids up to ϕ_w = 0.55 (the data for the rough colloids in Figure 6.8(f) is at ϕ_w = 0.535). The time-dependent diffusivity shows a similar trend (Figure 6.9(a) and (b)). We plot the value of $D_s(\Delta t)$ at Δt = 0.074 s, 1.03 s, and 8.03 s for both smooth and rough colloids in Figure 6.10. Our data is plotted along with theoretical predictions of the short-time self-diffusivity in hard sphere suspensions [9] ($\phi \leq 0.50$) and experimental data from dynamic light scattering [12]. Significant deviation (to within experimental error) from short-time behavior is seen at $\Delta t \geq 8.03$ s for smooth colloids and at $\Delta t \geq 1.03$ s, suggesting that particles exhibit subdiffusive dynamics beyond this lag time. The data in Figures 6.9 and 6.10 show that there is no significant difference in $D_s(\Delta t)$ between smooth and rough colloids at $\phi_w \leq 0.30$. Deviations from hard sphere behavior are observed with

increasing ϕ_w, suggesting that the compression of the Debye layer at high ϕ_w plays an important role in the short-time diffusivity.

Discussion

Our results show that surface roughness with a length scale that is on par with the Debye length induces changes in suspension rheology at high particle loading ($\phi \geq 0.50$). While Figure 6.5 shows that the increase in linear elasticity is modest, Figure 6.6 shows that the roughness effect on shear thickening behavior is especially apparent. One of the most well-studied mechanisms of shear thickening is hydrocluster formation in less densely packed systems [23]. With systems close to the jamming transition, extremely strong shear thickening behavior has been proposed to caused by strain localization and stress chain propagaion [31]. The latter is commonly encountered in granular flows and is a plausible explanation for the drastic decrease in the critical shear rate required for the onset of shear thickening in rough colloids (Figure 6.6(c)). Beyond a critical shear rate, these hydrodynamically coupled colloids form clusters that can span across the entire sample in dense suspensions that exhibit discontinuous shear thickening ($\phi \geq 0.56$) [5].

The direct measurement of rotational motion of rough colloids in jammed systems would illustrate the effect of rotational hindrance on shear thickening behavior of a variety of colloidal suspensions. The decoupling of rotational and translational diffusivity has previously been reported in colloidal glasses [27], but the effect of surface roughness on this decoupling has yet to be explored. One potential method of tracking rotational motion is to deposit a thin metallic layer on one hemisphere of a PMMA colloid to provide a refractive index contrast (Appendix B). Examples of this type of technique have been provided in the past [28, 29]. The implementation of tracking algorithms that allows the quantitative characterization of rotational motion in dense

suspensions would provide a clear explanation of the effect of roughness on a variety of rheological phenomenon, as seen in the enhancement in the shear thickening capability and the viscoelastic moduli of colloidal glasses studied here.

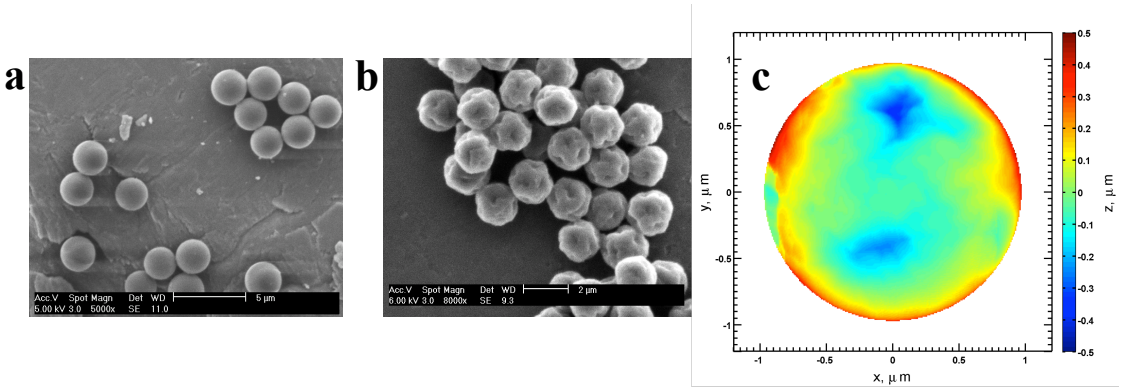

Figure 6.1. Monodisperse smooth and rough colloids. Scanning electron microscopy images of (a) smooth colloids with $2a = 2.3$ µm ± 4% and (b) rough colloids with $2a = 2.1$ µm ± 4%. (c), Representative atomic force microscopy image of a rough particle, where the deviation from a sphere of size $2a = 2.1$ µm is used to generate RMS roughness. This Figure is taken from a manuscript in preparation [L.C. Hsiao, D. Beltran-Villegas, I. Saha Dalal, E. Glynos, M.E. Szakasits, P.F. Green, R.G. Larson & M.J. Solomon, *In preparation* (2014)].

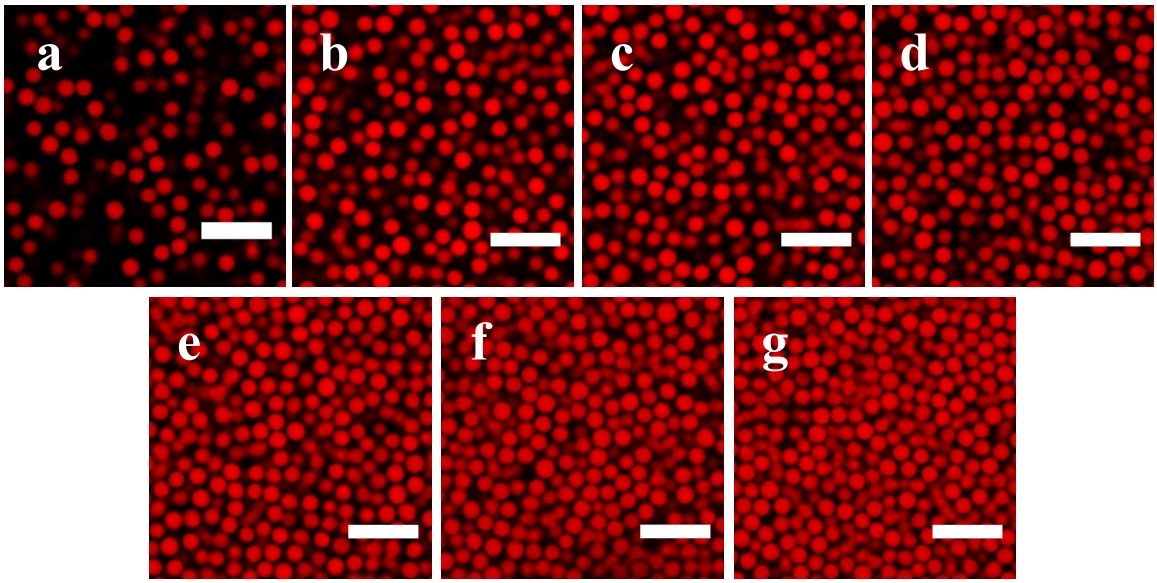

Figure 6.2. Representative confocal microscopy images of suspensions of smooth colloids. The weight fractions used in the measurements of translational diffusivity are: (a) $\phi_w = 0.20$, (b) $\phi_w = 0.30$, (c) $\phi_w = 0.35$, (d) $\phi_w = 0.40$, (e) $\phi_w = 0.45$, (f) $\phi_w = 0.50$, and (g) $\phi_w = 0.55$. Images are taken at least 10 μm above the coverslip. Scale bars represent 10 μm. This Figure is taken from a manuscript in preparation [L.C. Hsiao, D. Beltran-Villegas, I. Saha Dalal, E. Glynos, M.E. Szakasits, P.F. Green, R.G. Larson & M.J. Solomon, *In preparation* (2014)].

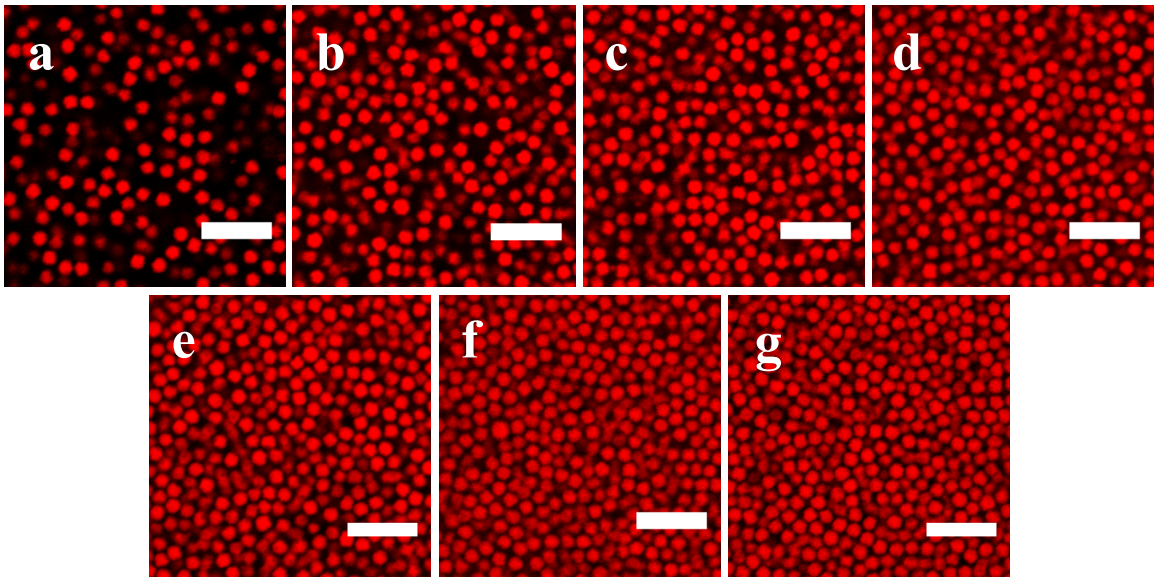

Figure 6.3. Representative confocal microscopy images of suspensions of rough colloids. The weight fractions used in the measurements of translational diffusivity are: (a) $\phi_w = 0.20$, (b) $\phi_w = 0.30$, (c) $\phi_w = 0.35$, (d) $\phi_w = 0.40$, (e) $\phi_w = 0.49$, (f) $\phi_w = 0.54$, and (g) $\phi_w = 0.55$. Images are taken at least 10 μm above the coverslip. Scale bars represent 10 μm. This Figure is taken from a manuscript in preparation [L.C. Hsiao, D. Beltran-Villegas, I. Saha Dalal, E. Glynos, M.E. Szakasits, P.F. Green, R.G. Larson & M.J. Solomon, *In preparation* (2014)].

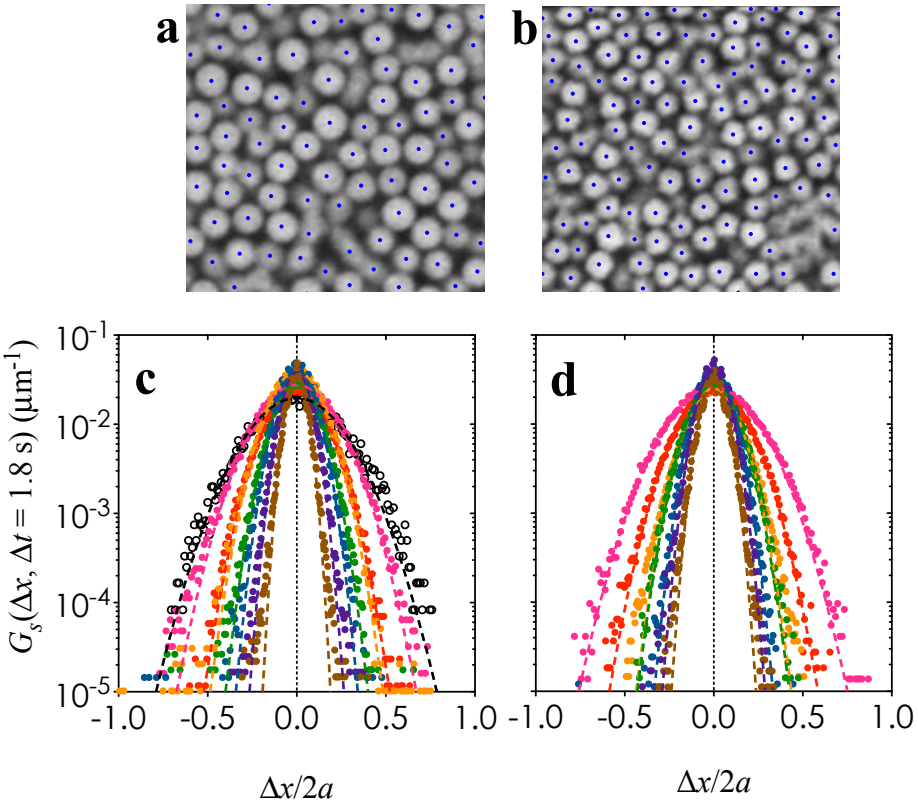

Figure 6.4. Fidelity of 2D particle tracking algorithm. Particle centroids identified using the Hough transform are overlaid on greyscale raw images for (a) smooth colloids, $\phi_w = 0.55$ and (b) rough colloids, $\phi_w = 0.535$. The single-particle self-part of the 1D van Hove correlations at Δt = 1.8 s are shown for (c) smooth and (d) rough colloids as a function of ϕ_w: $\phi_w = 0.02$ (black), ϕ_w = 0.20 (pink), $\phi_w = 0.30$ (red), $\phi_w = 0.35$ (orange), $\phi_w = 0.40$ (green), $\phi_w = 0.45$ (blue). For (c), ϕ_w = 0.50 (purple) and $\phi_w = 0.55$ (brown); for (d), $\phi_w = 0.487$ (purple) and $\phi_w = 0.535$ (brown). Dashed lines are Gaussian fits to the data points. This Figure is taken from a manuscript in preparation [L.C. Hsiao, D. Beltran-Villegas, I. Saha Dalal, E. Glynos, M.E. Szakasits, P.F. Green, R.G. Larson & M.J. Solomon, *In preparation* (2014)].

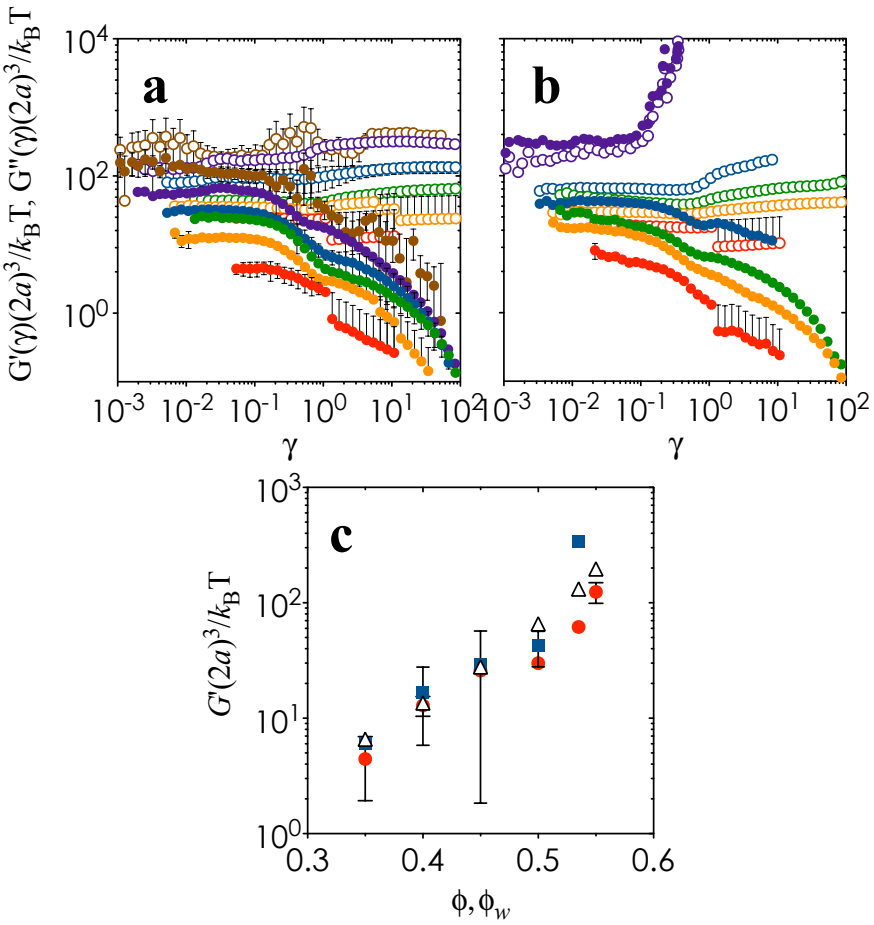

Figure 6.5. Normalized elastic and viscous moduli for smooth and rough colloids. The strain-dependent elastic and loss moduli, normalized by particle size and thermal energy, is shown for suspensions of (a) smooth colloids and (b) rough colloids. Solid symbols represent the elastic modulus and open symbols represent the loss modulus. Here, ϕ_w = 0.35 (red), ϕ_w = 0.40 (orange), ϕ_w = 0.45 (green); for (a), ϕ_w = 0.50 (blue), ϕ_w = 0.535 (purple), and ϕ_w = 0.55 (brown); for (b), ϕ_w = 0.487 (blue) and ϕ_w = 0.535 (purple). The linear elastic modulus normalized by particle size and thermal energy is shown in (c) for smooth (red circles) and rough (blue squares) colloids of different ϕ_w. Error bars represent standard deviations. Data from [30] are plotted as a function of ϕ (open triangles). This Figure is taken from a manuscript in preparation [L.C. Hsiao, D. Beltran-Villegas, I. Saha Dalal, E. Glynos, M.E. Szakasits, P.F. Green, R.G. Larson & M.J. Solomon, *In preparation* (2014)].

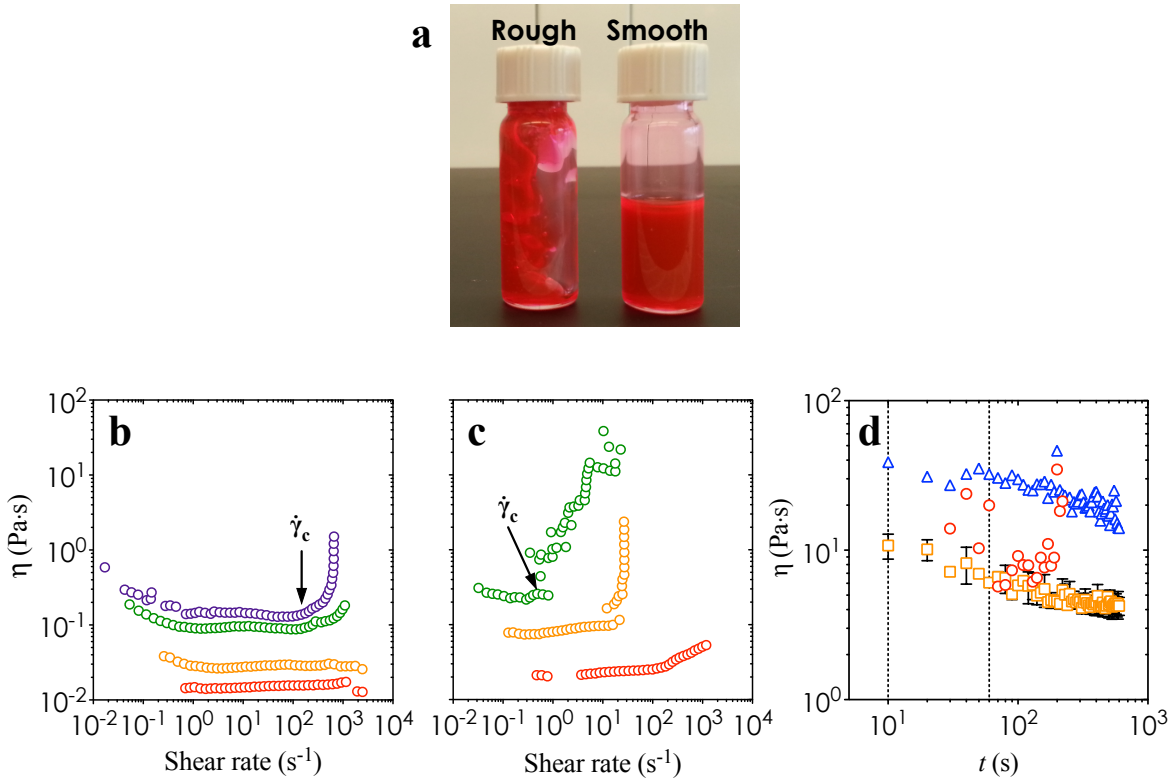

Figure 6.6. Shear thickening behavior of smooth and rough colloids. (a) A pictorial representation of shear thickening in vials containing suspensions of rough and smooth colloids (ϕ_w = 0.52). Both vials were flipped upside down and photographed immediately. The viscosity is plotted as a function of shear rate for (b) smooth colloids and (c) rough colloids: ϕ_w = 0.40 (red), ϕ_w = 0.50 (orange), ϕ_w = 0.535 (green), and ϕ_w = 0.55 (purple). Arrows point to the critical shear rate at the onset of shear thickening. (d), The time-dependent viscosity is plotted as a function of shear time for τ = 0.1 Pa (red circles), τ = 10 Pa (orange squares), and τ = 100 Pa (blue triangles). Dashed lines represent the measurement time for which data points in (b) and (c) are generated. Error bars shown are standard deviations. This Figure is taken from a manuscript in preparation [L.C. Hsiao, D. Beltran-Villegas, I. Saha Dalal, E. Glynos, M.E. Szakasits, P.F. Green, R.G. Larson & M.J. Solomon, *In preparation* (2014)].

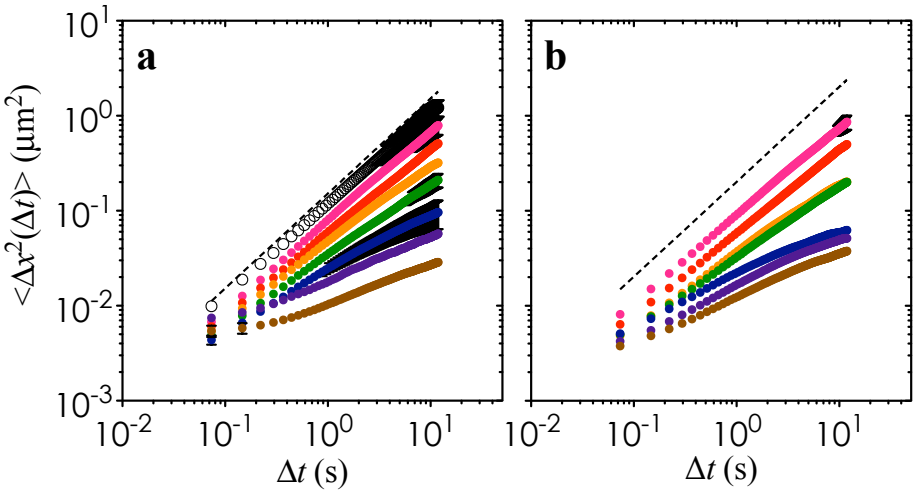

Figure 6.7. 1D mean-squared displacement of smooth and rough colloids. The MSD is plotted for (a) smooth colloids and (b) rough colloids as a function of lag time for ϕ_w = 0.02 (black open circles), ϕ_w = 0.20 (pink), ϕ_w = 0.30 (red), ϕ_w = 0.35 (orange), ϕ_w = 0.40 (green), ϕ_w = 0.45 (blue). For (a), ϕ_w = 0.50 (purple) and ϕ_w = 0.55 (brown); for (b), ϕ_w = 0.487 (purple) and ϕ_w = 0.535 (brown). Dashed line represents Stokes-Einstein diffusivity at infinite dilution. Error bars shown are standard deviations. This Figure is taken from a manuscript in preparation [L.C. Hsiao, D. Beltran-Villegas, I. Saha Dalal, E. Glynos, M.E. Szakasits, P.F. Green, R.G. Larson & M.J. Solomon, *In preparation* (2014)].

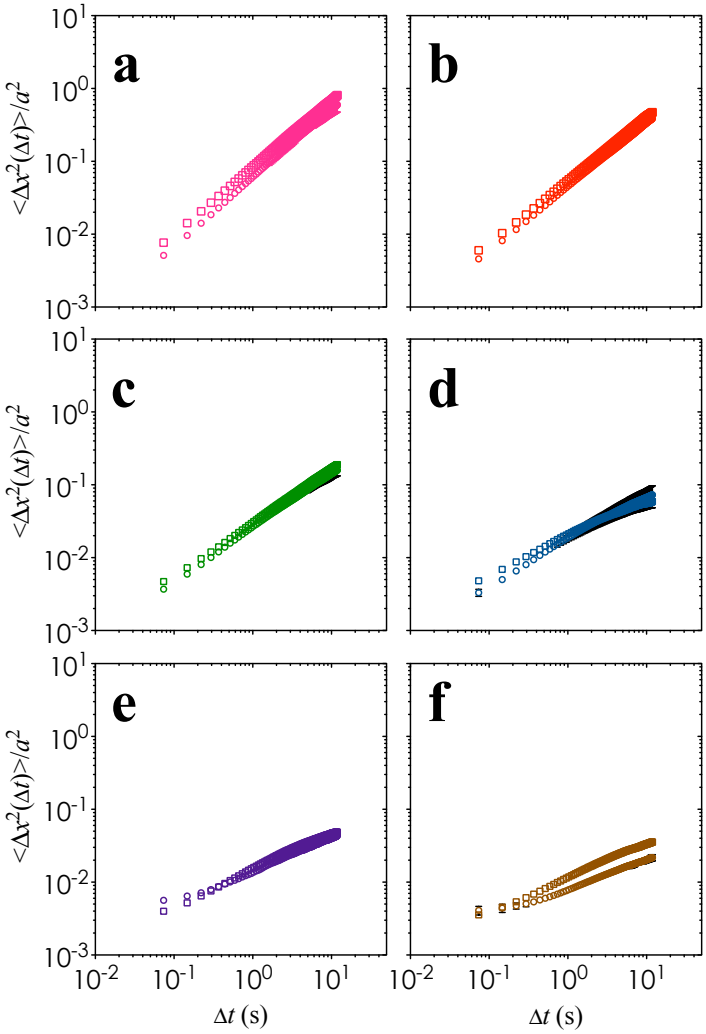

Figure 6.8. Comparison of the normalized 1D MSD of smooth and rough colloids. Data for smooth colloids are shown as open circles and data for rough colloids are shown as open squares. (a), ϕ_w = 0.20; (b) ϕ_w = 0.30; (c) ϕ_w = 0.40; (d) ϕ_w = 0.45; (e) ϕ_w = 0.50; (f) ϕ_w = 0.535 (rough) and 0.55 (smooth). This Figure is taken from a manuscript in preparation [L.C. Hsiao, D. Beltran-Villegas, I. Saha Dalal, E. Glynos, M.E. Szakasits, P.F. Green, R.G. Larson & M.J. Solomon, *In preparation* (2014)].

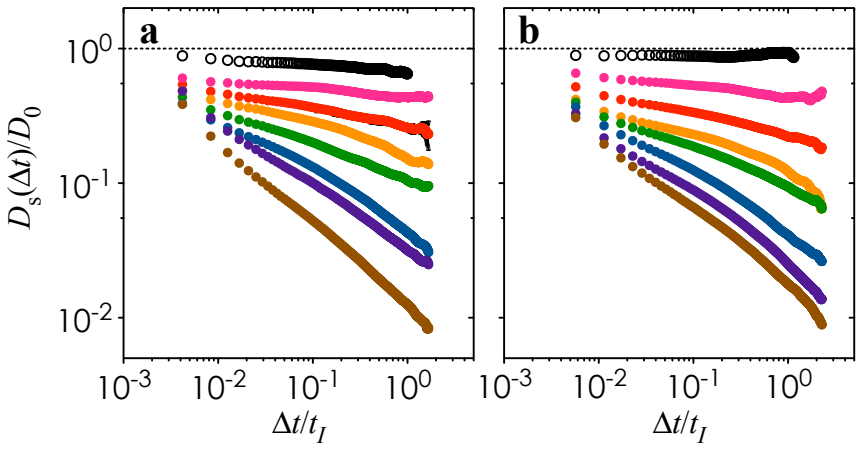

Figure 6.9. Time-dependent translational diffusivity normalized by Stokes-Einstein diffusivity as a function of lag time normalized by the Stokes-Einstein diffusion time. The data for (a) smooth and (b) rough colloids are shown for $\phi_w = 0.02$ (black open circles), $\phi_w = 0.20$ (pink), $\phi_w = 0.30$ (red), $\phi_w = 0.35$ (orange), $\phi_w = 0.40$ (green), $\phi_w = 0.45$ (blue). For (a), $\phi_w = 0.50$ (purple) and $\phi_w = 0.55$ (brown); for (b), $\phi_w = 0.487$ (purple) and $\phi_w = 0.535$ (brown). Dashed line represents Stokes-Einstein diffusivity at infinite dilution. This Figure is taken from a manuscript in preparation [L.C. Hsiao, D. Beltran-Villegas, I. Saha Dalal, E. Glynos, M.E. Szakasits, P.F. Green, R.G. Larson & M.J. Solomon, *In preparation* (2014)].

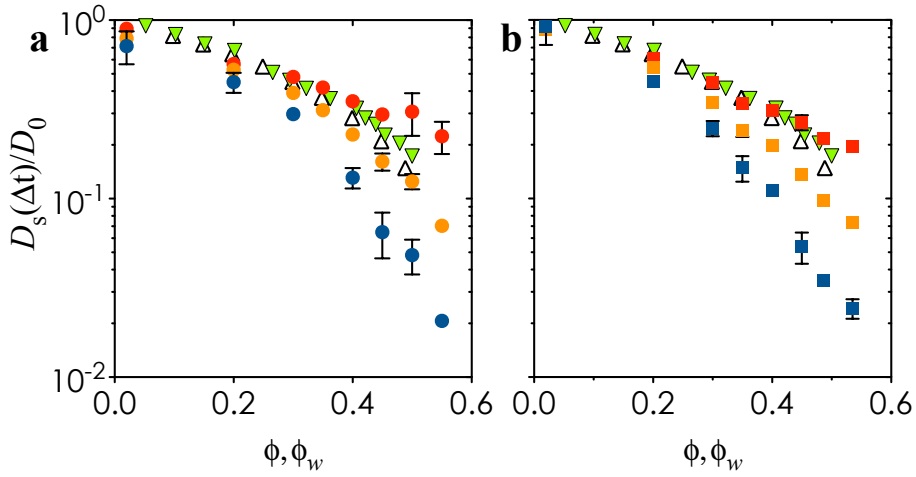

Figure 6.10. Time-dependent translational diffusivity normalized by Stokes-Einstein diffusivity as a function of weight fraction. The data points at Δt = 0.148 s (red), 1.03 s (orange), and 8.03 s (blue) are plotted in for (a) smooth (circles) and (b) rough colloids (squares). Error bars are standard deviations of the largest error observed. Theoretical predictions from [12] for hard sphere suspensions ($\phi \leq 0.50$) are shown as open triangles, and short-time diffusivity values from dynamic light scattering [9] are shown as green inverted triangles.

References

[1] Y. L. Chen and K. S. Schweizer, *Journal of Chemical Physics* **120**, 7212 (2004).
[2] H. Guo, S. Ramakrishnan, J. L. Harden, and R. L. Leheny, *Journal of Chemical Physics* **135**, 154903 (2011).
[3] J. Yang and K. Schweizer, *Journal Of Chemical Physics* **134**, 1 (2013).
[4] J. P. Pantina and E. M. Furst, *Physical Review Letters* **94**, 138301 (2005).
[5] R. Seto, R. Mari, J. F. Morris, and M. M. Denn, *Phys Rev Let*t **111**, 218301 (2013).
[6] D. Lootens, H. van Damme, Y. Hemar, and P. Hebraud, *Phys Rev Lett* **95**, 268302 (2005).
[7] W. K. Kegel and A. van Blaaderen, *Science* **287**, 290 (2000).
[8] E. R. Weeks, J. C. Crocker, A. C. Levitt, A. Schofield, and D. A. Weitz, *Science* **287**, 627 (2000).
[9] R. J. Phillips, J. F. Brady, and G. Bossis, *Physics of Fluids* (1988).
[10] J. F. Brady, *Journal of Chemical Physics* **99,** 1 (1993).
[11] J. F. Brady, *Journal of Fluid Mechanics* **212**, 109 (1994).
[12] P. N. Segrè, O. P. Behrend, and P. N. Pusey, *Physical Review E* **52**, 5070 (1995).
[13] G. H. Koenderink and A. P. Philipse, *Langmuir* **16**, 5631 (2000).
[14] L. Antl, J. W. Goodwin, R. D. Hill, R. H. Ottewill, S. M. Owens, S. Papworth, and J. A. Waters, *Colloids and Surfaces* **17**, 67 (1986).
[15] A. I. Campbell and P. Bartlett, *Journal of Colloid and Interface Science* **256**, 325 (2002).
[16] R. Rice, R. Roth, and C. P. Royall, *Soft Matter* **8**, 1163 (2012).
[17] M. C. Jenkins and S. U. Egelhaaf, *Advances in Colloid and Interface Science* **136**, 65 (2008).
[18] C. J. Dibble, M. Kogan, and M. J. Solomon, *Physical Review E*, **74**, 041403 (2006).
[19] K. F. Seefeldt and M. J. Solomon, *Physical Review E* **67**, 050402 (2003).
[20] R. A. Lionberger and W. B. Russel, *Journal of Rheology* **38**, 1885 (1994).
[21] T. Shikata and D. S. Pearson, *Journal of Rheology* **38**, 601 (1994).
[22] D. Lootens, H. Van Damme, and P. Hebraud, *Physical Review Letters* **90**, 178301 (2003).
[23] N. J. Wagner and J. F. Brady, *Physics Today* **62**, 27 (2009).
[24] M. van Hecke, *J Phys Condens Matter* **22**, 033101 (2010).
[25] S. Papanikolaou, C. S. O'Hern, and M. D. Shattuck, *Physical Review Letters* **110**, 198002 (2013).
[26] E. Somfai, M. van Hecke, W. G. Ellenbroek, K. Shundyak, and W. van Saarloos, *Physical Review E* **75**, 020301 (2007).
[27] K. V. Edmond, M. T. Elsesser, G. L. Hunter, D. J. Pine, and E. R. Weeks, *Proceedings of the National Academy of Sciences USA* **109**, 17891 (2012).
[28] S. M. Anthony, M. Kim, and S. Granick, *Langmuir* **24**, 6557 (2008).
[29] D. Mukhija and M. J. Solomon, *Journal of Colloid and Interface Science* **314**, 98 (2007).
[30] R. A. Lionberger and W. B. Russel, *Journal of Rheology* **38**, 1885 (1994).
[31] E. Brown and H. M. Jaeger. *arXiv*:1307.0269 (2013).

CHAPTER 7

Summary and future work

Concluding remarks

The objective of this thesis was to provide evidence that a guiding framework can be used to engineer the mechanical properties of colloidal gels and glasses based on structural principles. We focused on performing experiments with model systems such that a better connection between microstructure and the bulk rheological behavior can be made. In Chapter 2 we showed that structural rigidity is correlated with remnant elastic stress in gels that have undergone rupture when a large deformation is applied. The stress-bearing capability in yielded gels is a result of a subpopulation of locally rigid clusters, where rigidity is defined, as per Maxwell's isostaticity criterion, as having six or more nearest neighbors. This structural criterion is reduced for frictional and shape-anisotropic particles; that is, non-spherical particles with surface and shape anisotropy could support greater loads even at the same particle loading. This hypothesis motivated the work in Chapter 5 (self-assembly of spheroidal colloids) and Chapter 6 (testing the effect of roughness on rheological properties of dense suspensions close to jamming).

In Chapter 3, we studied the dynamics of yielded gels using a similar experimental method, and found that shear introduced bimodal dynamics in the form of co-existing fast and slow colloids. Increasing the applied strain resulted in a larger subpopulation of fast colloids and a decreasing subpopulation of slow colloids. These slow colloids displayed increased mobility.

When we applied a simple modification using just the slow, structurally rigid subpopulation of particles, we founnd that the theoretical prediction of the elastic modulus (based on mode coupling theory) agreed far better with experimental data.

Chapter 4 describes the development of a model gel system of spherical colloids in which microscopic force, structural characterization, and viscoelasticity were obtained concurrently. Because optical trapping requires a significant refractive index mismatch between the colloids and the suspending solvent, the resolution from confocal microscopy is limited. In addition, a density mismatch is introduced along with the required refractive index mismatch, and gravitational forces compete against gelation on experimental time scales. We varied the solvent composition systematically until a compromise among the constraints on all three techniques were found.

Chapters 5 and 6 describe the synthesis and application of shape-anisotropic particles. Oblate spheroidal PMMA particles were synthesized by a new, simple method and were used in self-assembly experiments in which a long-ranged depletion attraction was generated. These spheroids were refractive index and density-matched with their solvent, such that we were able to visualize the evolution of 3D structure in an experimental timeframe where sedimentation was minimal. A corresponding 3D image processing algorithm was developed where we obtain the orientation and centroids of each particle in the assembled structures. We observed orientational order within an intermediate volume fraction range and at high attraction strengths, but the microscopic origin of this was unclear.

The work in Chapter 6 was primarily motivated by our observation of shear thickening and enhanced elasticity in suspensions of rough particles. Rough PMMA colloids with monodisperse sizes were synthesized by the addition of a cross-linker early on during the free

radical polymerization reaction. Rheological experiments showed that shear thickening behavior set in at lower critical shear rates and lower packing fractions for particles with RMS roughness that are ~5% of their diameter. Surprisingly, there was no difference in the translational motion of smooth and rough colloids, even at the highest particle loading we tested. These results suggest that the hindered rotational motion played a significant role in their rheological properties.

Future work

There is a significant gap between our understanding of shape anisotropy and the bulk properties of soft materials. In this thesis, we showed that the ability to design the anisometry of colloidal materials combined with direct visualization are powerful means to bridge this gap. Here, we propose two specific sets of potential future work that are natural extensions of the results presented in this dissertation.

Effect of hindered rotational motion on rheological properties

The translational motion of rough colloids is quantitatively no different from that of smooth colloids in dense suspensions, as we showed in Chapter 6. Yet, introducing large asperities onto the surface of particles resulted in a drastic reduction in the critical shear rate required for shear thickening, as well as a modest increase in the linear elasticity at high weight fractions. Intuitively, the deep features on these rough colloids should hinder their rotational motion when they are packed closely or in adhesive contact [1, 2]. The development of Janus tracers in Appendix B motivates a study of the rotational motion of these colloids in concentrated suspensions. The ability to track their rotational motion through 3D space and in real time would

provide a quantitative answer as to why and how roughness enhances rheological properties at high packing fractions. The effect of particle size and interaction range would need to be carefully monitored to correctly quantify the effect of roughness on rheological phenomenon.

Rheology of spheroidal assemblies

In addition to surface anisotropy, changes in shape are also known to enhance mechanical strength in granular materials [3]. While Chapter 5 is solely concerned with assembling spheroidal colloids, additional experiments can be performed to determine the effect of stacked structures on the linear elasticity of spheroidal gels. Do orientational structures enhance stress-bearing capability? It has been shown that helical structures are mechanically robust [4]. The linear viscoelasticity of the oriented structures shown in Chapter 5 could be measured via rheometry, and the local mechanical strength of such structures could be probed with optical or magnetic tweezers. These rheological experiments are feasible provided that monodisperse spheroids can be generated reliably in larger quantities. The ability to compare these measurements to equivalent systems consisting of isotropic spheres would provide a convincing argument that shape anisotropy can be used to modify bulk rheological properties.

References

[1] M. Mailman, C. Schreck, C. O'Hern, and B. Chakraborty, *Physical Review Letters* **102**, 255501 (2009).

[2] S. Papanikolaou, C. S. O'Hern, and M. D. Shattuck, *Physical Review Letters* **110**, 198002 (2013).

[3] A. G. Athanassiadis *et al.*, *Soft Matter* **10**, 48 (2014).

[4] C. S. Haines *et al.*, *Science* **343**, 868 (2014).

APPENDIX A

Connecting linear elasticity to the 3D structure and 2D translational dynamics of colloidal gels

The 3D structure and 2D mean-squared displacement of colloidal gels are studied concurrently with linear rheological characterization. Briefly, PHSA-stabilized PMMA colloids ($2a$ = 1.1 μm ± 4%) are suspended at various volume fractions (ϕ = 0.15, 0.20, 0.25, 0.30, 0.35, and 0.40) in a mixture of cyclohexyl bromide (CHB) and decalin (63:37 v/v). Non-adsorbing polystyrene (MW = 900,000 g/mol R_g = 41 nm, R_g/a = 0.07) is added at a dilute concentration (c/c* = 0.4 and 0.5, corresponding to $U \sim$ -3 and -4 k_BT respectively) to induce a short-ranged depletion attraction that leads to gelation. Charge screening is provided by adding 1 μM tetrabutylammonium chloride (Debye length = 69 nm, zeta potential ≤ 10 mV) to the gels.

Gels are allowed to quiescently equilibrate for 30 minutes prior to imaging and rheological characterization. Figure A.1 shows the 2D representative confocal images of these gels after a waiting time of 30 minutes. The 3D image volumes are captured at dimensions of 31 μm × 31 μm × 25 μm (voxel size = 60 nm × 60 nm × 60 nm), and 2D images are captured at 31 μm × 31 μm (pixel size = 60 nm × 60 nm) with a lag time, Δt = 0.074 s. Images are obtained from three independent locations within the same sample, at a distance of ≥ 15 μm above the coverslip. Particle centroids are identified using a local regional maximum of intensity in 3D space, and with edge-detection Hough transform in 2D space. Figure A.2 shows that the volume

fraction identified from the image processing algorithm, ϕ_{IP}, is within 10% of the expected volume fraction from the ratio of the weight of the particles to the weight of the solvent, ϕ_{expt}.

We compute the radial distribution function, $g(r)$, and the contact number distribution, $p(z)$, using the location of the particles in 3D. The $g(r)$ for gels with c/c* = 0.4 (Figure A.3(a)) and c/c* = 0.5 (Figure A.3(b)) are shown. Particles are considered to be in adhesive contact if their separation distance is less that that of the first minimum in the $g(r)$ shown in Figure A.3. Figure A.4 shows that the mean contact number, $\langle z \rangle$, remains close to 6 despite the changes in c/c* and ϕ.

A closer examination of the self-part of the van Hove correlations of the gel samples, $G_s(\Delta x, \Delta t = 1.75 \text{ s})$, shown in Figure A.5, suggests that a small degree of dynamical heterogeneity exist within the samples particularly at low ϕ. Figure A.5(a) shows that particles remain similarly mobile for all ϕ at c/c* = 0.4, with the exception of $\phi = 0.15$ (red) and $\phi = 0.20$ (orange) where a small subpopulation of particles appear to exhibit a propensity for higher mobilities. Nevertheless, the 1D mean-squared displacement (MSD) of the gels at c/c* = 0.4 (Figure A.6) shows that the ensemble-averaged MSD for all ϕ are similar to each other, to within experimental error. The fluctuations in the MSD seen at long times ($\Delta t \geq 10.0$ s) are due to a loss of statistics from small numbers of long-lived trajectories.

The quantitatively similar nature of the dynamics and structure for gels with $0.15 \leq \phi \leq 0.40$ is surprising in the light of rheological measurements (Figures A.7). The strain-dependent elastic and viscous moduli, $G'(\gamma)$ and $G''(\gamma)$, increase with increasing ϕ at c/c* = 0.5. (A comprehensive study at c/c* = 0.4 is currently lacking.) The linear elastic modulus, G', is shown to scale as ϕ^4 in Figure A.8. This increase in linear elasticity cannot be adequately explained by the lack of change in the value of $\langle z \rangle$ and MSD of the samples. Additional theoretical work will

be necessary to connect the change in the linear elasticity of these gels to their local structure and dynamics.

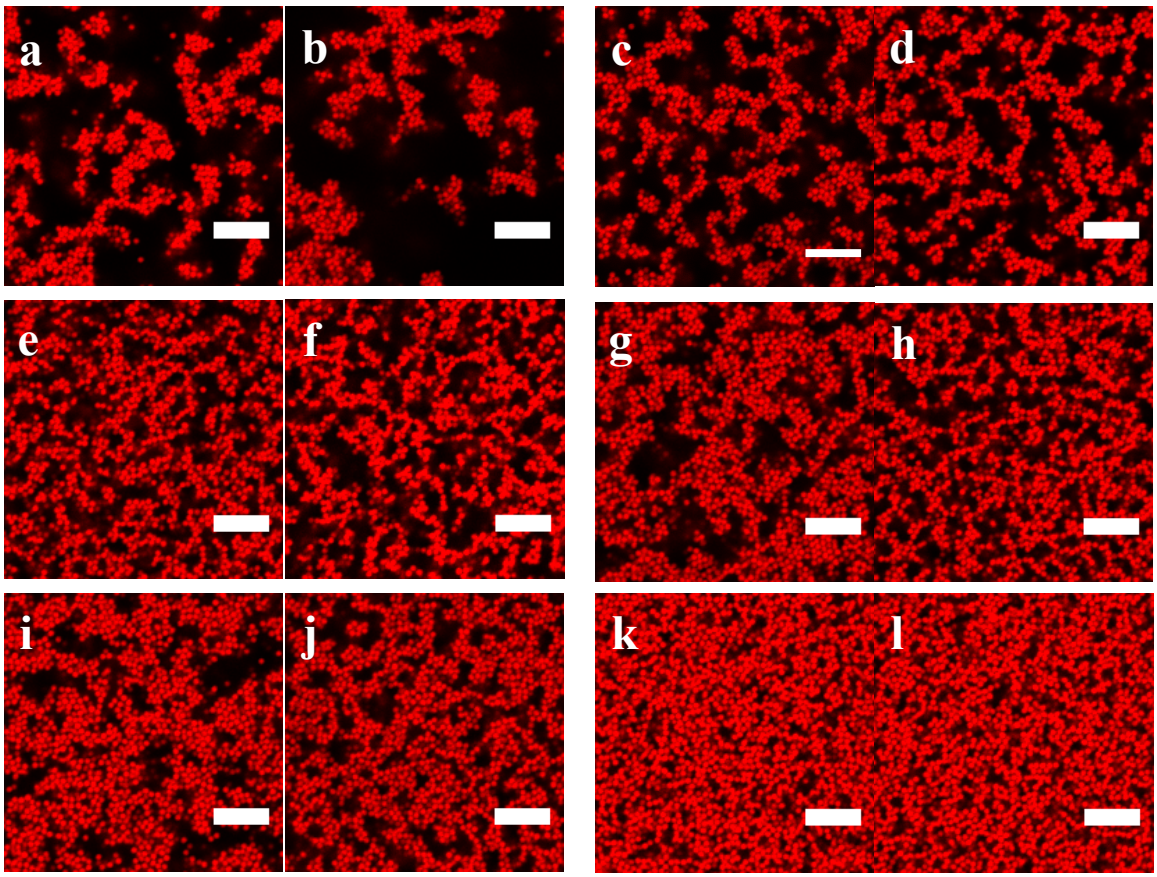

Figure A.1. Representative 2D confocal images of colloidal gels. Colloidal gels with (a) ϕ = 0.15, c/c* = 0.4, (b) ϕ = 0.15, c/c* = 0.5, (c) ϕ = 0.20, c/c* = 0.4, (d) ϕ = 0.20, c/c* = 0.5, (e) ϕ = 0.25, c/c* = 0.4, (f) ϕ = 0.25, c/c* = 0.5, (g) ϕ = 0.30, c/c* = 0.4, (h) ϕ = 0.30, c/c* = 0.5, (i) ϕ = 0.35, c/c* = 0.4, (j) ϕ = 0.35, c/c* = 0.5, (k) ϕ = 0.40, c/c* = 0.4, and (l) ϕ = 0.40, c/c* = 0.5. Scale bars represent 10μm.

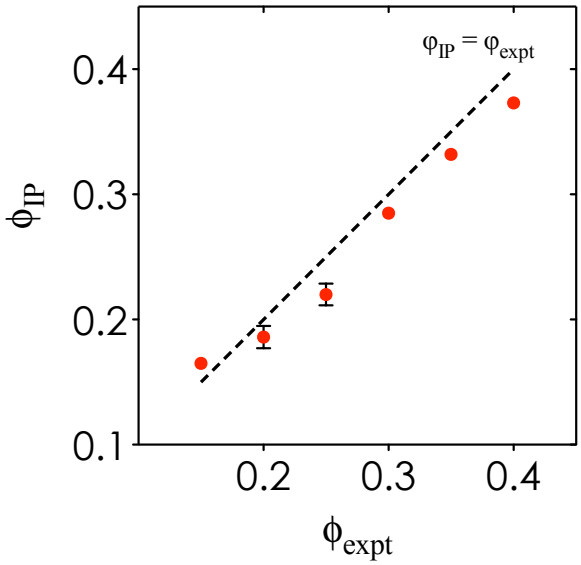

Figure A.2. Fidelity of 3D image processing algorithm. The volume fraction obtained from 3D image processing, ϕ_{IP}, is plotted against the experimentally measured volume fraction, ϕ_{expt}. Dashed line represents the perfect match of both volume fractions, where $\phi_{IP} = \phi_{expt}$.

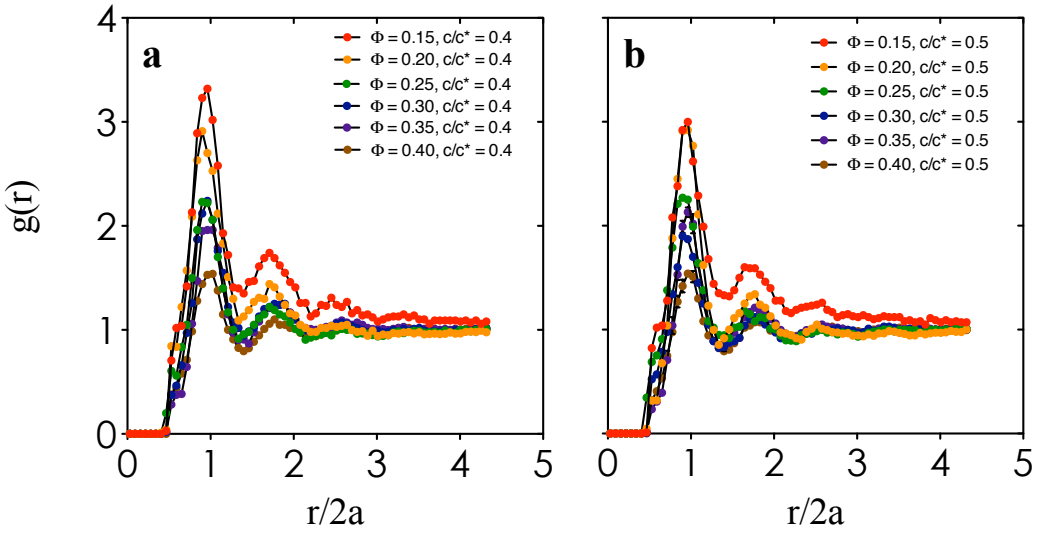

Figure A.3. Radial distribution function from 3D structural quantification of gels. The $g(r)$ are plotted as a function of $r/2a$ for all experimental samples in (a) c/c* = 0.4 and (b) c/c* = 0.5: ϕ = 0.15 (red), ϕ = 0.20 (orange), ϕ = 0.25 (green), ϕ = 0.30 (blue), ϕ = 0.35 (purple), and ϕ = 0.40 (brown). Solid lines are drawn through the $g(r)$ curves to guide the eye.

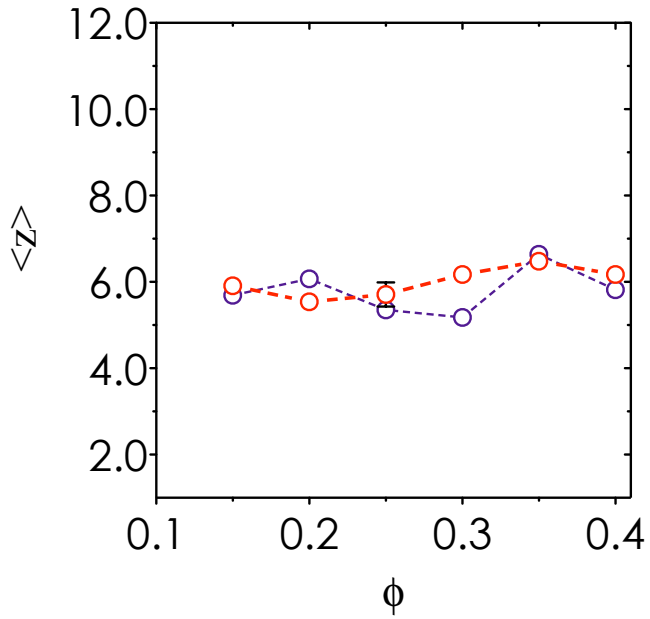

Figure A.4. The mean contact number, <z>, as a function of volume fraction, ϕ. The values of <z> are plotted for gels at c/c* = 0.4 (red) and c/c* = 0.5 (purple). Dashed lines are drawn to guide the eye. Error bars shown are standard deviations obtained from 3 independent locations within a sample.

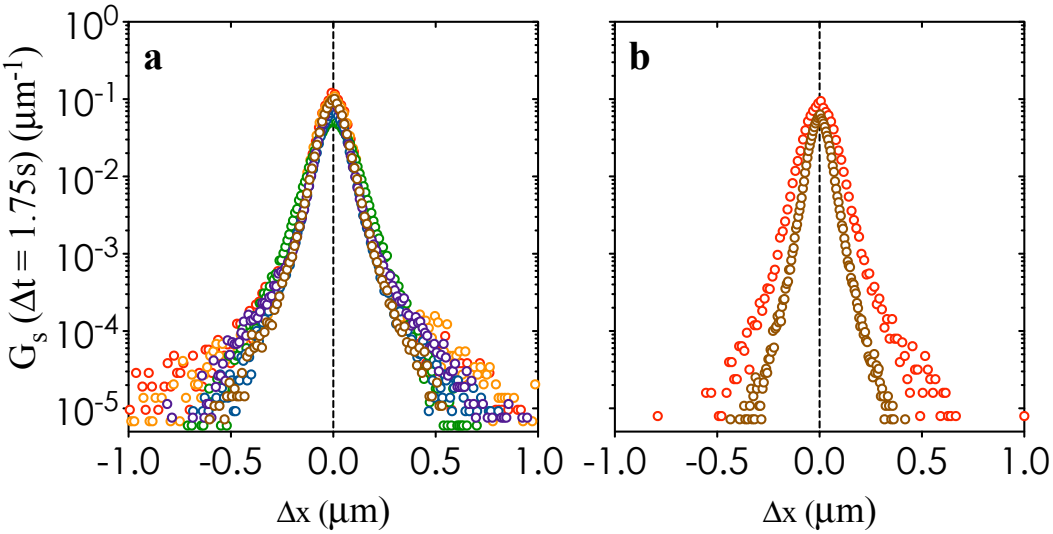

Figure A.5. Self-part of the van Hove correlations. The single-particle displacement probability is plotted for gels with (a) c/c* = 0.4 and (b) c/c* = 0.5. In both plots, $\phi = 0.15$ (red), $\phi = 0.20$ (orange), $\phi = 0.25$ (green), $\phi = 0.30$ (blue), $\phi = 0.35$ (purple), and $\phi = 0.40$ (brown).

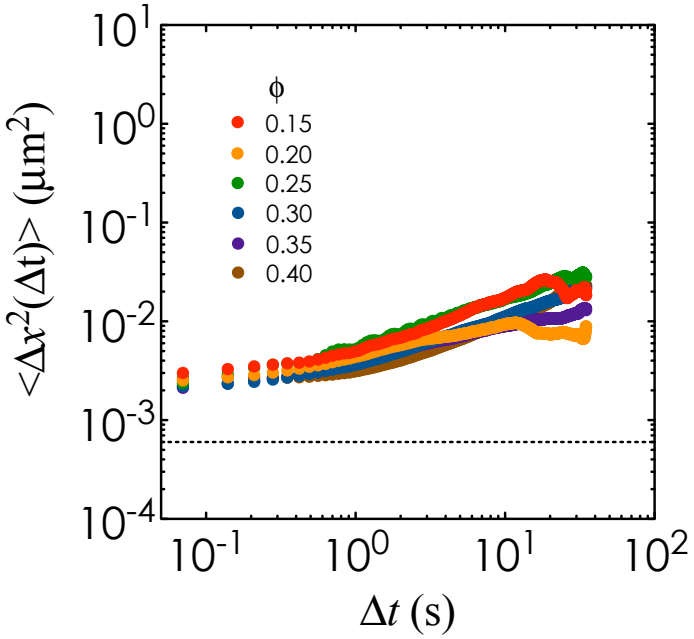

Figure A.6. 1D mean-squared displacement of gels at c/c* = 0.4. The MSD of gels are plotted for ϕ = 0.15 (red), ϕ = 0.20 (orange), ϕ = 0.25 (green), ϕ = 0.30 (blue), ϕ = 0.35 (purple), and ϕ = 0.40 (brown). All samples shown here are from c/c* = 0.4. Dashed line represents the static noise floor from environmental and instrumental error.

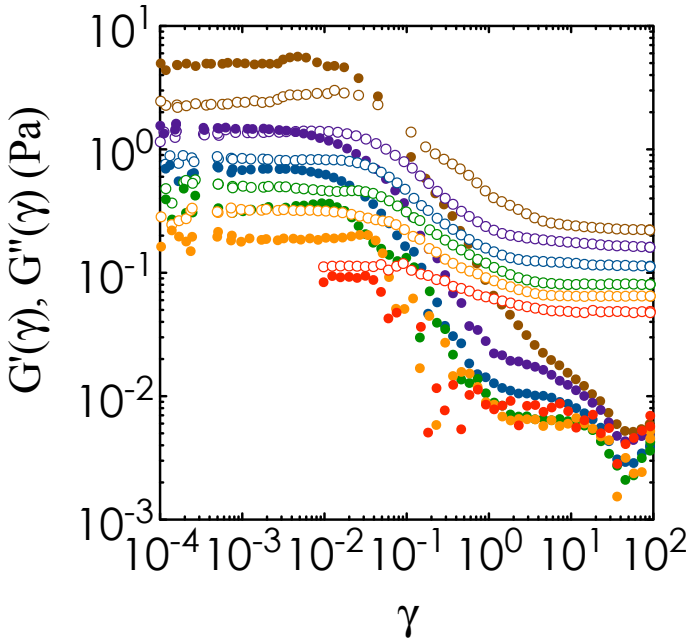

Figure A.7. Strain-dependent elastic and viscous moduli of gels at c/c* = 0.5. The raw data from oscillatory measurements of the strain-dependent elastic and viscous moduli are shown here for $\phi = 0.15$ (red), $\phi = 0.20$ (orange), $\phi = 0.25$ (green), $\phi = 0.30$ (blue), $\phi = 0.35$ (purple), and $\phi = 0.40$ (brown). Solid symbols represent G'(γ) and open symbols represent G"(γ).

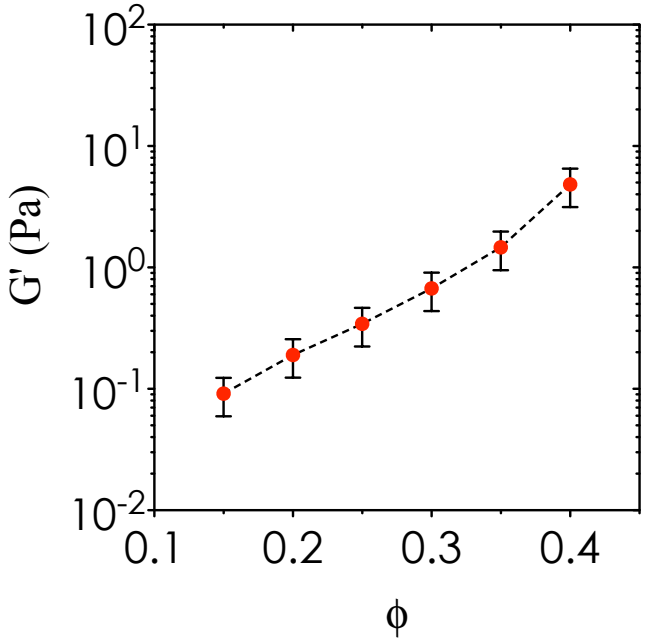

Figure A.8. Volume fraction dependence of the linear elastic modulus for gels at c/c* = 0.5. The value of G' is plotted as a function of ϕ for gels at c/c* = 0.5. Error bars represent 35% confidence intervals. A dashed line is drawn through the data points to guide the eye.

APPENDIX B

Synthesis of Janus PMMA colloids with aluminum layer[§§]

Janus PMMA colloids can be used as tracers in the tracking of rotational motion in dense suspensions. First, the PMMA colloids are suspended at 2-3 wt% in a 12.5%:87.5% (v/v) hexane and isopropanol mixture containing 2 mg/ml stearic acid and 1.25 mg/ml S-(thiobenzoyl)thioglycolic acid. These additives are critical in the adhesion of the aluminum layer onto the PMMA colloids, because of earlier observations that the aluminum layers were prone to separate from the PMMA even after brief sonication. The suspension is spin coated onto glass slides (2" × 3") at 300 rpm for 20 seconds to ensure monolayer thickness, followed by a high spin speed at 3000 rpm for another 20 seconds. The slides are loaded into a thermal evaporator (Åmod, Ångstrom Engineering) and a thin layer of aluminum (5 - 10 nm, Figure B.1(a) and (b)) is deposited at a rate of 0.8 - 1 Å/s onto the substrates. The coated PMMA colloids are scraped off the glass slides using a plastic scraper and cleaned with multiple washings of hexane. They are also filtered using a 11.0 μm Nylon syringe filter to remove residual debris. The Janus colloids can be stored in hexane for months without significant degradation. A centrifugation and solvent transfer step is used to transfer them into mixtures of cyclohexyl bromide (CHB) and decalin. These Janus colloids can be used as tracers due to the optical contrast of the metallic layer. Particle tracking algorithms that identify the centroids of both the PMMA and the

[§§] The development of this technique is partly done with Megan Szakasits.

aluminum layer can be used to track the orientational director, $\vec{u}$, over real space and time (Figure B.1(c)).

The Janus tracers (Figures B.1(d) and (e)) are incorporated into the concentrated colloidal suspensions described in Chapter 6 at a dilute concentration (~ 0.5 - 2 wt%). Suspensions containing these Janus tracers are shown for smooth and rough colloids in Figures B.1(f) and (g). The weight fractions of both suspensions are 0.50. Additional work will be necessary to accurately quantify the rotational diffusivity in these concentrated suspensions.

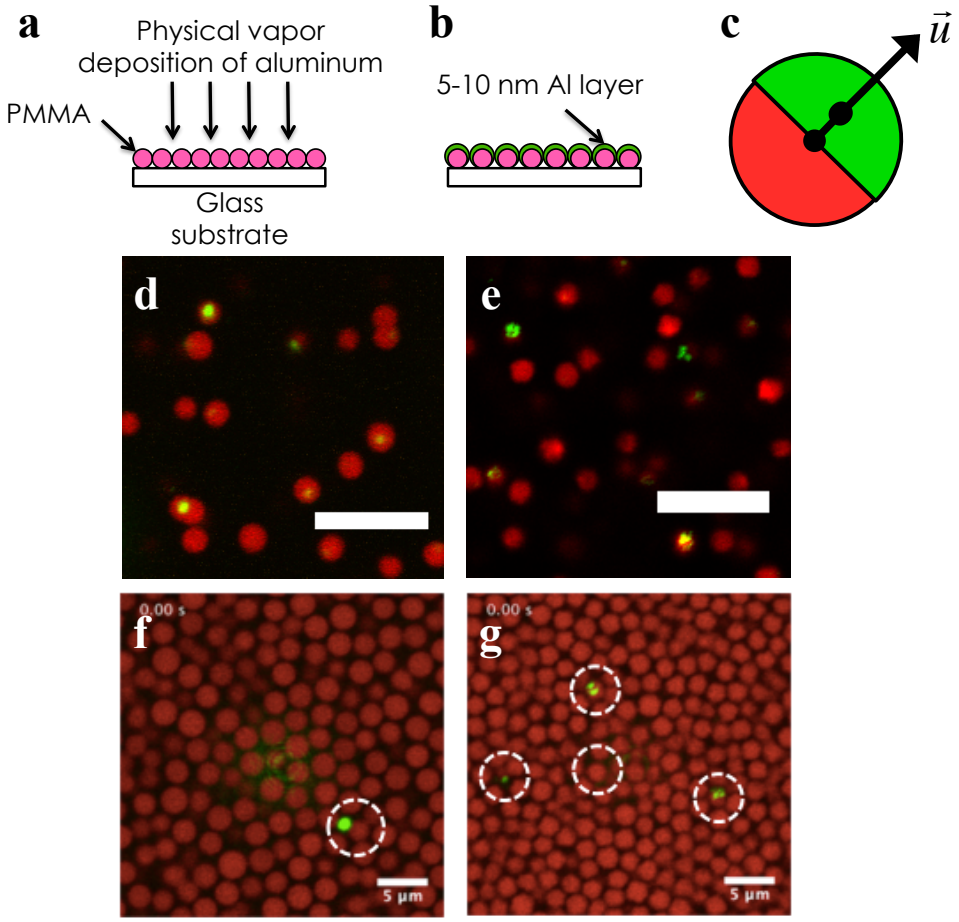

Figure B.1. Overview of Janus tracers that could be used to track rotational motion in dense suspensions. (a) and (b) are schematic of the physical vapor deposition of a thin layer of aluminum (5 - 10 nm) onto PMMA colloids. (c) is the representation of the orientational director of the Janus surface. (d, e) Representative 2D confocal microscopy images of a dilute suspension consisting of (d) smooth Janus and (e) rough Janus colloids. Scale bars indicate 10 µm. (f, g) Representative 2D confocal microscopy images of dense suspensions (ϕ_w = 0.50) of (f) smooth colloids with Janus tracers and (g) rough colloids with Janus tracers. White dashed circles indicate the position of the Janus tracers. In (b-g), green represents the aluminum layer and red represents the PMMA core.